Downloaded from orbit.dtu.dk on: May 05, 2023

DTU Library

Fabrication of Nanostructured Polymer Surfaces and Characterization of their Wetting Properties

Enabling mass fabrication of superhydrophobic surfaces

Andersen, Nis Korsgaard

Publication date:
2016

Document Version
Publisher's PDF, also known as Version of record

Link back to DTU Orbit

Citation (APA):
Andersen, N. K. (2016). *Fabrication of Nanostructured Polymer Surfaces and Characterization of their Wetting Properties: Enabling mass fabrication of superhydrophobic surfaces*. DTU Nanotech.

General rights
Copyright and moral rights for the publications made accessible in the public portal are retained by the authors and/or other copyright owners and it is a condition of accessing publications that users recognise and abide by the legal requirements associated with these rights.

- Users may download and print one copy of any publication from the public portal for the purpose of private study or research.
- You may not further distribute the material or use it for any profit-making activity or commercial gain
- You may freely distribute the URL identifying the publication in the public portal

If you believe that this document breaches copyright please contact us providing details, and we will remove access to the work immediately and investigate your claim.

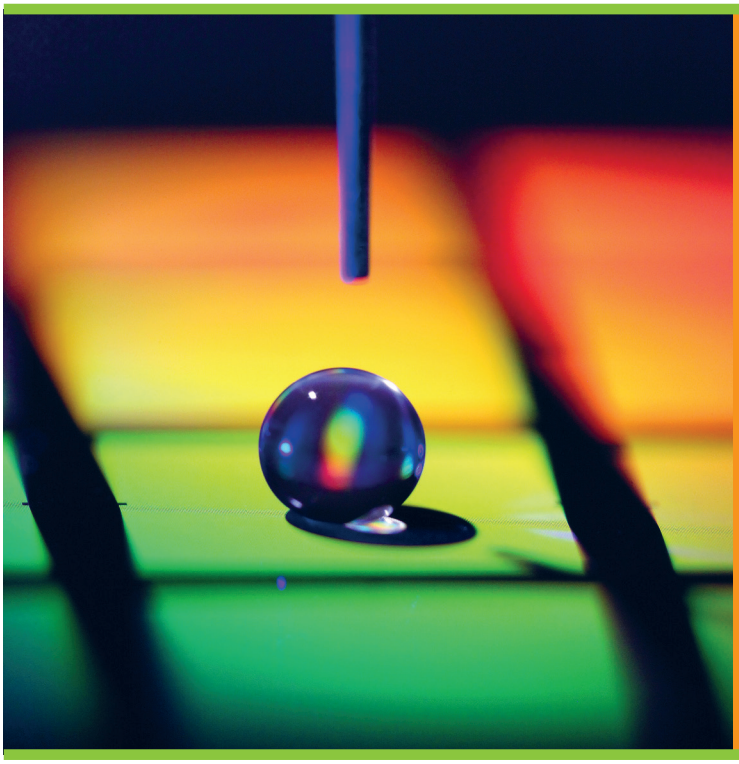

Fabrication of Nanostructured Polymer Surfaces and Characterization of Their Wetting Properties

Enabling mass fabrication of super hydrophobic surfaces

Nis Korsgaard Andersen
PhD Thesis December 2016

DTU Nanotech
Department of Micro- and Nanotechnology

Fabrication of Nanostructured Polymer Surfaces and Characterization of Their Wetting Properties

Enabling mass fabrication of superhydrophobic surfaces

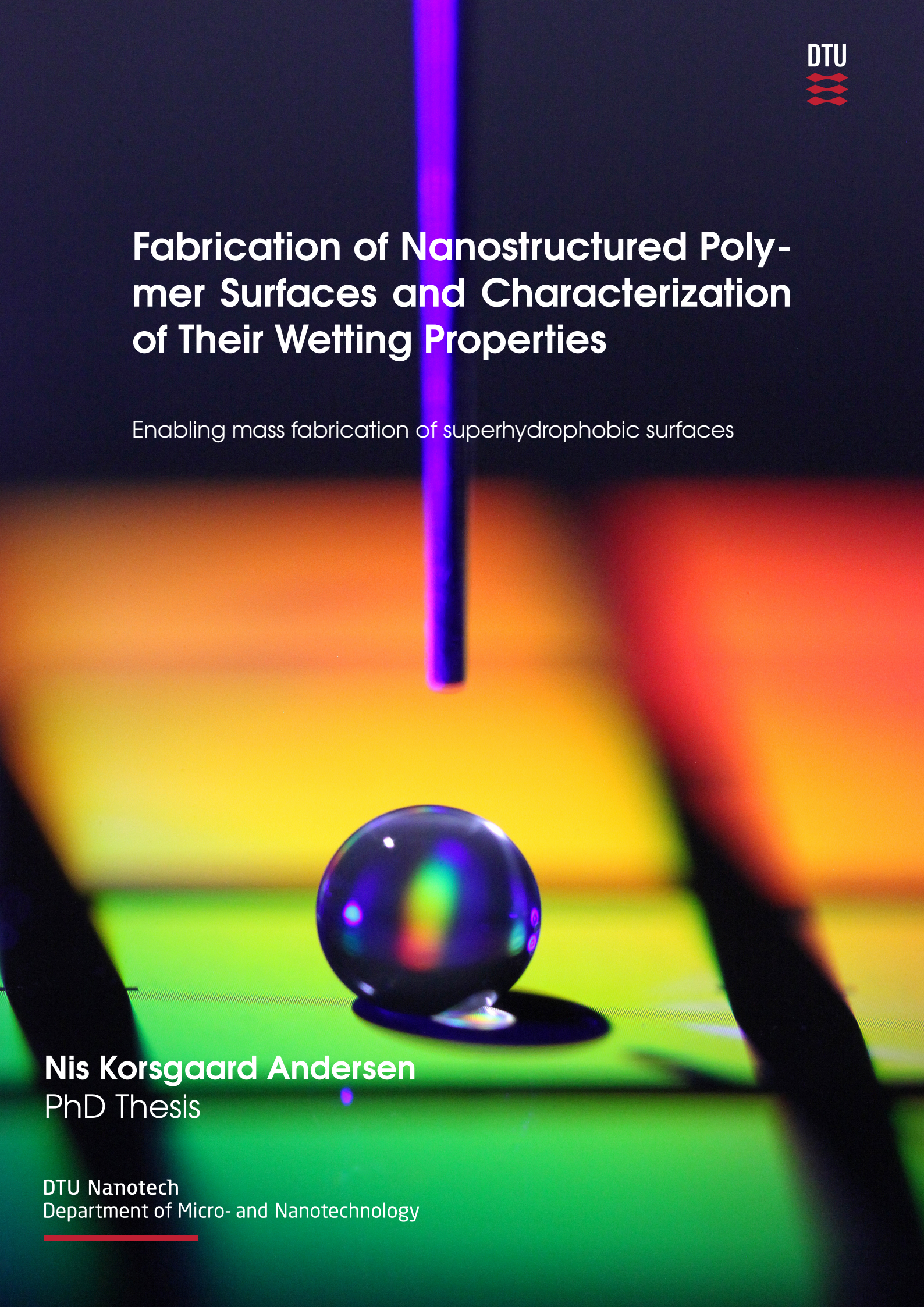

Nis Korsgaard Andersen

PhD Thesis

DTU Nanotech
Department of Micro- and Nanotechnology

Fabrication of Nanostructured Polymer Surfaces and Characterization of Their Wetting Properties

Nis Korsgaard Andersen
Department of Micro and Nanotechnology
Technical University of Denmark
December 5, 2016

Supervisors
Rafael Taboryski, Associate Professor
Fridolin Okkels, Consultant Fluidan

DTU Nanotech
Department of Micro- and Nanotechnology

Fabrication of Nanostructured Polymer Surfaces and Characterization of Their Wetting Properties
Enabling mass fabrication of superhydrophobic surfaces
Nis Korsgaard Andersen

© Nis Korsgaard Andersen, 2016.

Supervisor: Rafael Taboryski, Department of Micro and Nanotechnology
Co-supervisor: Fridolin Okkels, Fluidan
Examiner: Name, Department

PhD thesis August 2016
Department of Micro and Nanotechnology
Polymic Group
Rafael Taboryski
Technical University of Denmark
Kgs. Lyngby

Cover: Water on hierarchical micro- and nanostructure in Silicon coated with FDTS (True colours). The structures are presented in chapter 5. Photo by Jesper Scheel.

Typeset in LaTeX
Document compiled: December 5, 2016
Kgs. Lyngby, Denmark 2016

Abstract

In the past decade, there have been numerous examples of surfaces created with novel functionalities. These functional surfaces are predicted to have a massive impact on a range of commercial sectors within the next five years. Most realized functional surfaces rely on tailored micro- and nanoscale roughness, which cannot be produced with current mass fabrication technologies. The technology platform needed to create these surfaces has to be directly compatible with current mass production platforms, to commercially realize micro- and nanotextured surfaces. This comparability can be achieved by direct micro- and nanostructuring of commerical injection molding tools to create the desired surface structures directly in the molding process.

The aim of this project was to enable the fabrication of surfaces with controlled wetting by injection molding.

During the project, I have demonstrated improvements in many of the fields related to mass-fabrication of water repellent surfaces. Including:

- Basic research in wetting phenomena; studying the role of multiple heights, irregular structures, and the transition to hierarchical structures.
- Development of algorithms for improved contact angle fitting.
- Simulations of wetting transitions.
- Clean room fabrication of functional surfaces, and production of micro- and nanostructured mold inserts.
- Injection molding of micro- and nanostructured polymer parts on a commercial injection molding machine.
- Co-invented a patented technique for microstructuring steel molds able to produce superhydrophobic polymer parts.

The patented microstructuring technique generates microstructures similar to those found on the leaf of the lotus flower, without the overlaying nanostructure. Despite the lack of hierarchical structures, the microstructured surface shows excellent water repellent properties. The demonstration of a single level, superhydrophobic, structure with low aspect ratio, served as inspiration for studies in the underlying wetting mechanisms. This resulted in two published studies. The first study concerns the differences between lattice based clean room structures and the irregular structures produced by the patented microstructuring technique. The second study bridges the gap between silicon structures produced by planar processes in the clean room and the smooth multi-height structures often found in nature.

Finally i have demonstrated a novel type of hierarchical structures to get a better understanding of the role of hierarchy in wetting phenomena. I have produced and characterized hierarchical structures with the same surface coverage achieved in several different configurations. This leads to an interesting finding, not covered by modern wetting theories, where the local configuration of nanostructures governs the wetting behavior of the hierarchical structure.

Dansk Resumé

Der har i det seneste årti været præsenteret mange eksempler på overflader med nye funktionaliteter. Markedsanalyser spår at disse nye egenskaber vil have stor betydning indenfor en række kommercielle markeder inden for de næste 5 år. De fleste overflader med specielle egenskaber er afhængige af en specifik mikro- og nanostruktur på overfladen. Disse overfladestrukturer kan ikke produceres direkte med de nuværende produktionsmetoder. For at realiserer kommercielle produkter med funktionelle overflader kræver det at disse strukturer kan produceres på en måde der er kompatibel med de nuværende produktionsmetoder. Denne kompatibilitet kan opnås ved at mirko- og nanostrukturere sprøjtestøbningsværktøjer for derved at opnå den ønskede overfladestruktur direkte i støbeprocessen.

Målet med dette projekt har været at gøre det muligt at sprøjtestøbe plastik emner med vandafvisende overflader.

Under projektet har jeg demonstreret forbedringer inden for en række felter der relaterede til massefabrikation af vandafvisende plastik emner:

- Grundforskning indenfor interaktioner mellem væsker og strukturerede overflader. Her har jeg undersøgt effekten af højdevariationer, irregulariteter og hierarkiske strukturer.
- Udviklet algoritmer der forbedre målingen af kontaktvinkler.
- Simuleret vand indtrængen i porøse overflader under vand.
- Fabrikeret mikro- og nanostrukturerede overflader i renrum. Disse strukturer har jeg også overført til sprøjtestøbe indsatser for at producerer plast emner med de fabrikerede strukturer.
- Har været medopfinder af en patenteret teknik til at mikrostrukturere stål forme der kan producere vandafvisende prøver.

Den patenterede mikrostruktureringsteknik generere mikrostrukturer der minder om strukturerne på overfladen af bladet fra en lotus blomst, uden det ekstra lag af nanostrukturer. På trods af de manglende nanostrukturer er de mikrostrukturerede emner meget vandafvisende. Disse strukturer uden nanostrukturer har været inspiration til flere fundamentale studier i hvordan overfladestrukturer interagerer med vand. Det har resulteret i to publikationer. Det første studie undersøgte effekterne af irregularitet i overfladestrukturerne. Det andet imødekommer den store forskel mellem kantede silicium strukturer af samme højde og de runde former, i forskellige højder, der ses i naturen.

Endelig har jeg fabrikeret en ny type hierarkisk struktur der kan afdække de underlæggende mekanismer i interaktionen mellem overflade strukturer og væsker. Disse strukturer er lavet med samme overfladetæthed og linjetæthed, men i forskellige konfigurationer. Ved at studere disse strukturers interaktion med væsker har det været muligt at få ny viden omkring de drivende mekanismer bag vandafvisende overflader med hierarkiske overfladestrukturer.

List of Abbreviations

ASE advanced silicon etching.
BARC bottom anti reflection coating.
CAGR compound annual growth rate.
COC cyclic olefin copolymer.
DRIE deep reactive ion etching.
ESEM environmental scanning electron microscope.
ESONN European School on Nanosciences and Nanotechnologies.
FDTS Perfluorodecyltrichlorosilane.
FHNW Fachhochschule Nordwestschweiz.
LIGA lithographie, galvanoformung und abformung.
LLDPE linear low-density polyethylene.
LPCVD low pressure chemical vapor deposition.
MEMS microelectromechanical systems.
MVD molecular vapor deposition.
PA polyamide.
PP polypropylene.
PSI Paul Scherrer Institute.
SEM scanning electron microscope.
TEOS Tetraethyl orthosilicate.

Preface

The work presented in this Ph.D. thesis have been supervised by Rafael Taboryski, and carried out in the POLYMIC group. The main focus of the POLYMIC group is to transfer existing capabilities in academia to commercially relevant production platforms. Previously the focus in the group was injection molding of Lab-on-a-Chip devices but have recently changed to micro- and nanostructured surface in polymer. Microstructuring of surfaces can bring novel functionalities directly from the fabrication process, e.g. colored surface made from transparent polymer.

The focus in this project have been to produce water repellent surface on injection molded surfaces, using a micro- and nanostructured mold. Since this functionality is already well known from nature, and academia, the main focus in the project is the design for manufacturing. The design of surfacestructures quickly became the main focus of the project since most water repellent surfaces published in literature are not possible to realize by injection molding.

Early in my Ph.D. project I discovered, together with Carl Esben Poulsen and others, a structuring technique capable of producing highly water repellent surfaces in injection molded polymer. The structure produced by this novel manufacturing technique showed, in contrast to other known designs, to be very suited for manufacturing by injection molding. Much of the later work in the project was centered around explaining the superior performance of these easy-to-mold structure. The intellectual property of this manufacturing technique have been secured in three patents included at the end of the thesis.

The work presented in this Ph.D. thesis have been conducted between October 15th 2012 and August 22nd 2016. During this time i have been on leave three times.

1 In spring 2013 i was forced on leave for four months to do civil service instead of being conscripted to the Danish army. Resulted in coauthoring a publication that is not included in this thesis.[1]
2 During 2015 i was on 10 weeks paternity leave.
3 In fall 2015 i was working on a spin-out project, TransForm, where we got external funding to mature our patent pending technology. The invention behind this was discovered while working on my Ph.D. and will be included in this thesis.[a]

The length of a PhD Scholarship in Denmark is three years and the end date have thus been extended according to the time on leave. During my PhD i was on a three month external stay at Fachhochschule Nordwestschweiz (FHNW) and Paul Scherrer Institute (PSI), in Switzerland. The work at the external stay resulted in a co-authorship of a paper that is not included in the main text but instead included in an appendix. All work presented in this thesis have been conducted at DTU Nanotech, DTU Danchip, FHNW or PSI.

[a] `www.transform-technologies.dk`

Acknowledgement

First and foremost, thanks to my beloved wife for always supporting and encouraging me when I needed it the most.

Thanks to the POLYMIC group, whose members have changed a lot during my time at DTU, for always having a relaxed atmosphere. With you it is always possible to discuss clean room or cooking recipes. Especially to Emil Søgaard for teaching me a lot of the basic skills used in this project. Also, thanks to the Danchip Staff for helping with clean room equipment, especially Conny Hjort, Jesper Hanberg, and Claus Højgaard Nielsen for always taking their time to help me out.

I would also like to thank my friends from my B.Sc. and M.Sc. for working as Ph.D.'s at DTU, enabling cross department lunch breaks. It is comforting to know that Ph.D. problems are the same anywhere, its not just in your project where nothing seems to work.

Thanks to my supervisor Rafael Taboryski, whose reality checks have been appreciated, and needed. Thanks for interesting discussions and advice on all sorts of topics, ranging from publishing of papers to everyday problems.

A special thanks Carl Esben Poulsen for the long term collaboration in the TransForm project, always being always helpful and cheerful. In this regard I would also thank the rest of the TransForm team, Kasper Kistrup, Anders Wolf, Rafael Taboryski, Flemming Jensen, and Thorsten Freltoft for the experiences and insights in commercialization of new technologies.

I would like to thank Prof. Magnus Christiansen and Dr. Helmut Schift for accepting me into their groups at my external stay. And a special thanks Cristian Rytka for teaching me so much about injection molding, both for academic and commercial use.

Lastly, I would thank the Augustinus Foundation, the Jens Otto Mønsted Foundation, and the Oticon Foundation, for financially supporting my external stay and DTU POC for financing the development of TransForm technologies.

Contents

Appendices

List of publications

Journal papers

Paper 1-4 four are included in the thesis, whereas Paper 5-6 are attached in Appendix D and E.

Paper 1
Søgaard, E., **Andersen, N. K.**, Smistrup, K., Larsen, S., Sun, L. & Taboryski, R. Study of Transitions between Wetting States on Microcavity Arrays by Optical Transmission Microscopy. *Langmuir* 30, 12960–12968 (2014).[2]

- Developed and used a model to describe the experimental results presented in the paper
- Discussions about data treatment, experimental setup and the conducted experiments.
- Written the parts of supplementary materials concerning simulations
- Proofreading of final paper

Paper 2
Andersen, N. K. & Taboryski, R. Multi-height structures in injection molded polymer. *Microelectron. Eng.* 141, 211–214 (2015).

- Designed the structures by modeling in MATLAB.
- Conducted all the fabrication of samples used in presented in the paper.
- Characterized samples by Interference microscopy, scanning electron microscope (SEM) and contact angle measurements.
- Wrote the paper and drew all figures used in the paper.

Paper 3
Andersen, N. K. & Taboryski, R. Drop shape analysis for determination of dynamic contact angles by double sided elliptical fitting method. Submitted to *Measurement Science and Technology* June 26. 2016

- Conceived the idea for the double sided elliptical fitting.
- Implemented drop shape analysis with both polynomials and elliptical fitting in MATLAB.
- Documented the implementation and tested stability of implementation.
- Wrote paper and made all figures for the paper.

Paper 4
Larsen, S. T., **Andersen, N. K.**, Søgaard, E. & Taboryski, R. Structure irregularity impedes drop roll-off at superhydrophobic surfaces. *Langmuir* 30, 5041–5 (2014). (equally contributing author with S.T. Larsen)

- Developed model to explain results (in collaboration with R. Taboryski).
- Did a major overhaul of both text and figures after the first submission which only included experimental results.
- Proofreading of the final paper.

Paper 5
Poulsen, C. E., Kistrup, K., **Andersen, N. K.**, Taboryski, R., Hansen, M. F. & Wolff, A. Laser ablated micropillar energy directors for ultrasonic welding of microfluidic systems. *J. Micromechanics Microengineering* 26, 067001 (2016).

- Developed and characterized the process of microstructuring mold inserts (with C.E. Poulsen & K. Kistrup).
- Discussions about injection molding process.
- Proofreading of final paper.

Paper 6
Rytka, C., Opara, N., **Andersen, N. K.**, Kristiansen, P. M. & Neyer, A. On The Role of Wetting, Structure Width, and Flow Characteristics in Polymer Replication on Micro- and Nanoscale. *Macromol. Mater. Eng.* 301, 597–609 (2016).[3]

- Produced inserts used for injection molding of hierarchical structures.
- Assisted in the injection molding of samples with hierarchical structures.
- Characterization of samples with hierarchical structures, both in SEM and Laser Confocal Microscope.
- Discussions about the measurements of contact angles.
- Proof reading of the final paper.

Patent applications

Patent application 1
Carl Esben Poulsen, Anders Wolf, **Nis Korsgaard Andersen**,Kasper Kistrup, and Rafael Taboryski. Replication Tool and Method of Providing a Replication Tool. Priority calim of regional application 05/12/2014.[4]

- Participated in developing the patented method for microstructuring tools.
- Participated in developing the patented method for using the tools.
- Participation in proof of concept.
- Participated in correspondence with patent office and patent agent.

Patent application 2
Carl Esben Poulsen, Anders Wolf, **Nis Korsgaard Andersen**,Kasper Kistrup, and Rafael Taboryski. Micro-scale energy directors for ultrasonic welding. Priority calim of regional application 05/12/2014.[5]

- Participated in developing the patented method for microstructuring tools.
- Participated in developing the patented method for using the tools.
- Participated in correspondence with patent office and patent agent.

Patent application 3
Carl Esben Poulsen, Anders Wolf, **Nis Korsgaard Andersen**,Kasper Kistrup, and Rafael Taboryski. Method of Producing an Item with Enhanced Wetting Properties by Fast Replication and Replication Tool Used in the Method. Priority calim of regional application 05/12/2014.[6]

- Participated in developing the patented method for microstructuring tools.
- Participated in developing the patented method for using the tools.
- Participation in proof of concept.
- Participated in correspondence with patent office and patent agent.

1

Introduction

In this project, I aim to control wetting of surfaces on injection molded polymer parts by controlling the surface structures on the micro- and nanoscale. The project is a multidisiplinarry project with a primary focus on wetting, micro- and nanofabrication, and injection molding. In this chapter, I will give a short introduction to the three topics and describe the state of the art within wetting controlled by surface structures.

1.1 Wetting

Wetting is something that affects our everyday life, even if we do not notice it. Sponges suck up liquid, raindrops leave a trail of water on the window and paint stick to the wall. Everywhere we see liquid, we see wetting. Sometimes it is important, how a liquid wets a surface, sometimes not. Many plants rely heavily on specific wetting properties to clean their leaves[7], guide water to their roots[8] or take up water from dew.[9] Through millions of years, plants have evolved and tailored their wetting properties for their particular environment. In engineering wetting play a significant role in producs like fabrics, kitchenware, medical devices, painting, etc. The abundance of wetting phenomena in nature have inspired many innovative solutions, e.g. modern outdoor clothes that are breathable but also water proof. This is obtained by using a finely meshed structure with specific chemical properties, the same mechanism that keeps birds from getting wet.[10]

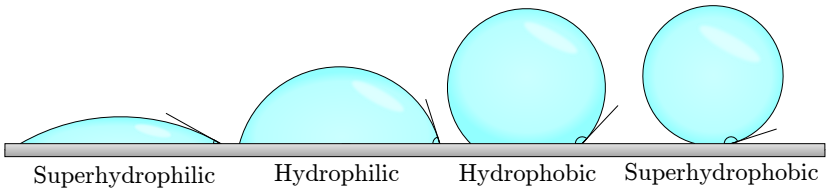

Figure 1.1: Water drops on a surface showing different contact angles, increasing from left to right.

A central term in wetting is the contact angle between a liquid and a solid. By definition the contact angle is measured inside the liquid. The contact angle is always in the range between 0° and 180° where the limits are referred to as completely wetting and non-wetting, respectively. The contact angle governs how liquid spread across the surface depending factors like surface roughness and surface chemistry. For water contact angles below 90° a surface is considered hydrophilic, whereas contact angles above 90° it is considered hydrophobic. In the extreme cases of contact angles close to 0° or 180° the surface can be refferred to as superhydrophilic or superhydrophobic, respectively. A schematic drawing of the different

contact angle regimes are shown in figure 1.1. For superhydrophobic surfaces, there has been some scientific discussion about the exact requirements for the "super" prefix. Some suggest that it applies to all surfaces that show a water contact angle above 150°,[11] while others also impose the requirement of low adhesion.[12] An example of a surface that shows very high contact angle and adhesion is a rose petal. A drop on a rose petal is almost spherical, but will not detach the surface, even when turned upside down. The seemingly contra-intuitive phenomena with "non-wetting" surface that have a high adhesion to liquid will be explained in chapter 2. The argument for requiring low adhesion for the "super" prefix is that the word hydrophobic meaning fear of water, this would refer to repelling water rather than just showing a high contact angle. To avoid misunderstanding, I prefer to use the term water repellent for surfaces where water easily moves off the surface. In the case that drops easily rolls off the surface, the drop will rinse the surface of all contaminants that have an affinity for water. Surfaces that show a high degree of cleaning by rinsing with water are called self-cleaning surfaces. To achieve the self-cleaning property, it is imperative that water drops on the surface have little resistance to rolling off the surface. It is not enough that the drops just leave the surface. When a drop slides down a surface with relatively high adhesion it leaves a trail of liquid, in this trail, the contaminants can stay on the surface instead of leave with the drop, see figure 1.2. An everyday example on this is raindrops on windows, although the drops slide down the glass they leave a trail of water, and after rain, a window is not much cleaner than before the rain.

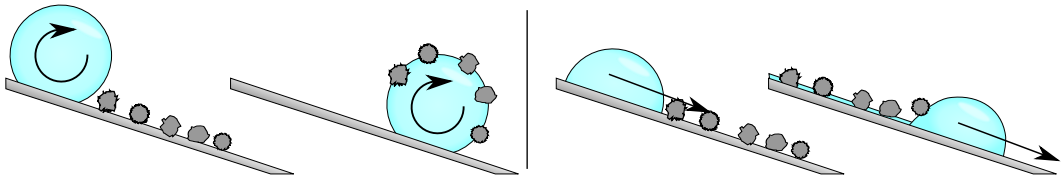

Figure 1.2: Illustration of the self-cleaning effect. A drop that rolls off the surface leaves the surface dry and carry contaminants off the surface (left). A drop that slides off the surface leaves a trail of water with contaminants (right).

In 1997 Barthlott and Neinhuis discovered that well known self-cleaning properties of lotus leafs (*Nelumbo nucifera*) originate from a particular combination of surface structures and surface chemistry. By using SEM, they showed that the surface of lotus leafs have microstructures covered in nanostructures. The self-cleaning property is seen on many plant leafs but is considered to be outstanding on the leaf of the lotus flower. This effect is therefore often called the lotus effect. A combination of micro- and nanoscale texture is referred to as a hierarchical structure. Several studies suggest that hierarchical structures are necessary for creating a water repellent surface.[13–16] In chapter 5 I will discuss whether this is the case. It has later been shown that it not possible to achieve superhydrophobic properties by only engineering the chemical composition of a flat surface. This was shown by obtaining the most hydrophobic material known to exist which have a maximal contact angle of 119°.[17] To create a superhydrophobic water repellent surface it is, therefore, necessary to combine hydrophobic surface chemistry with surface roughness.

By introducing surface structures like on the lotus leaf, it is possible for a drop to rest only on the top of these structures. A schematic drawing of this is shown in figure 1.3. With the right surface structures the area of water that touches the solid surface can be only a few percent of the total footprint. With such a little area of solid-liquid contact the adhesion forces are tiny, which results in very high contact angles and very low resistance to moving on the surface. It is widely accepted that specific surface structures are necessary to achieve

a water repellent surface, and this is consistent with findings in nature.[7–9,11,14,18,19]

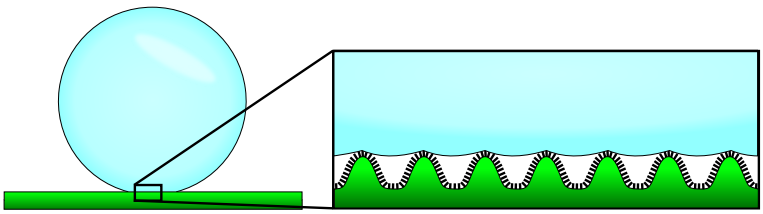

Figure 1.3: Illustration of superhydrophobic state on a lotus leaf. The hierarchical surface structure on the leaf gives rise to very high contact angles and low adhesion.

1.1.1 Importance of controlled wetting

The ability to control wetting is anticipated to have a huge impact on a variety of engineered materials, ranging from windows and cars to medical devices and industrial production. And it is not difficult to imagine why. As an example, self-cleaning surfaces on a skyscrapers windows could eliminate the need for window cleaning that is both expensive and dangerous.

A market analysis by BBC research from 2013 expects a massive growth of nanoengineered surfaces within the next five years, see table 1.1. The eight markets analyzed are each comprised of different sub-markets driven by various nanoengineering technologies. Controlled wetting is expected to play a significant role in all but the biomedical market. Controlled wetting comprises, superhydrophobicity, anti-fogging and self-cleaning by the lotus effect. In the terms of the report, the biomedical market does not include controlled wetting but is instead focused on anti-biofouling technologies to be used for keeping medical ware, hospitals, production facilities, etc. clean from bacterial growth. Controlled wetting is, however, important to many medical and diagnostic devices, such as microfluidics. The BBC report expects average yearly growth of around 30% in 10 years, resulting in a significantly sized market of 2.5 billion USD in 2022. Such a market size requires that many of technologies that have been shown to work in academia are transferred to industrially relevant platforms. In the following, I will highlight some relevant markets from the BBC report.

	Global Market ($ millions)				CAGR%	
Applications	2012	2017	2018	2022	2012-2017	2017-2022
Biomedical	0	2.7	15.8	158.1	-	125.7
Automotive	0	4.2	16.9	74.4	-	77.7
Aerospace	0	0	8.5	150.0	-	105.0*
Electronics	28.0	294.7	326.9	560.3	60.1	13.7
Energy	0	0	21.8	236.5	-	81.5*
Building Materials	150.0	300.0	355.1	1078.0	14.9	32.0*
Optics	0	12.4	33.3	169.7	-	68.8
Textiles	5	8	15.9	40.4	9.9	26.3*
Other	0	0	5.1	28.1	-	53.2*
Total	183.0	662.0	799.3	2495.5	27.7	32.0

*CAGR 2018-2022

Table 1.1: Table from BBC Research report on expected global markets for nanoengineered surfaces, including calculated compound annual growth rate (CAGR).[20]

Building materials. There is already windows and paints on the market being branded as self-cleaning. These products achieve self-cleaning by the addition of titanium dioxide, in a thin layer on windows and as particles in the paint. Titanium dioxide drives a photocatalytic reaction that breakdowns organic molecules when exposed to sunlight. The end products of the reaction are then easily washed off by rain, and the surface is thus able to clean itself. Self-cleaning windows using the lotus effect have so far only been demonstrated in scientific literature.[21] For bringing this technology to commercial products, the production cost needs to be significantly lowered. Probably by coating or laminating the glass instead of direct structuring of the glass. The state of the art water repellent coatings are not optically transparent and thus cannot be used on windows. For the remaining part of this report, the phrase self-cleaning will refer to cleaning by the lotus effect, i.e. removal of dirt by water repellency.

Electronics and Automotive. In consumer products such as hearing aids, cellphones, and other electronic devices there is a growing interest from the industry to prevent the intrusion of water into the device. In 2013 many large cell phone and hearing aid brands introduced a hydrophobic coating that should prevent water from entering the device, thereby protecting the electronic components.[22,23] There is a range of commercially available coatings to achieve this by gas phase deposition of some, usually fluorine based, hydrophobic compound.[24] These coatings usually have a thickness in the range of a few nanometers and works by changing the surface chemistry. The surface chemistry of coated surfaces often resembles Teflon, which has a water contact angle of $\approx 109°$. Such a water contact angle is close to the maximum possible water contact angle from a flat surface. With only a few nanometers in thickness, the coating does not create significant surface roughness and is thus unable to surpass the maximum contact angle of 119°. The products by *NewerWet* exceed this limit by including microparticles in their coating to create surface roughness even when applied to flat surfaces. Such a solution present three immediate problems,

- microparticles interfere with light creating opaque surfaces,
- the particles are loosely bound to the surface, resulting in low coating durability,
- particles are often made from fluorocarbons that are bioaccumulating.[25,26]

Similar coatings have been developed in the car industry facing the same problems. To my knowledge, the lifetime of a superhydrophobic coating of a car is around a year. The car coatings also create a white haze, changing the color of all but white cars, reducing its applicability.

Aerospace, Marine, and Military. In the BBC report, there is mentioned several companies working with anti-icing coatings and sharkskin like coatings. Anti icing coatings are imagined to reduce the problems with icing of mechanical parts in aeroplane wings. Shark skin coatings can be used for drag reduction in either air or water. Anti-icing coatings are usually based on creating a water repellent surface.[27] This seems like an intuitive approach if the surface repels water and dew rolls off the surface there will be no buildup of ice on the surface. The mechanism for icing can, however, be very different from water freezing on a cold surface. Surfaces can ice up from water vapor condensing directly as ice or supercooled drops that freeze immediately after touching the surface.[28] In these cases, the surface coating cannot prevent the ice from forming on the surface, but should instead facilitate a very low adhesion/easy removal.

Other, not included in BBC report. In industrial productions, there is also a growing interest in the ability to control the wetting of surfaces by liquids. When applying paint to a surface, you would want the paint to stay where it was applied, not contract into droplets and

not spread out in undesired shapes. The interaction between a liquid and a flat solid surface is governed by the chemical properties of the materials. The specific wetting properties in e.g. a painting process put heavy constraints on solid-paint combinations that are usable. To circumvent this limitation the industry is using a stack of wetting promotion layers that will ensure proper wetting properties, or chemically alter the surface by for instance flame treatment. If the wetting behavior of an item was modified by microstructuring its surface, the industrial processes could be greatly simplified.

1.1.2 State of the art surfaces with tailored wetting

In this section, I will highlight different techniques concerning controlled wetting of surfaces. Here superhydrophobic or liquid repellent are the most common properties of the produced surfaces. To get a better overview, I have divided the different surfaces into four categories, depending on the fabrication scheme or working principle.

Clean room based fabrication of wetting controlled surfaces have been the go-to platform many researchers. This is probably due to the discovery of the hierarchical structure on lotus leaves coincides with a rapid development in microelectromechanical systems (MEMS) fabrication. By fabrication of microstructures in a clean room, it is possible to produce surface structures with distinct dimensions and surface chemistry. In turn, this allows detailed study of wetting phenomena related to the microstructures. Microstructures used to study wetting mechanisms are usually created on a wafer in silicon or photoresist covered by fluorinated carbon compounds.[29–32] To replicate the hierarchical structure of lotus leafs, and many other superhydrophobic structures seen in nature, different research groups have applied self-organizing structures on top of lithographically defined microstructures.[14,33,34] The use of overhanging structures has been shown to increase hydrophobicity and stability of the superhydrophobic state.[35] Park et al. have used clean room processes to define and coat microstructures in glass substrate thereby creating superhydrophobic or superhydrophilic surfaces, that are also transparent and anti-reflective.[21]

Polymer replication technologies have been used to create superhydrophobic surfaces, either as an extension of clean room based surfaces or replication of surfaces found in nature. Jeong et al. create a hierarchical structure by using UV curable photoresist in a two-step process, fist imprint microstructures and then, imprint nanostructures on top of the microstructures. In the group of Tapani Pakkanen they use injection molding to create parts with micro and nanostructured surfaces, the molds for these parts are often fabricated without lithographic clean room processes. As molds, they have used alluminum foils microstructured by a micro-working robot, often followed by anodization to obtain overlaying nanostructures.[36–41] Examples of polymer replication using simpler molds are the hairy structures made by pulling polymer foils from sheets of woven metal wires.[42,43] Or direct replication of the surface of plant leafs.[44–46]

Coating is the technology of most commercial interest. This probably due to its compatibility with existing material choices and integration cost. In general coatings can be divided into two categories, those that change the surface structure and those that does not. Coatings that does not alter the surface structure are limited to changing the wetting properties only by chemical modification of the surface. Examples of coatings to create a hydrophobic surface chemistry are Perfluorodecyltrichlorosilane (FDTS), Teflon, P2i, and Liquipel, the latter three being commercial products. These coatings use fluorocarbon to achieve its hydrophobic properties, but the deposition method might vary according to the application in mind. For

coating hearing aids or cell phones the sensitive components as microphones and loudspeakers might be damaged by plasma processing and not by vapor deposition. For coatings that change the surface structure it is possible to create water-repellent surfaces with extreme contact angles, with the best possible water repellent surface produced by Gao.[47]

SLIPS, short for Slippery Liquid-Infused Porous Surface, was first produced by[48] inspired by the working principle of pitcher plants *Nepenthes*.[49] As the name suggests SLIPS works by having a porous surface soaked with a low surface energy liquid, such as fluorinated oil. When a drop of water comes into contact with the oiled surface, the water will not touch the solid surface but instead, rest on oil. Since the oil-water interaction is significantly different than that of solid-water, the water will have little resistance to sliding on the surface. The benefits of this approach is a liquid repellent behavior that is much more stable concerning external influences, such as high pressures or scratches. It has later been shown that SLIPS show excellent anti-icing properties as well as anti-fouling properties.[50,51]

1.2 Design for Manufacturing and High Volume Production

The focus of this Ph.D. project has been to bring the state of the art water repellent surfaces from academia closer to to industry. This is driven by the current lack of technology needed fill the expected markets mentioned in section 1.1.1. The largest challenge for industrial use of surfaces with controlled wetting as I see it is the technology platform. As accounted for in section 1.1.2, most superhydrophobic surfaces are realized by either clean room based silicon technology or surface coatings. Since virtually none of the proposed applications are based on silicon technology only the coating technology is currently adopted in the industry. In the POLYMIC group, we focus on bringing the possibilities from high-tech silicon fabrication to mass production platforms compatible with industrial production. In this Ph.D. project, this platform has been injection molding of parts while other in the group work with roll-to-roll extrusion coating of foils. By using microstructured injection molding tools, we have demonstrated that we are able to mass produce polymer parts with functional surfaces. The direct implementation of microstructures in the mold ensures complete compatibility with industrial production. Since the wetting behavior of the surface is a combination of microstructures and surface chemistry, there is the possibility to combine microstructures with coatings to tailor the functionality of the surface. An advantage of using micro- and nanostructures directly in the mold is that the patterned areas are predefined, in opposition to coating where the coated area needs to be defined on every coated part. For some high-tech applications, the possibility to spatially control the position of microstructures can for a low cost enable features that are very expensive to achieve by masked coating.

In this project I have used a modified lithographie, galvanoformung und abformung (LIGA)[a] process to create polymer parts with micro- and nanostructured surfaces. The LIGA process implies that a structure is defined on a surface by lithography, the structure is then electroplated to create a metal mold. The metal mold is then used for molding high precision parts. By using the LIGA process, it is possible to create molds that have with tolerances governed by the lithography in use. When LIGA was originally invented, X-ray lithography was used to define structures in photoresist, UV-Lithography developed in the microelectronics industry was later accommodated in the LIGA process to reduce costs. Within the POLYMIC group, we have a strong knowledge base using what we call a modified LIGA process, which instead of using structures in photoresist uses structures in silicon

[a] German for Lithography, Electroplating, and Molding

for electroplating. By electroplating silicon structures, we can use all structuring techniques developed by the MEMS industry, enabling fabrication of much more complex structures than possible using UV-LIGA. We initially developed this technique to create molds for mass fabrication of lab-on-a-chip devices and have later turned to create surface structures for functional surfaces.[52,53]

The fabrication of a microstructured surface is a multistep process that can be broken down into the following four categories:

Design. The end product of the design phase is a CAD drawings of masks used in the clean room fabrication, and a detailed process flow. The design phase usually starts based on some model or hypothesis. During the design phase, all steps in the process flow is considered and preferably sketched. Both clean room fabrication and injection molding presents several limitations and depending on the chosen fabrication method there is restraints to the possible design.

Clean room fabrication. During clean room fabrication the steps in the process flow from the design phase is carried out. The simplest possible process consist of lithography, pattern transfer, and electroplating. For more sophisticated designs the process of lithography and pattern transfer may be performed several times and sometimes there might be post processing steps applied, such as oxide growth, to get the desired structures. The end product of the clean room fabrication is a nickel shim that can be used in our injection molding tool. The clean room processes utilized in this project are explained in detail in chapter 3.

Injection molding. The shim from clean room fabrication is mounted in out injection molding tool and used to mold polymer pieces with a microstructured surface. During injection molding, there is usually a significant amount of optimization to get the process running as desired. The injection molding process is explained in detail in chapter 3.

Charcterization. The injection molded samples needs to be characterized for its wettability and fabrication fidelity. In this work SEM and confocal microscopy have been used to characterize the replication fidelity of the microstructures. Contact angle measurements have been used to assess the wetting properties of the surface. The procedure for contact angle measurements is explained in chapter 4.

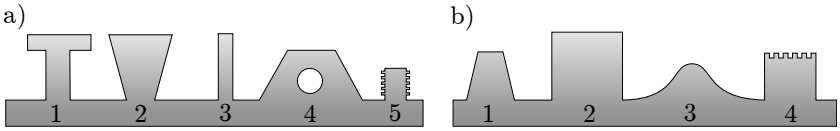

Figure 1.4: a) Structures not possible to realize by injection molding: 1) Overhanging structures, 2) Structures with negative sidewall slope, 3) High aspect ratio structures, 4) hollow structures, 5) structures with roughness on sidewalls. b) Characteristic structures that are possible to injection mold: 1) positively sloped sidewalls, 2) Aspect ratio ≈ 1, 3) smooth curvy structures with positive sidewalls, 4) hierarchical structures with no sidewall roughness.

The injection molding platform put a range of constraints on the structures that can be realized, making it impossible to use structures directly from literature. The main restrictions being an aspect ratio of around one and no overhanging structures. In figure 1.4 I have sketched an ensemble of structures that a) are not possible to mold and b) likely to be molded. In reality, the boundary is not as strict as depicted but the figure is representative for the general guidelines.

Slightly overhanging structures or structures with slightly negative sloped sidewall might be realized in sufficiently rubberlike polymers. A rubberlike polymer would be able to deviate from the molded shape while demolding and then go back into the original shape after detaching the mold.

The limiting factors when molding high aspect ratio structures are both the filling of the structure and the demolding. The filling of the structure can, in general, be achieved by applying heat and pressure. The adhesion between structure and mold needs to be lower than a value set by the mechanical properties of the structure, to demold the structures. High aspect ratio wall like structures are significantly easier to mold than pillar-like structures, both when filling and demolding. The difference in filling can be exemplified by the hydraulic resistance for a circular cross section and a rectangular cross section

$$R_h^{\circ} = \frac{8\mu L}{\pi R^4} \quad , \quad R_h^{\square} \approx \frac{12\mu L}{wt^3(1-0.63t/w)} \quad \text{assuming} \quad t < w, \tag{1.1}$$

where μ is the viscosity, L is the height of the structure, R is the radius of the circular cross-section, w and t are the width and thickness of the wall, respectively. The two expressions scale with the critical dimension of the structure, radius for pillars and thickness for walls, to the power of the -4 and -3, respectively. This difference in scaling makes a huge impact when producing structures on the micro- or nanometer scale. Of course the process of filling a micro- or nanostructure is in reality much more complicated than the laminar flow in a well-defined channel, but I would argue that the scaling would still apply to the real system. For any industrial molding process, the design guideline is an aspect ratio on one for pillar-like structures.

The hierarchical structure depicted in figure 1.4 b4 is marked as possible, and it is, but it is not at all straightforward. The mold is filled by injecting molten polymer at very high temperatures, typically $> 250°C$, into a much cooler mold, usually $< 100°C$.[b] Since the mold is made of metal, with a high thermal effusivity, the polymer that comes in contact with the mold surface will cool rapidly. If the mold temperature is below the no-flow temperature of the polymer, it will solidify, if it is above it will still flow but with a drastic increase in viscosity. This phenomenon, called a skin layer, will inhibit filling of microstructures in general, but especially nanostructures on top of microstructures. A schematic drawing of the formation of the skin layer is illustrated in figure 1.5.

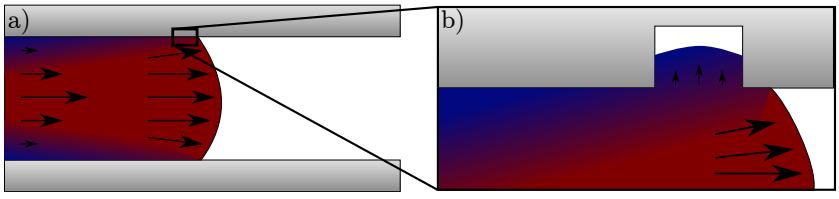

Figure 1.5: a) Flow of molten polymer in a macroscopic mold channel. The polymer in contact with the mold surface quickly cools, forming a skin layer. b) A zoom in on a microstructure in the mold surface. The rapid cooling of polymer will freeze the polymer, hindering complete filling of the microstructure.

When comparing the silicon structures referred to in section 1.1.2 with the restrictions posed by injection molding it is clear that none of these structures are directly compatible

[b] These temperatures depend heavily on the polymer used and desired product. They are only taken to illustrate the large temperature difference

with this production platform. A lot of work in this Ph.D. project have been devoted to fundamental research on wetting of structures that are possible to realize by injection molding. The insights from this research can be used to decide the design of structures depending on the application in mind.

1.3 TransForm Structures

Early in my Ph.D. I invented, together with Carl Esben Poulsen and others, what we later called TransForm structures. These structures showed remarkable water repellency, and could be produced by a relatively fast injection molding process. In figure 1.6 there is two SEM micrographs showing typical structures in mold and polymer.

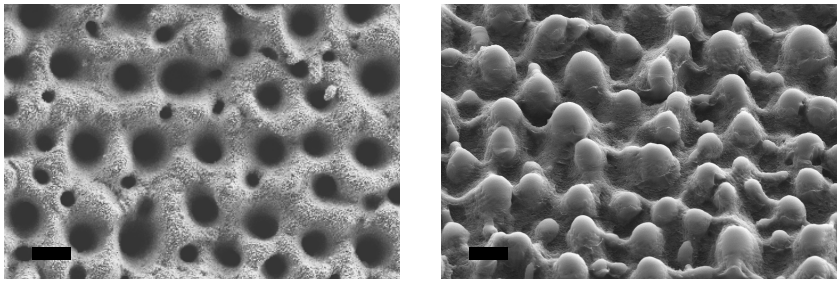

a) b)

Figure 1.6: SEM micrographs showing typical TransForm Structures. a) mold surface in aluminum. b) Molded polymer part in polypropylene (PP). Scale bar is 10 μm.

When comparing with state of the art superhydrophobic surfaces it was quite surprising that these structures were super hydrophobic and water repellent. In contrast to most other superhydrophobic surfaces these were not hierarchical structures. The surface instead consist of micro bumps with very smooth rounded tops, arranged in a way similar to that of structures on water repellent leaves. A comparison between transform structures and the surface structures on the leaf of the lotus flower is shown in figure 1.7. From this, the distribution of structures is recognizable, the structures are not ordered in latices but have an inter structure distance with a narrow distribution. In contrast to the lotus flower the TransForm structure does not have nanostructures on top of the microstructures but have the same rounded shape of the pillar tops. From the SEM images it also looks like there is a distribution of structure heights, so liquid coming in contact with the surface might not touch all microstructures.

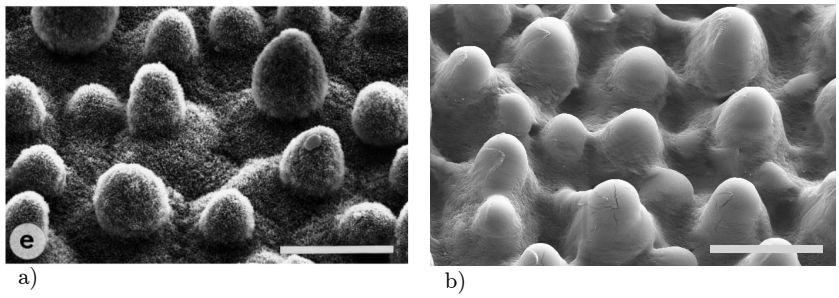

a) b)

Figure 1.7: SEM micrographs of a) leaf of the lotus flower, from[7] b) Molded polymer part in PP. Scale bar is 20 μm.

The TransForm structures served as an inspiration for several designs published in this

Ph.D. This was however not mentioned in the papers due to the process of patenting the TransForm structures.

2

Wetting of surfaces

The fundamental physical property giving rise to all wetting phenomena is the energy associated with interfaces. Most materials have its minimum energy when binding to itself and thus creating interfaces to different materials costs energy. For solid materials, this is only observable when cleaving the material. For a cleaved rigid material the energy required to rearrange its structure is usually larger than the energy associated with its interfaces. A liquid is, however, able to reorganize its physical structure at very low energy cost and will thus minimize its energy by minimizing its surface. The energy cost of an interface can be viewed as the sum of the energy of the missing bonds between the atomically dense fluid and atomically light vapor, as illustrated in figure 2.1. This difference in density means that the macroscopically observable behavior is caused by differences in the materials on the atomic scale. The atomic scale origin results in very sharp transitions between liquid and gas with an interface thickness of a few nanometers.[54]

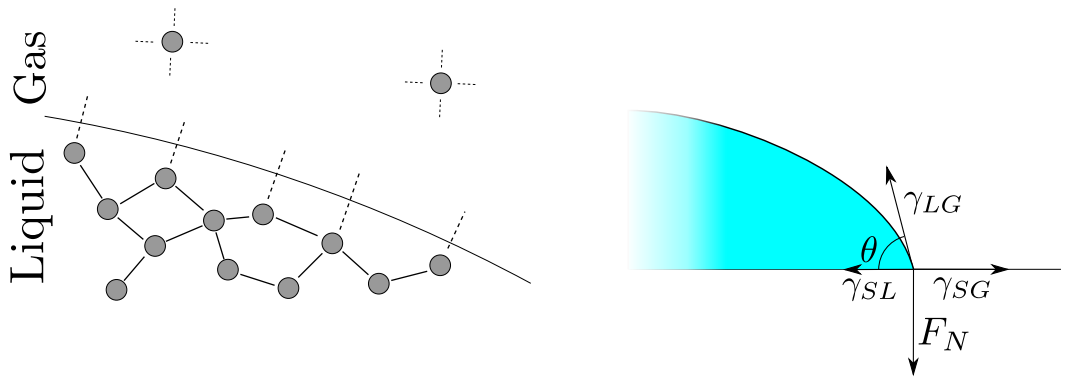

(a) **(b)**

Figure 2.1: (a) Illustration of the dangling bonds at a liquid-gas interface due to the difference in density. (b) A classical force diagram drawn to explain the Young's equation, showing the three surface tensions of a three phases system. Drawing is from[55]

2.1 Classical Models

When a drop of liquid rests on a surface surrounded by another fluid, e.g. gas, the minimization of energy will result in a given contact angle between solid and liquid. In 1805 it was proposed by Thomas Young that all liquids forms a specific contact angle that can be

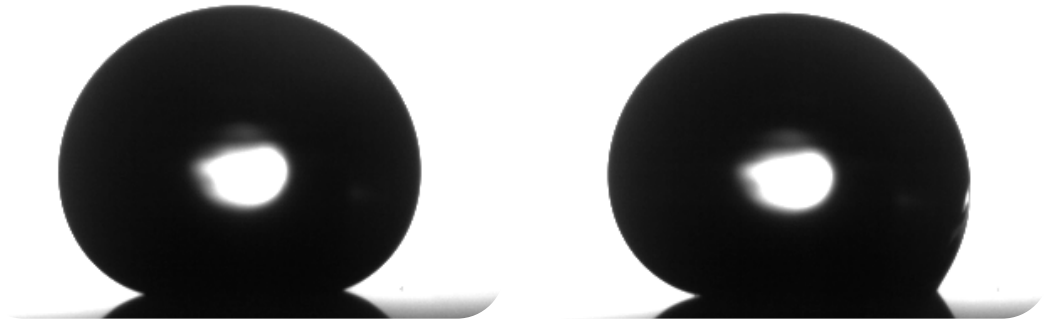

(a) Horizontal surface **(b)** Surface tilted 10 deg

Figure 2.2: Two images of a sessile drop in profile. By tilting the surface it is evident that the contact angle have a range of different values.

calculated by the force balance in figure 2.1b. The contact angle was thus claimed to be a direct result of the specific interfacial energies in the three phase system.[56] The separate surface energies act as line forces on the triple line resulting in the force diagram in figure 2.1b. The contact angle for a system with know surface energies can from 2.1b be calculated by the Young's equation

$$\cos(\theta_Y) = \frac{\gamma_{sg} - \gamma_{sl}}{\gamma_{lg}}, \tag{2.1}$$

where γ_{ij} is the surface tensions between solid, liquid, and gas, θ_Y is known as Young's contact angle. This theoretical reflection has since 1805 been used in different fields of science to measure and predict a range of properties. The surface energy of solids are often determined through measurements of the contact angle of sessile drops, and phenomena as the capillary rise are described using the contact angle. The very simple theory presented by young can despite its extensive use easily bee proven wrong. By tilting a surface with a drop it is evident that the contact angle at the left (downhill) side is different than the contact angle at the right (uphill) side, see figure 2.2. Continuity along the triple line dictates that the drop in figure 2.2b exhibits all the contact angles in between the contact angle of the downhill and uphill sides. The phenomena that allow a drop to have a range of different contact angle is referred to as contact angle hysteresis. The concept of contact angle hysteresis implies that there exist a maximum contact angle that the liquid can have before it starts advancing over the surface and a minimum contact angle before receding over a surface. The maximum and minimum contact angles are referred to as the advancing and receding contact angles. The origin of contact angle hysteresis is a very debated subject in literature and have been ascribed to

- surface roughness[57–59]
- micro- scopic chemical heterogeneity[10,59]
- drop size effect[59,60]
- molecular reorientation[59,61]
- physical deformation of the surface at the triple line[61,62]
- pinched off droplets at the receding edge[31]
- the penetration of the liquid molecules into the solid surface[59,63]
- activation energy from related to breaking and forming bonds between solid and liquid[64]

The vast amount of contributions to contact angle hysteresis render it virtually impossible

to find any surfaces that do not show contact angle hysteresis, with the exception of a few highly engineered surfaces.[47,65] One should therefore always assume contact angle hysteresis to play a significant role in the wetting of any real surface.

When placing a drop on a solid surface the triple line does not move across the surface unless the contact angle is outside the interval defined by the advancing and receding contact angle. It is, therefore, highly unlikely that a drop placed on a solid surface will show the Young's contact angle. If the drop is placed with a contact angle within the interval between receding and advancing contact angle it will not reconfigure to the Young's contact angle, instead it will show an as-placed contact angle. It is well known that the measured static contact angle depends on the deposition method[58] and is thus questionable whether the static contact angle can be used for calculation of surface energy etc. To overcome this issue, a way of calculating the Young's contact angle from the advancing and receding contact angles have been suggested.[66]

2.1.1 Wenzel model

Following the idea of Young's contact angle, Wenzel[57] introduced roughness into the calculation of contact angles. When a surface is rough the surface area is increased compared to a flat surface. The increase in surface area can be described by the roughness factor r defined as

$$r = \frac{\text{Actual surface area}}{\text{Projected surface area}}. \tag{2.2}$$

The modification to Young's equation is done by calculating the forces at the triple line with an increased contribution from the solid-liquid and solid-gas interfacial energy due to the roughness induced increase in energy density. This increase in energy results in a different contact angle, as shown in figure 2.3, only accounting for the lateral forces. By equating the lateral forces, it is straight forward to arrive at the Wenzel equation

$$\cos(\theta_W) = r\cos(\theta_Y). \tag{2.3}$$

With θ_W being the Wenzel contact angle. According to the Wensel equation, the contact angle on rough surfaces will decrease for $\theta_Y < 90°$ and increase for $\theta_Y > 90°$ compared to a flat surface.

It is important to note that in the derivation of the Wenzel equation it is assumed that the forces at the triple line scales with the energy density of the surface. This assumption only holds when the roughness is randomly distributed and when the projection of the triple lines on flat and rough surfaces coincide.

2.1.2 Cassie-Baxter model

Cassie and Baxter later expanded the Wenzel model to include heterogeneous surfaces with the purpose of explaining why fabrics and bird feathers often show water repellent properties.[10] The Cassie-Baxter model is based on energy calculations where they consider the changes in energy required to wet a heterogeneous surface. Figure 2.4 shows a schematic drawing

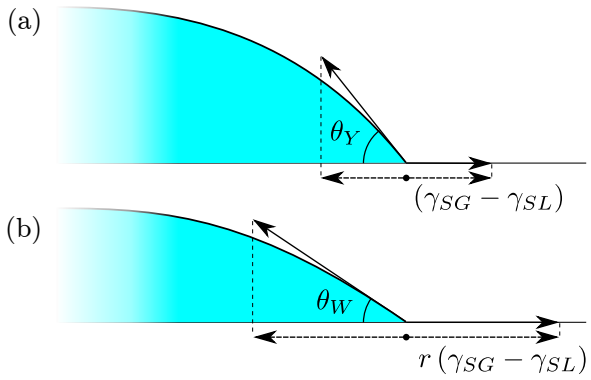

Figure 2.3: Force diagram for triple line for: (a) Flat surface showing the Young's contact angle, (b) a rough surface showing the Wenzel contact angle.

of water wetting a porous surface created by a mesh of fibers. The liquid interface per unit area now consists of surface fractions f_1 and f_2 for solid-liquid and liquid-gas interfaces. By calculating the energy required to wet a unit area $E_P = f_1(\gamma_{sl} - \gamma_{sg}) + f_2\gamma_{lg}$ and substituting this into equation 2.1 replacing the energy needed to wet a flat surface $E_F = \gamma_{sl} - \gamma_{sg}$ one arrives that the Cassie-Baxter equation

$$\cos(\theta_{CB}) = f_1 \cos(\theta) - f_2, \tag{2.4}$$

where θ_{CB} is the advancing or receding contact angle of the surface calculated by using the advancing or receding contact angle for the flat material as θ. In the more general case where the surface is not porous but consists of materials with different surface fractions and contact angles, f_i and θ_i equation 2.4 generalizes to[67]

$$\cos(\theta_{CB}) = \sum_{i=1}^{n} f_i \cos(\theta_i). \tag{2.5}$$

In the original paper by Cassie and Baxter they use equation 2.4 to accurately predict the advancing and receding contact angles of water on meshes consiting of metal wires that have been coated with wax to obtain a uniform hydrophobic surface chemistry. When comparing with experiments, they note that the equation does not hold if the angle between mesh fibers and moving triple line is less than 6°. When the mesh fibers are perpendicular to the direction of triple line movement the surface factions at the triple line will vary during movement. For the Cassie-Baxter equation to hold, they state that an infinitesimal change in the wetted area δA the changes in the interfacial area should be $f_i \delta A$ for all interfaces. This constraint is in line with the origin of wetting behavior that even though area properties describes a surfaces it is the conditions at the triple line that determines the dynamic contact angles. For many microstructured surfaces created using lithography, it evident that the triple line does not follow predictions using the area fractions of the surface, but rather line fractions.[68,69]

Although the Cassie-Baxter state was described for liquid on meshes, it is directly applicable to porous or microstructured surfaces. A drop on a microstructured surface is considered to be in the Cassie-Baxter state if it rests on top of the surface structures as illustrated in figure 2.5a. A drop resting on top of the structures, not wetting the structures, will generally

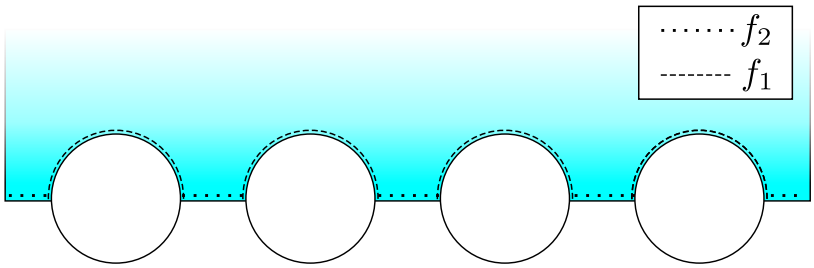

Figure 2.4: Schematic of the original model by Cassie and Baxter. When wetting a heterogeneous surface the interfacial energies scales with the surface fractions f_1 and f_2.

have lower resitance to moving on the surface than a drop in the Wenzel state, wetting the structures. The distinction between the non-wetting Cassie-Baxter state and the wetting Wenzel state rapidly becomes more unclear for a real surface. In reality, a drop on a microstructured surface would rarely be in a pure Cassie-Baxter state but rather in some hybrid state.[2,70,71] In figure 2.5b five wetting states of a surface with hierarchical microstructures are shown as examples. For more complex surface structures there are even more permutations. State 5 in figure 2.5b is often referred to as petal state or impregnating Cassie state, named after the wetting of rose petals with high contact angle and high adhesion.[72]

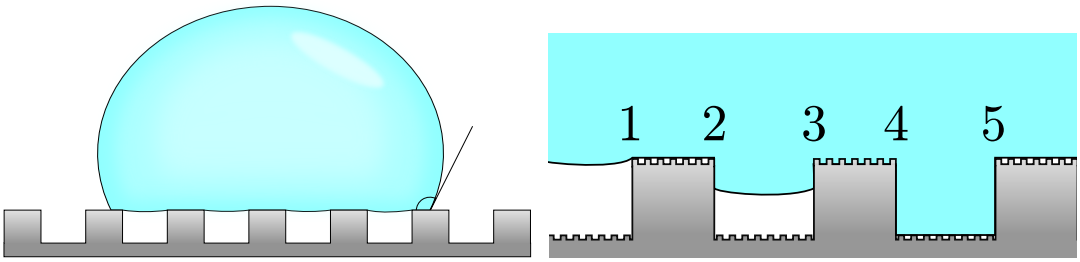

Figure 2.5: (a) Drop resting on micro structured surface in a pure Cassie-Baxter state. (b) Wetting states for drop on hierarchically structured surface. 1) a pure Cassie-Baxter state (non-wetting) on both small and large structures. 2) non-wetting of small structures partial wetting of large structure. 3) Wetting of uppermost small structure and large structure, non-wetting of small structures between large structures. 5) Wetting of large structure, non-wetting of small structure.

2.1.3 Transition from Cassie to Wenzel

It is widely accepted that the driving mechanic behind most water repellent surfaces seen in nature is maintaining all drops on the surface in the Cassie-Baxter state.[7,15,16,18,32,37,42] Much research has therefore been devoted to describing the mechanisms that lead to a collapse of the Cassie-Baxter state, a so-called wetting transition.[2,73–76] Wetting transitions can happen on many time scales and via different mechanisms depending on the circumstances. When simplified there is often the distinction between two basic types of wetting transitions, a sagging transition and a depinning transition, as illustrated in figure 2.6. To stabilize the Cassie-Baxter state to the sagging transition, the structures should be densely packed and as

tall as possible. To prevent wetting through the depinning transition, different groups have employed a variety of strategies, primarily to increase the advancing contact angle at the sidewall or producing sidewalls of negative slope[75]. In both cases to increasing the required applied pressure needed for reaching the advancing contact angle.

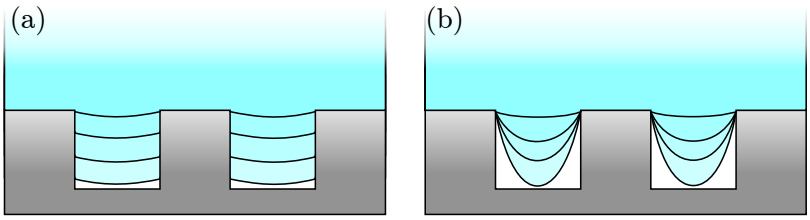

Figure 2.6: Illustration of the two basic wetting transitions. (a) The depinning transition, where the contact angle on the side walls equals the advancing contact angle, and the triple line moves down. (b) The sagging transition, where the triple line is pinned at the apex of the structure and the applied pressure forces the meniscus to the bottom of the trench.

2.1.4 Young-Laplace equation

In the previous sections, we have looked at the force exerted by the surface tension on the triple line as depicted by Young. This picture was adapted by Pierre Simon Laplace and used to derive what is know as the Young-Laplace equation for the pressure difference across curved liquid-gas interfaces. This pressure difference is called the Laplace pressure. The origin of the Laplace pressure arrives from the surface tension, that not only exert a force at the triple line but at all lines in the surface. This pull is a force per line with equal magnitude in all directions parallel to the surface. On a flat surface, the net force on an infinitesimal area is zero whereas a curved surface creates an uncompensated normal force. This is schematically drawn in figure 2.7 with the curvature of the surface described by the radii of curvature R_1 and R_2.

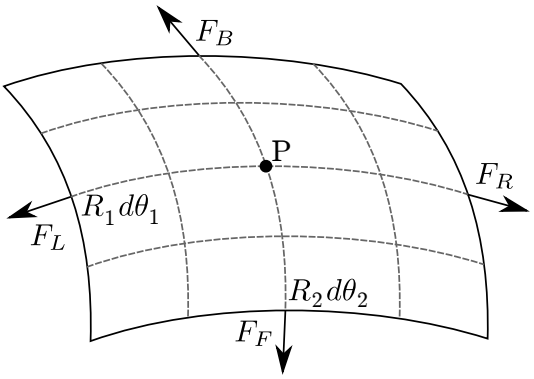

Figure 2.7: Force diagram for an infinitesimal surface area. The curvature creates uncompensated forces normal to the surface. This normal force per area is know as the Laplace pressure.

To find R_1 and R_2 at a point P the surface is cut in mutually orthogonal planes intersecting each other in the normal to the surface. The radii of curvature are the radii of two circles in the two planes approximating the surface profile. The radii of curvature are treated as algebraic quantities and are defined as positive if the center of the circle is under the surface

and negative if the center is over the surface. By integrating the force per line around the perimeter of the infinitesimal area and dividing by area on arrives at the Young-Laplace equation for the pressure difference across surface

$$\Delta P = \gamma_{lg} \left(\frac{1}{R_1} + \frac{1}{R_2} \right). \tag{2.6}$$

2.1.5 Capillary Rise

In a capillary rise experiment, one puts a capillary tube into a liquid. Due to the wetting properties of the system the liquid level inside the capillary tube will differ from the liquid level around the tube. For a tube-liquid combination that has a contact angle $> 90°$ the liquid inside the tube lowers compared to the liquid around, for contact angles $< 90°$ the liquid in the tube will rise. The distance that the liquid height, H, differs from the surrounding liquid can be calculated by the well known Jurin's law

$$H = \frac{2\gamma_{lg} \cos(\theta_Y)}{\rho g R}, \tag{2.7}$$

with ρ being the density of the liquid, g the gravitational acceleration and R the radius of the capillary tube. In the derivation of equation 2.7 it is assumed that $R << H$, if this is not the case there have been found several correction terms. There are at least three different approaches to deriving Jurin's Law:[77]

1 Minimize the energy of the system consisting of a wetting energy and a gravitation energy, $E = E_W + E_G$. The energy associated with wetting of the tube walls can be calculated as, $E_W = 2\pi RH(\gamma_{SL} - \gamma_{SG})$, and the gravitational energy in the liquid column as, $E_G = \frac{1}{2}\pi R^2 H^2 \rho g$. By minimizing the energy of the system and substituting surface tensions via equation 2.1 on arrives at equation 2.7.
2 Assume that the contact angle of the liquid in the tube is the Young's contact angle, this forces the liquid to form a meniscus of a specific curvature, $R/\cos(\theta_Y)$. Through equation 2.6 this creates a pressure $p_C = \frac{2\gamma_{LG}\cos(\theta_Y)}{R}$ that in equilibrium is equated with the hydrostatic pressure $p_H = \rho g H$.
3 Calculate the force balance between the gravitational pull and the surface tension at the triple line in the tube. The force at the triple line is found as $F_T = 2\pi R\gamma_{LG}\cos\theta$ whereas the gravitational pull on the water column sums up to $F_G = \rho g \pi R^2 H$.

The different derivations correspond to different ways of describing wetting. In the first derivation, the wetting is controlled by interfacial energies from areas. In the second, the contact angle forces the liquid meniscus to bend and thereby generate a pressure difference over the meniscus. In the last, the water column is raised by the forces pulling at the triple line. Although all derivations end up at the same result, I prefer the image in the third derivation, that the forces at the triple line govern the wetting of a system.

2.2 Modern models

After Cassie, Baxter and Wenzel proposed their models of wetting there were a couple of decades without many improvements to the understanding of wetting phenomena. At the end of the 20th century, the development of computers, digital cameras, and improvement to surface probing techniques created the opportunity to get a better understanding of the

subject. After discovering that the superhydrophobicity of lotus leaves arise from a particular micro- and nanostructure and the possibility to use microstructuring techniques to design surface structures, the scientific interest in wetting increased dramatically. The growing scientific interest naturally leads to new understandings that have led to several modern theories of wetting. Of these, I prefer the following two models when describing wetting in general and dynamics of drops in the Cassie-Baxter state. I have chosen these due to the sound reasoning of their arguments combined with high-quality experimental proofs.

Shanahan De Gennes wetting theory, originally published in french[78] suggests that parts of contact angle hysteresis are related to normal force in the force diagram by Young in figure 2.1b. For the surface to generate such force the molecules at the triple line are distorted and will rearrange to minimize their energy. In Liquid-Gas-Gel systems it is easy to see that the gel deforms at the triple line due to the pull from the liquid-gas surface tension. Experimentally this was later shown by Tadmor by measuring the centrifugal force required to slide a drop across an atomically flat surface.[62] The force needed to move a sessile drop was in this experiment shown to be less for a sessile drop compared to a pendant drop. For a pendant drop the gravity pull is in the same direction as the $\gamma_{lg}\sin(\theta)$ component and is thus compensated by a larger normal force than for a sessile drop. It might seem surprising that drops that are being pulled normal to the surface require higher force to move in the lateral direction since friction between solid objects behave in the opposite way. In this, and other, papers Tadmor also shows that the lateral force required to move a drop increases over time until reaching some maximum limit.[62,79,80] The time it takes to reach the plateau is defined by the physical properties of the solid and the time it takes for molecules to rearrange.

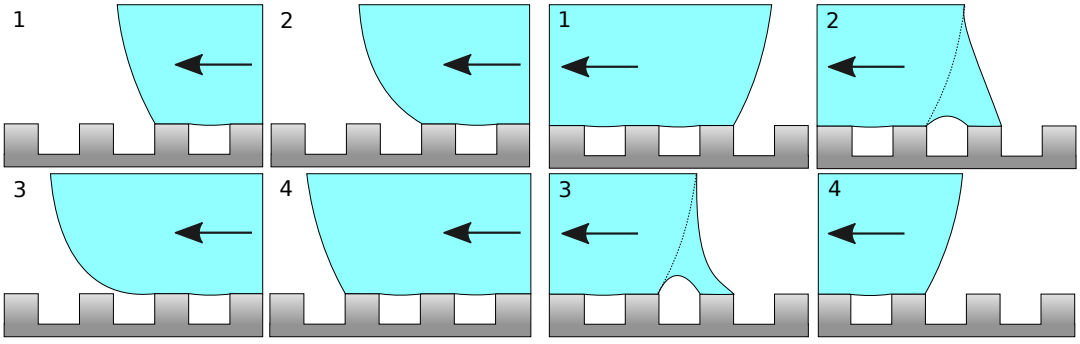

(a) Advancing triple line **(b)** Receding triple line

Figure 2.8: Schematic drawing of the triple line advancing (a) or receding (b) over a microstructured surface. On the advancing side the the liquid can only get to the next structure by tipping over, resulting in a advancing contact angle of $\theta_a = 180°$. On the receding side the drop needs to detach each pillar, ofen resulting in microscopic capillary bridges.

In 2013 Paxson and Varanasi published the paper Self-similarity of contact line depinning from textured surfaces.[33] In the paper they image a drop moving across a micro-textured surface by environmental scanning electron microscope (ESEM). Their findings are schematically shown in figure 2.8 for bot advancing and receding side of a drop. This shows that if a drop is in the Cassie-Baxter state on a microstructured surface with disconnected structures there is a significant difference between the advancing and receding side of the drop. On the advancing side of the drop, the only way the triple line can get to the next post is by tipping over. This process imposes that the advancing contact angle is always 180°. On the

receding side, the triple line needs to detach each post individually, often by forming capillary bridges due to pinning. The fact that the advancing process is the same for all disconnected structures, which most superhydrophobic surfaces have, implies that drop movement only depends on the depinning process of the receding triple line. The two design criteria when creating a superhydrophobic surface should, therefore, be a stable Cassie-Baxter state and small pinning of the the triple line. The property of self-similarity from the title of their paper refers to their postulate that this process is the same on all length scales, an important feature when designing surface structures with multiple length scales.

2.3 Simulating wetting of submerged structures

For many imagined applications of superhydrophobic surfaces, it is necessary to assess the stability of the Cassie-Baxter state as it is the key to maintaining superhydrophobicity. In the simple case, this could be to determine the water column pressure required for initiating the transition from the Cassie-Baxter state to the Wenzel state. To observe the wetting transition on submerged surfaces, Emil Søgaard fabricated a pressure cell where it was possible to observe the wetting at various pressures. The pressure cell was designed to hold a 2 mm thick ø50 mm disk which is the standard format from our injection molding machine. By doing experiments with submerged pillar-like structures, it was clear that the wetting transition starts at a single spot and then propagates like described by Papadopoulos.[71] In the injection molding process, it is challenging to avoid defects in the finished parts completely. Such defects would initiate the wetting and in time wet the whole surface. The published experiments included at the end of this chapter was, therefore, all conducted using separated hole-like structures to prevent propagation of the wetting transition. Separation both includes that the triple line is discontinued between holes and also the air trapped in each hole is unable to flow to neighboring holes. The wetting transition of these separate microcavities was studied by optical transmission microscopy while being submerged in pressurized water.

The samples used in for optical transmission microscopy were all molded in cyclic olefin copolymer (COC) (TOPAS grade 8007-s04). For a wetting transition in a hole with a diameter of 15.5 μm, the maximum hole size in the experiment, and an advancing contact angle of 102° the maximum deflection of the meniscus is $d = r \tan\left(\frac{\theta_a - \pi/2}{2}\right) = 0.81\,\mu$m. With a hole depth of 3.2 μm it is most likely that the wetting transition will occur by depinning rather than sagging since the Laplace pressure needed for the sagging transition is enormous. To model the wetting transition of a submerged hole the one might look at the similarities with a capillary rise experiment. In section 2.1.5 it was presented how a liquid intrudes into a wetting capillary tube until gravitational pull balances the forces. In the submerged pressurized wetting experiment the liquid is forced into a nonwetting cavity until gas pressure in the microcavity balances the forces. In a time-resolved simulation, the increased gas pressure in the microcavity will result in gas diffusing from the gas phase into the liquid phase. The diffusion of gas will subsequently reduce the gas pressure in the microcavity leading to a new equilibrium position of the liquid-gas interface. This is schematically depicted in figure 2.9.

The experiment carried out by Emil Søgaard[2] counts the number of holes that are almost filled, being the impregnating Cassie state, and completely filled, being in the Wenzel state. A large array of $N_{holes} \approx 70$ is used in each experiment, with all experiments being repeated tree times. The holes start filling at a particular pressure given by the maximum

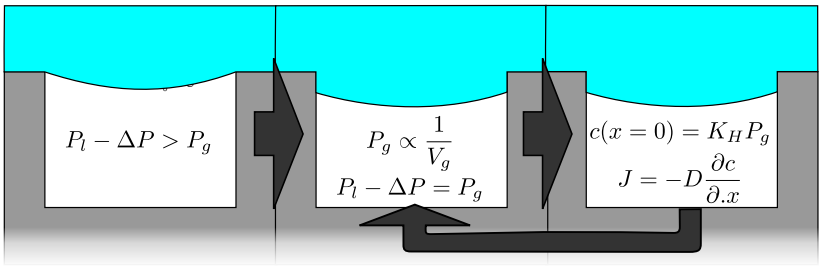

Figure 2.9: Schematic drawing of the physical system through the simulation. a) The applied pressure forces the meniscus to curve. If the resulting contact angle is above the advancing contact angle, the triple line moves. b) The triple line moves until the increasing gas pressure balances the applied pressure. The pressure in the cavity scales inversely with the volume. c) Due to the increased pressure in the cavity the gas will diffuse into the liquid, this is governed by Fick's law of diffusion and Henry's law as boundary condition.

Laplace pressure that the meniscus can support before the contact angle at the edge exceed the advancing contact angle of the system. After the onset of wetting the limiting factor is the flux of gas from the cavity into the liquid. In reality, there are small differences between the holes that will promote wetting of some holes before others. Since the limiting diffusion length is the thickness of the water layer above the cavity, $b = 0.5\,\text{mm}$, and the hole to hole distance is $15\,\mu\text{m}$, nitrogen diffusing from one hole would quickly saturate the water above adjacent holes, see figure 2.10. It is, therefore, reasonable that small differences in wettability will result in holes filling one by one instead of all at the same time. The total uptake of nitrogen and thereby the concentration in the water is the same whether all holes are 10% filled or 10% of the holes are filled and the rest empty.

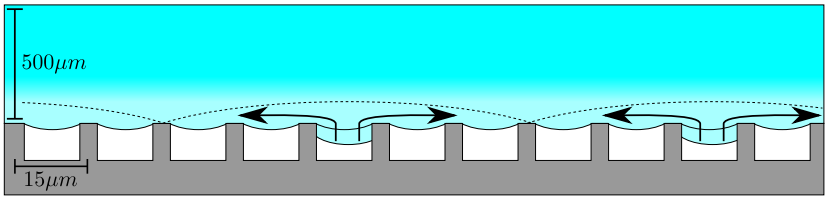

Figure 2.10: Schematic drawing of the diffusion of nitrogen in the water layers closest to the cavities. Due to slightly different wettability of the cavities, some will fill before others. The air from these holes will quickly saturate the water above neighboring cavities thereby preventing these from filling.

The simulation is set up as a time dependent system where the physical observations are used to set the initial conditions. It is possible to implement time-dependent system parameters such as an applied pressure that are a function of time. The simulation is carried out by setting the initial conditions and then updating all physical parameters at sufficiently small time steps until the system reaches equilibrium and there are no changes in the physical parameters. Script-wise it is implemented as a master script where the physical system is defined, the master script then calls a range of functions that runs the simulation. The simulation was carried out in MATLAB with the code included in Appendix A.

The system is set up to consist of a layer of water with an atmospheric equilibrium concentration of nitrogen and a microcavity with nitrogen at atmospheric pressure. The

geometry of the microcavity is defined by a volume V_0 and a radius R. At the start of the simulation, the whole microcavity is filled with gas so that the volume of the gas equals the volume of the microcavity, $V_g = V_0$, as the cavity fills the volume of gas will shrink. A normalized filling of the cavity can thus be calculated by

$$f = \frac{V_0 - V_g}{V_0}, \tag{2.8}$$

where $f = 0$ and $f = 1$ corresponds to a cavity filled with gas and liquid, respectively. The initial gas pressure in the cavity is set to $p_g^0 = 1\,\text{bar}$ and with the applied pressure also being measured to a reference of 1 bar the pressure in the liquid is set as $p_l = p_a + 1\,\text{bar}$.

The variables describing the physical system updates in each time step, this is done in two stages in a loop.

a) Calculate the maximum Laplace pressure that the meniscus can support before the triple line is forced to move,

$$\Delta p_{LP}^{max} = -2\gamma_{lg}\frac{\cos(\theta_A)}{R}. \tag{2.9}$$

If the pressure difference across the meniscus, $\Delta p = p_l - p_g$, is larger than the maximum Laplace pressure, $\Delta p > \Delta p^{max}$, the triple line is forced to move. When moving the volume of gas reduces from V_g to V_g^* thereby increasing the pressure from p_g to p_g^* by the relation

$$p_g V_g = p_g^* V_g^*, \tag{2.10}$$

using the ideal gas law assuming an isotherm process. The triple line will move until the maximum Laplace pressure can support the difference between applied pressure and gas pressure,

$$\Delta p_{LP}^{max} = p_l - p_g^*. \tag{2.11}$$

Using equation 2.8 and 2.10 the updated filling f^* can be calculated as

$$f^* = \frac{V_0 - V_g^*}{V_0} = 1 - \frac{p_g V_g}{V_0\left(p_l - \Delta p_{LP}^{max}\right)} \tag{2.12}$$

where p_g and V_g are pressure and volume from last iteration.

b) With the pressure increase in the cavity the equilibrium concentration of nitrogen in the water increases. The equilibrium concentration of gas dissolved in liquid is calculated by the well known Henrys law[81]

$$c_h = k_H p \tag{2.13}$$

where c_h is equilibrium concentration of gas dissolved in the liquid, p is the partial pressure of the gas and k_H is the Henry's constant for the liquid gas combination of interest. For nitrogen in water at room temperature we use $k_H^N = 1640\,\frac{\text{Lbar}}{\text{mol}}$. We assume that the only gas in the micro cavity is nitrogen so $p = p_g$. With an increase in the equilibrium concentration the gas will start to diffuse into the liquid column governed by the diffusion equation in 1D

$$\frac{\partial c}{\partial t} = D\frac{\partial^2 c}{\partial x^2}. \tag{2.14}$$

Where D is the diffusion coefficient for the gas in liquid. For nitrogen in water at room temperature we use $D^N_{H_2O} = 1.8 \cdot 10 - 8 \frac{\mathrm{m}^2}{\mathrm{s}}$. In order to use equation 2.14 in a numerical implementation it needs to be rewritten into discrete form where the continuous concentration $c(x,t)$ is discretized into a grid with spacing of dx and dt,

$$c(x,t+dt) = c(x,t) + D\left(c(x-dx,t) + c(x+dx,t) - 2c(x,t)\right)\frac{dt}{(dx)^2}. \tag{2.15}$$

The concentration can thus be described by a N by M matrix where N is the number of spatial grid points and M is the number of temporal grid points. In the discrete form it is possible to calculate the next concentration profile given the current concentration profile and proper boundary conditions. The boundary conditions enters equation 2.15 when calculating either first or last element of the vector describing the concentration at a given time. For the first element concentration vector is assumed connected to a reservoir with the equilibrium concentration, $c(x \leq 0) = c_h$, whereas the last element have a zero flux boundary condition imposed by $c(x > N) = c(x = N)$. The vector $c(c,t)$ with added boundary conditions used as input in equation 2.15 is thus

$$c_{bc}(c,t) = [c_h, c_1, c_2, c_3, ..., c_{N-2}, c_{N-1}, c_N, c_N] \tag{2.16}$$

Although the concentration at the liquid-gas interface is modeled as a reservoir of constant concentration the flux of molecules between gas and aqueous phase will change the number of molecules in gas phase, thereby change the pressure. The flux of molecules into the liquid can be calculated by the change in concentration times the volume of the liquid, $dn = \overline{(c(t+dt) - c(t))}V_l$, where V_l is the volume of liquid and $n_g(t)$ is the number of molecules in the gas phase. The change in pressure is again calculated by the ideal gas law assuming an isotherm process

$$P_g(t+dt) = P_g(t)\frac{n_g(t) - dn}{n_g(t)}. \tag{2.17}$$

If the flux of molecules into the gas have reduce below a certain threshold $dc < \epsilon$ or the filling is complete, $f = 1$, the simulation ends. If this is not the case the script returns to point **a)**.

This simple model can accurately describe the filling of microcavities given a constant pressure and a well-defined geometry, as plotted in figure 4a on page 31. For low pressures, $p_a \leq 225\,\mathrm{mbar}$, with little filling, the accuracy is slightly worse than for the higher pressures, $p_a \geq 300\,\mathrm{mbar}$, with higher filling. The difference in accuracy I expect is due to the differences of simulating the gradual filling of one hole while measuring binary filling of many holes. In the case that some holes are half filled during the experiment they will be counted as being in a pure Cassie-Baxter state. For a high percentage of filled holes, this would induce a relatively small error while for little filling it would drastically change the amount of dissolved gas in the water layer.

When having a numerical model that accurately predicts the behavior of the system it is straightforward to illustrate what factors governs the filling of holes. In figure 2.11 the filling of a ø15 μm hole of depth 3.4 μm with an applied pressure of 300 mbar is plotted for various water volumes and diffusion constants. This corresponds to the second graph in figure 4 in the paper, page 31, labeled 300 mbar. It is evident from figure 2.11a that increasing the volume of water above the microcavity will increase the maximum level of filling by increasing the total amount of nitrogen that can be dissolved in the water at a specific concentration. By increasing the volume above the limit needed for complete filling, the increased volume will

reduce the filling time to some lower bound. The decrease in filling time can be explained by imagining two extreme situations, one where the water volume is exactly large enough to contain all the nitrogen atoms and one with an infinite water volume. In the case of a finite volume, the concentration of nitrogen needs to be constant throughout the volume. According to Fick's first law, that the diffusive flux is proportional to the concentration gradient, it would take an infinite time to reach such a situation. In the case of an infinite liquid column, the concentration will follow a distribution described by the error function and will never be affected by the zero-flux boundary condition at the upper wall. In such a case the time it takes to dissolve all nitrogen molecules in water is given solely by the diffusion constant. In figure 2.11b the result of increased diffusion constant is plotted. As expected by the previous analysis the increased diffusion rate decreases the time it takes to reach maximum filling but does not alter the value of maximum filling.

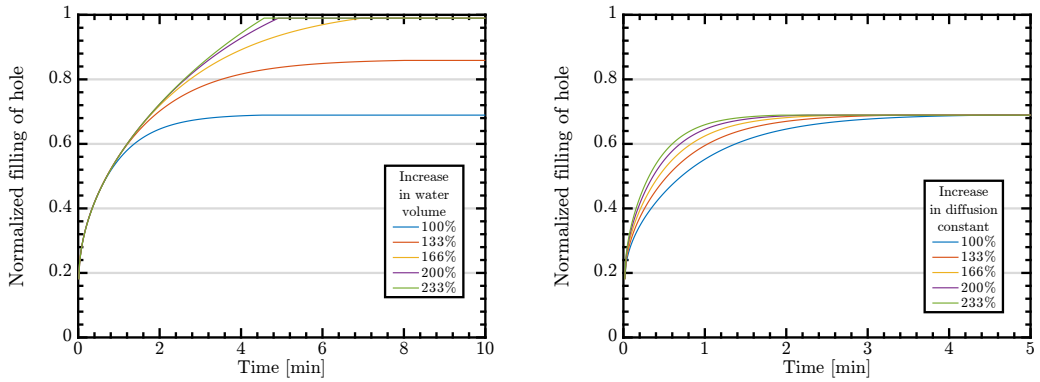

(a) Filling for different water volumes. **(b)** Filling for different diffusion constants.

Figure 2.11: Simulation results from increasing the a) volume of water column and b) value of diffusion constant. Increased volume increases maximum filling whereas increased diffusion constant decreases time to achive maximum filling.

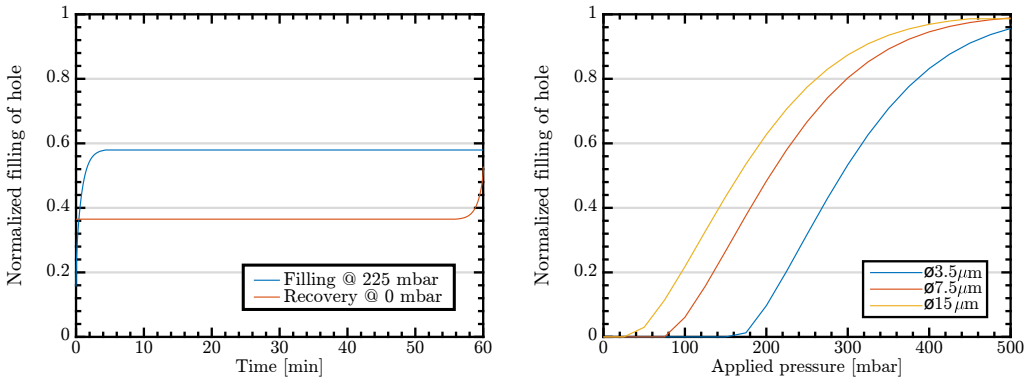

(a) Simulation with recovery **(b)** Simulation where $P_a = t \cdot 25\,\frac{\text{mbar}}{\text{min}}$

Figure 2.12: Simulation of the filling experiment with gradual pressure. In contrast to the experimental result the model shows roughly the same rate of filling for the three hole sizes.

In the paper there is also presented results of several other measurements, in figure 4b page 31 is a measurement of a recovery from the impregnating Cassie state and in figure 5 page 33 is an experiment with a time-dependent applied pressure. For both experiments, the simple simulation scheme is unable to predict the measurements accurately, see figure 2.12. In the case of the recovery experiment, the theoretical model will not make a full recovery for zero applied pressure due to contact angle hysteresis. When filling the cavity, the applied pressure needs to exceed the Laplace pressure for a contact angle on the wall equal to the advancing contact angle. After reversing the pressure, the meniscus can support a Laplace pressure with a contact angle equal to the receding contact angle. In the experiment a ø15 μm cavity is filled by applying 225 mbar pressure, the pressure in the cavity in equilibrium can be calculated using equation 2.11

$$p_g^* = p_l - \Delta p_{LP}^{max} = 225\,\text{mbar} + 2 \cdot 72\,\text{mN/m}\frac{\cos(102°)}{7.5\,\mu\text{m}} = 185\,\text{mbar}. \tag{2.18}$$

The cavity pressure is thus lower than the applied pressure due to the pressure drop across the meniscus. In the same way, when reducing the applied pressure to zero the cavity pressure will then be higher than the applied pressure. The equilibrium pressure in the cavity after the recovery cycle can also be calculated by equation 2.11 using the receding contact angle of TOPAS when calculating the Laplace pressure

$$p_g^* = p_l - \Delta p_{LP}^{max} = 0\,\text{mbar} + 2 \cdot 72\,\text{mN/m}\frac{\cos(73°)}{7.5\,\mu\text{m}} = 56\,\text{mbar}. \tag{2.19}$$

At a pressure of 56 mbar, the cavity will not be able to take up all the nitrogen dissolved in the water column during filling, since the equilibrium concentration calculated by Henry's law is higher than at the beginning of the experiment.

To explain the full recovery seen in the experimental data we have to look at what is missing from the model. The recovery experiment in the paper runs over two hours, one hour of filling and one hour of recovering. The diffusion length for nitrogen in water in on hour is

$$x_d = 2\sqrt{Dt} = 2\sqrt{1.88 \cdot 10^{-5}\,\frac{\text{cm}^2}{\text{s}} \cdot 60^2\,\text{s}} = 5.2\,\text{mm}. \tag{2.20}$$

The sample used in the experiment consists of 9 different geometries in 7 mm × 7 mm patches and with a diffusion length of 5.2 mm the concentration above one patch will be influenced by the concentration over neighboring patches. The different geometries will have different amounts nitrogen and different filling behavior and should be expected to have different nitrogen concentrations after the filling phase. If the neighboring structures are completely filled during the filling phase, they will not be able to recover in the recovering step creating a surplus of dissolved nitrogen. This excess of nitrogen could keep the concentration in the water layer above the studied structure high enough to ensure a full recovery. The influence of long-range diffusion to neighboring patches can also explain the time evolution of the filling and recovery. For the filling there is a rapid filling during the first 5 min that follow the 1D diffusion simulation very well, after 5 min the filling changes to a much slower rate indicating that diffusion over larger distances is limiting. According to the 1D model in figure 2.12a the same timescale governs the recovery process as the filling. The experimental result shows that this is clearly not the case. That the observed recovery happens at a much slower rate than the filling supports the idea of long-range diffusion to play a vital role in the recovery process.

For the experiment with gradually increasing pressure, the model results in figure 2.12b, deviates considerably from the experimental results in figure 5 page33. In the model, all

structure types fill completely at roughly the same rate after reaching the onset pressure. In the experimental results, the filling rate for the different hole sizes is significantly different. The previous analysis showed that the diffusion constant and available liquid volume governs the filling rate after the onset of filling. In the experiment, none of these parameters was changed, and there is no obvious explanation why the rates should be different. For the onset pressure, there is a slight difference between model and experiment; the theoretical calculation underestimates this pressure compared to the experimental value. The calculation of onset pressure is highly dependent on the contact angle whereas the filling profile is less dependent. It is possible that roughness on the sidewalls increases the advancing contact angle, compared to the flat reference, and that this increases the onset pressure.

3

Fabrication of microstructures in polymer

In this chapter, I will go through the different process steps in the fabrication of a microstructured polymer device. To describe such a fabrication procedure, the common practice is to write a process flow. The process flow contains all the steps from blank Silicon wafer to finished polymer part. When writing a process flow the description of each step is usually written in physical changes, e.g. an etching process should etch 10 μm deep trenches. When the processes are later developed the description changes to process parameters, e.g. etch for 10 min with 150 $\frac{cm^3}{min}$ SF_6 and 10 $\frac{cm^3}{min}$ O_2. An example of a simple process flow is illustrated in figure 3.1. By writing up a process flow, it is possible to know how to start your process to end up with the right result.

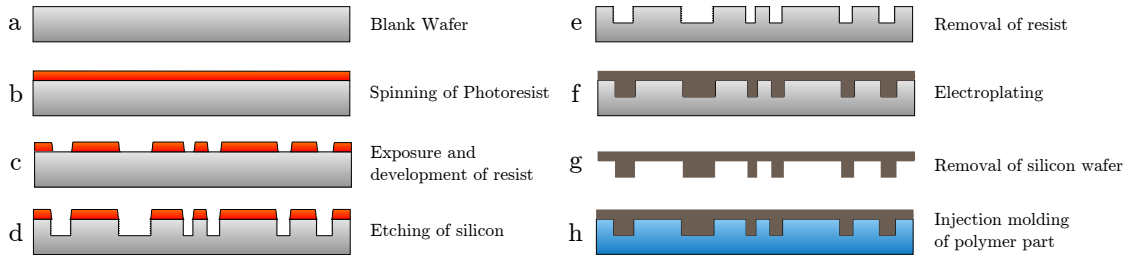

Figure 3.1: Flow diagram of simplest version of modified LIGA process.

To write up a process flow like that in figure 3.1 we can, at DTU, use the toolbox provided by DTU Danchip. This Toolbox is a compilation of standard processes on all machines, including detailed characterization of the particular process. For the simple process sketched in figure 3.1 there is no need to develop the processes yourself, you only need to modify the standard process to give the result you seek, e.g. adjusting etching times to etch the correct depth. For more complicated designs it is however often necessary to develop your custom processes to get the desired result. For such processes, it is not possible to know the exact possibilities and limitation of a given process. In this case, the process flow is a draft, and the following optimization of the fabrication might provide insights that will change the process flow. The work of optimizing processes and adjusting designs according to the possibilities and limitations is an iterative process. To minimize time and cost I often optimize processes by using "dummy" patterns before designing and ordering masks for lithography.

3.1 Design

The design phase should start with a conception of the final surface structure. The task in the design phase is to come up with a process flow describing the fabrication of the envisioned structure. From this process flow the masks required for lithography steps can be drawn in CAD software and ordered from an external mask supplier. When writing up a process flow, there are several important factors to keep in mind

- Accurately back calculate through the process steps from the desired structure to get the correct starting point
- Consider the machinery available for each step, it can be of great help to have several choices in case of long-term downtime.
- Check cross contamination ensuring that the process flow is allowed by Danchip rules, including the appropriate rinsing steps when needed.
- Consider the tolerances that can be allowed and the success rate of each step. These two factors are crucial for getting a realistic estimate of the time required to produce the final structure.

I have primarily designed the masks used in this project using the L-Edit CAD software. L-Edit is a cell-based CAD software where the deign is broken down into the simplest parts that are then repeated in huge arrays. By this approach, the files written by the software can be stored using very little hard drive space despite describing millions of structures in a single design.

For the paper included at the end of this chapter, and in some unpublished work, I have used MATLAB to write mask files that are not possible to draw in CAD software. This is done by using the human readable "Caltech Intermediate Format" .cif. The .cif format is a text file with each line describing a geometry, the basic elements being polygons and circles. A polygon defined by 5 points can be written in the file as

```
P x1 y1 x2 y2 x3 y3 x4 y4 x5 y5
```

with x1, y1 being x and y coordinate for the first point, etc. A circle is defined as

```
R d x0 y0
```

with d being the diameter, and x0,y0 being x and y coordinate for the center of the circle. All numbers are written as integers in units specified by the file header. The default value being $200\,0^{-1}\,\mu$m=0.5 nm. I have used this to write a mask with randomly placed circles and one with Penrose tiles. The script used to create the mask with random circles is included in Appendix B.

When designing a pattern, it is advised to contact the manufacturer to know the specifications of and prices for their different writing technologies. Delta mask, who is the standard supplier of masks for UV-lithography masks used at DTU Danchip, writes with a pixel size of $0.2\,\mu$m and with a minimum linewidth of $1.5\,\mu$m. For higher resolution or smaller line widths, the price for the mask will increase, rapidly. To save costs, the tolerances on the design should be compared to the specifications of the mask writer, and the mask file drawn appropriately. Without considering the manufacturing specifications it is easy to place a circle in a point that is not on a $0.2\,\mu$m grid. By not taking the manufacturing grid into account the price of the mask will increase or result in a slightly skewed circle.

3.2 Clean room fabrication

In this section I will go through the different fabrication steps I have used in the clean room. Some of the content in this section will be basic knowledge for people that have worked in a clean room. I have framed this basic knowledge to improve readability.

3.2.1 Lithography

Box 3.1: UV lithography

Lithography is the process of creating a pattern on a surface, traditionally by using a patterned master. In microelectronic fabrication, lithography is performed using a mask and a UV source to pattern a UV sensitive polymer on a wafer. There are several UV sensitive polymers available, and generally, they are divided into negative and positive resist types, the difference being the response to UV light exposure. The negative photoresist cures and becomes insoluble in a developer whereas the positive becomes soluble.[55] This is schematically drawing in figure 3.2 a.

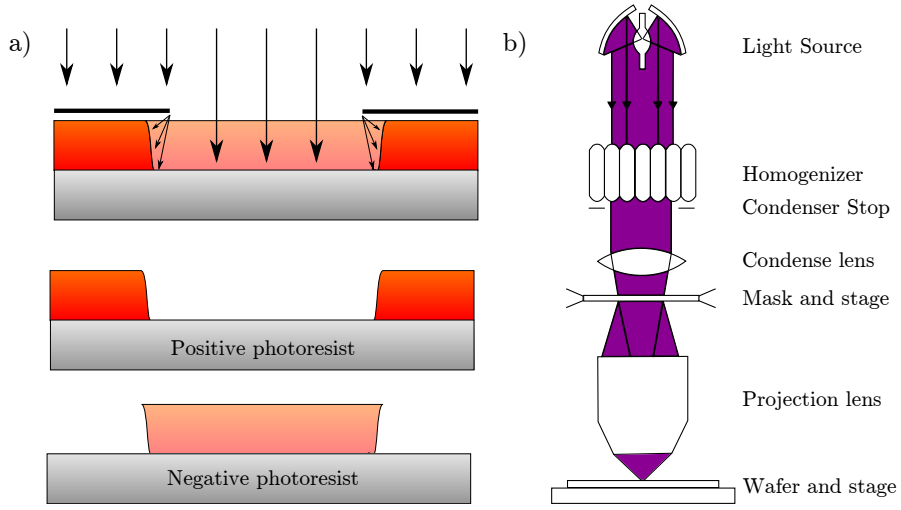

Figure 3.2: a) A schematic drawing of contact UV lithography, bending of light around edges creates a slightly sloped exposure profile in the polymer, the resulting polymer profile is depicted depending on the type of resist. b) A schematic drawing of the more advanced lens system required for projection lithography. Some of the components are also needed to get a homogeneous exposure in contact lithography. a) is inspired by[82]

At DTU Danchip there are two types of equipment available, contact lithography with a wavelength of 365 nm and projection lithography with a wavelength of 248 nm. The latter is commonly referred to as Deep UV lithography. For both contact and projection lithography, the master pattern is written on a mask by an external supplier using a laser-based mask writer. In contact lithography, the patterns of the mask are the same size as the developed pattern on the wafer. For projection lithography the pattern on the wafer is reduced in size compared to the patterns on the mask, this significantly reduces the price of producing the master pattern on the mask. For contact lithography the critical

design dimension is 1.5 μm, it can be lower but due to inhomogeneity in exposure it is challenging to get smaller feature sizes throughout the wafer. Projection lithography can by using shorter wavelength and advanced optics reliably produce features with a critical dimension of 250 nm.[83] A schematic drawing of a projection lithography system is drawn in figure 3.2 b.

In this project, I have used either UV-Lithography or Deep-UV-Lithography (DUV) for creating the patterns needed. Both UV- and DUV-Lithography are parallel patterning technologies, meaning that they expose the whole pattern in one short exposure. In contrast, serial writing techniques like laser writing, e-beam writing, 2-photon polymerization, and NanoFrazor by Swiss Litho write the patterns in series.[84] Serial writing is a maskless process that gives the possibility of resigning the pattern between every fabrication iteration. The resolution by serial writing technologies is also usually higher than that of parallel patterning. The huge drawback of serial writing techniques is however that patterns are drawn in series, i.e. the fabrication time scales with the patterned area and resolution. In this project, the aim has been to produce macroscopic areas with micro and nanopatterns suitable for mass production, favoring the patterning by parallel techniques. All UV-Lithography have been performed on an EVG620 Aligner and DUV-Lithography on a CANON FPA-3000 EX4 DUV Stepper.

When choosing between UV or DUV for a process, there has been several things to consider.

Reliability. At the start of my Ph.D. project the machine for DUV exposures was newly installed in the cleanroom. With a new installation of such a complex machine, there is expected to be a lot of downtime for maintenance, etc. Furthermore, there have been very few users to generate the required knowledge base for the proper use of the equipment. At the beginning of the project, I was therefore not inclined to use DUV Lithography unless it was necessary for realizing a particular pattern.

Time. The DUV-Lithography is handled solely by Danchip personnel, whereas for UV-Lithography the machines are operated by the individual student. The reliability on Danchip personnel can put serious time constraints of the process if deadlines for the fished samples are in holiday periods etc. The DUV machine is usually not operated for 5-6 weeks in the summer whereas the UV machinery is available 24 hours a day seven days a week all year round.

Price. Besides the cost in time for the two technologies there is a difference in cost of operation. The price for using the UV-Lithography equipment is 370 DKK/h and DUV Stepper is 3600 DKK/h. The price for ordering a standard mask for UV-Lithography is $\approx$ 1500 DKK and the price for a standard mask for DUV-Lithography is $\approx$ 15 000 DKK. The price difference rapidly decreases for batch processes, since the stepper is fully automated and can expose $\approx$ 1 wafer per minute, while manually exposing wafers in UV lithography often takes 5-10 min per wafer.

Specifications and reproducibility. The equipment for UV Lithography was developed in the early 1980s, whereas the Cannon DUV Stepper is from the late 1990s. This difference in technology age has a huge impact on the reproducibility of the two technologies. The smallest feature size produced by the DUV stepper is 250 nm whereas for UV Lithography it is around 1 μm. When aligning two patterns on each other, the stepper can do so, fully automated, with an accuracy of 50 nm with ($\approx$ 99.7 %) confidence. Aligning in UV lithography is done

manually by moving a stage until two alignment marks are on top of each other, evaluated using an optical microscope. The accuracy of such an alignment I usually not better than 3 μm.

3.2.2 Pattern transfer

To transfer the pattern from photoresist to silicon wafer there is a range of different pattern transferring techniques available. In this project, I have primarily used the SPTS Pegasus machine in the DTU Danchip clean room. The SPTS Pegasus is designed specifically for running deep reactive ion etching (DRIE) processes, but there are several other user-developed processes available on the machine.

Box 3.2: Deep Reactive Ion Etch

DRIE is a Bosch process, know from advanced silicon etching (ASE), where the process parameters change in cycles to create vertical side walls on the defined structures, see Figure 3.3a. The steps in each cycle include a passivation step and an etching step. By repeatedly combining slow anisotropic etching by ion bombardment with fast isotropic chemical etching it is possible to etch very deep trenches with vertical sidewalls. A full etching cycle is illustrated in figure 3.3b. For the process used in this project the ion bombardment in step 3 in Figure 3.3b continues throughout step 4, resulting in the semi-isotropic shape. The most important parameters when controlling the etching cycle is the gas flow, the power applied to create the plasma (coil power), the power applied to facilitate ion bombardment (platen power), the temperature of the wafer (platen temperature) and process time. The repetition of small isotropic etching cycles results in small scallops at all vertical sides, as can be seen in Figure 3.3a.

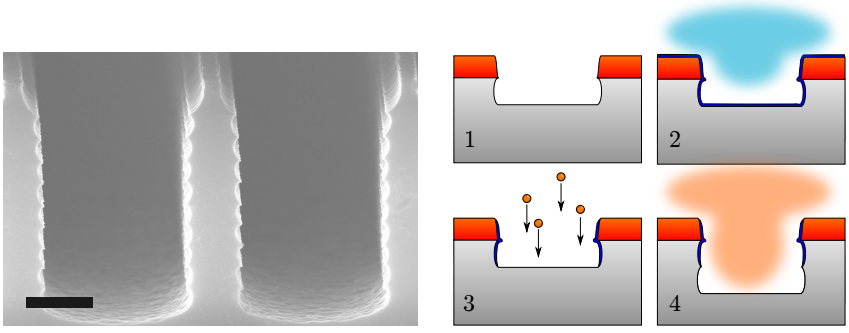

a) b)

Figure 3.3: a) SEM cross section micrograph of trenches produced by DRIE, scalebar is 1 μm. b) Drawing of the three process steps that are repeated in DRIE. 1) Showing the structure from the previous step. 2) Coverage of surface in polymer. 3) Ion bombardment of horizontal surfaces, removing the polymer from step 2 in these areas. 4) Chemical etching of all exposed silicon.

With this form of etching, the depth of the structures might vary across the surface of the wafer depending on various loading effects. Locally the etching of shallow trenches might hinder the transport of reactive ions to silicon surface reducing the etch rate. On the macroscopic scale, the etching of large areas can consume all reactive ions in the area decreasing the etch rate over a macroscopic area.

Content in this box is modified from[55]

When choosing the method for pattern transfer, the main points to consider are

Etching depth required. The etching rate for different etching technologies differ a lot, from 31 nm/min using ion milling to 20 μm/min using DRIE. At the same time the selectivity, i.e. etching rate of silicon divided by the etch rate of masking material, can be very different. The masking material is usually a thin film, not thicker than a few microns, putting strict requirements on the selectivity needed to etch a 100 μm deep trench.

Sidewall quality and shape. The different etching techniques create very different sidewalls on the etched structure. DRIE creates scallops on the sidewalls that are very close to vertical, KOH etching creates sidewall angles matching the (111) crystallographic planes in the silicon wafer, and polysilicon wet etch creates circular shaped indents.

In this project, I have primarily used DRIE since it is the best available machine to etch silicon in the micrometer range in the Danchip clean room.

Since the final structure is to be used as a mold, the sidewall quality is extremely important. Rough sidewalls would significantly increase the adhesion between polymer and mold, hindering demolding. The need for smooth sidewalls clashes with the inherent scallops of the DRIE processing.

3.2.3 Post Processing

I define post processing as the palette of processing techniques that can be used to alter or add features to the structures defined by lithography. The processes used in this project are oxide growth, oxide deposition, and reflow of photoresist. In previous projects in the group, we also used black silicon etch and isotropic silicon etch.

Oxide growth can be used to alter the shape of microstructures in silicon. When growing a thermal oxide, oxygen is introduced to the wafer in a furnace at high temperatures, typically $\geq$1000°C. At room temperature the silicon will react very slowly with oxygen in the air creating a thin native oxide, $\approx$ 1 nm thick.[85] The high temperatures of the furnace accelerate this process, enabling the formation of oxides with a thickness of up to 3 μm within a reasonable process time. This upper bound on thickness comes from the process being diffusion limited, with the oxide thickness depending on the square root of time. So although it is not impossible to grow thicker oxides it is impractical due to extremely long process time. When applying a diffusion limited process to a structured surface, the result will depend on the structure. This structural dependence is best illustrated by figure 3 on page 49 where a cleaved micropillar with thermally grown oxide is imaged in profile. At the convex corners and on the flat surface, there is the same oxide thickness, resulting in the perseverance of these structures. In the concave corner, the oxygen transport is less than for flat surfaces, resulting in the smoothening of the silicon structure. Before electroplating of the sample, the oxide is removed to expose the rounded silicon structure. This is done by etching in

hydrofluoric acid. If the oxide is not removed completely, there is likely to be overhanging structures that are not possible to mold.

Oxide deposition is the second method to reshape structures by silicon dioxide. The thermal oxide is grown, consuming silicon in the process. Oxide deposition works by just adding silicon dioxide on the surface of the sample, not changing the underlying silicon structure. The oxide deposition used in this project have been using the low pressure chemical vapor deposition (LPCVD) Tetraethyl orthosilicate (TEOS) Furnace. The deposition runs by introducing TEOS and oxygen in a furnace at 725°C and a pressure of 25 Pa. TEOS oxide have an excellent step coverage and is deposited very uniformly over the wafer, and is not limited by the diffusive transport of reactants.[86] The uniform distribution of TEOS oxide will round convex corners while keeping concave corners sharp, see figure 3.4 a-c. A drawback of the oxide deposition is the growth of defects, as shown in figure 3.4 d. During the etching of the nanopillars with positively sloped sidewalls, there is a high risk of getting small etching defects. These defects will then grow during oxide deposition. Due to the many users in the Danchip clean room, it proved extremely difficult to reliably produce wafers with a tolerable amount of defects. I, therefore, chose to abandon this deposition of oxide as a method for rounding structures.

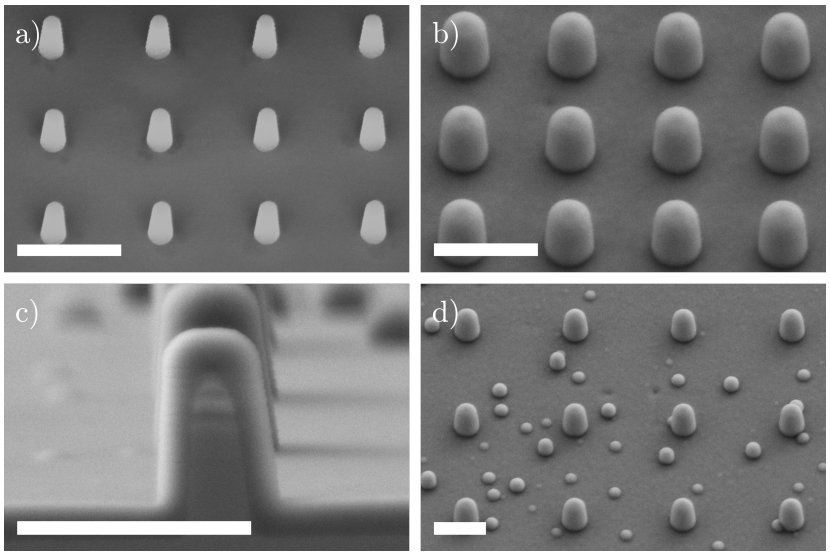

Figure 3.4: SEM micrographs of nanopillars modified by oxide deposition. a) Nanopillars in silicon directly after etching. b) Nanopillars deposited oxide. c) Profile view of a nanopillar with TEOS oxide. d) Nanopillar with oxide, showing the growth of defects from etching process. Oxide thickness is ≈ 115 nm and the scale bars are 1 μm

Reflow of photoresist can be used to create a super smooth surface using the surface tension of molten polymer. This is done by heating up the photoresist beyond its melting point, where the surface tension will shape the photoresist to minimize its surface. A cylindrical post in photoresist will in this way reflow into a spherical cap. More advanced geometries can be achieved by pinning of the photoresist and grey scale lithography.[87–89] In this project the idea of using thermal reflow was to get posts with a hemisphere on top as shown in figure 3.5 a. The reflow of photoresist into hemispheres is quite simple for photoresist on a flat substrate as seen in figure 3.5 b. To get a hemisphere on top of a pillar there is a strict relation between the volume of the photoresist and the diameter of the pillar. In order to get the right amount of photoresist on the pillar I needed to take into account the loss of

photoresist during development and etching. When doing this the resulting in very thick photoresist layers that would blur the edges of the pillars to a degree that was unacceptable. Due to the intermediate results of using reflow showing no improvements over flat-topped surfaces, I stopped the development of this process.

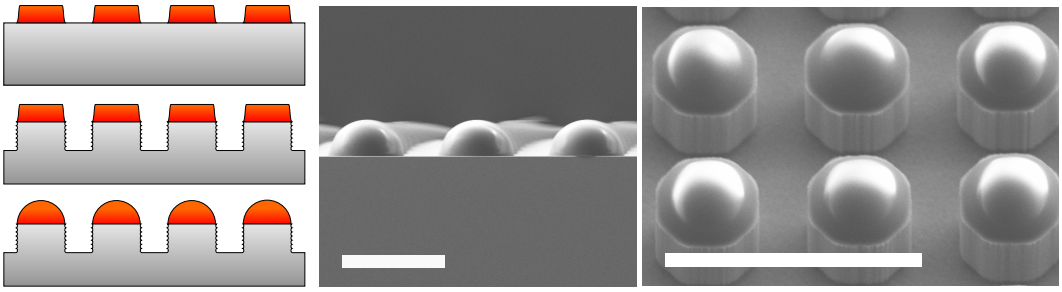

a) b) c)

Figure 3.5: a) Intended process flow using reflow to create hemispherical tops on pillars. b) hemispherical features created by reflow of photoresist on silicon. c) Photoresist on pillar tops reflown into spherical caps.

Black silicon is the product of a maskless etching process that forms nanostructures on the surface. These nanostructures are easy to recognize by their anti-reflective properties, creating a black silicon surface.[90] Black silicon has been used extensively in our group to create nanostructures of different shapes or to achieve a hierarchical structure by etching them on top of microstructures.[2,70] After extensively using this technique in my master project I abandoned it in my Ph.D. project due to three factors.

- The advancing contact angle on most polymers is too close to 90° for the drop to be in the Cassie-Baxter state on a surface with nonvertical walls, according to the conditions developed by Extrand.[19] According to Extrand, the drop cannot be in the Cassie-Baxter state if $\theta_a - \alpha < 90$,where α is the angle between the sidewall and a vertical line.
- Even in the average sidewall slope is sufficiently steep to fulfill the criterion by Extrand, the random nature of black silicon creates a distribution of sidewall slopes. The tail of this distribution will usually be below the Extrand criterion, resulting in pinning spots.
- Black silicon structures with close to vertical sidewalls often have very high aspect ratios, that are not possible to realize by injection molding.

Polarity reversal. In some cases, it is desirable to use a polarity reversal step to get the intended structure. I have developed a polarity reversal by imprinting in a polymer foil, with successive electroplating. The imprint was carried out using a $approx 100\,\mu$m thick TOPAS 5013L-10 foil in the CNI tool from NIL Technology. Using a foil instead of imprinting into photoresist enables much easier demolding since it can be peeled off. I have used this technique to reverse the polarity of; structures that have been altered by thermal oxidation, and for black silicon structures. The results from the thermally oxidized structures were published and are, enclosed at the end of this chapter.

3.2.4 Electroplating

To produce mold inserts that are hard enough to withstand the injection molding process, while not being as brittle as Silicon, I use electroplating of nickel to create mold inserts. This is a well-established technology developed by the optical disk industry (CD,DVD, Blu-ray).

Box 3.3: Electroplating

Electroplating is a process used for deposition of metals on conducting surfaces. The deposition is performed by applying a direct current through an anode and a cathode submerged in an electrolyte solution. Metal will oxidize at the anode creating metal ions, these ions will transfer charge to the cathode by deposition at the cathode surface, as illustrated with nickel electroplating in Figure 3.6 a). For electroplating of nickel the process at the anode and cathode respectively is described by

$$Ni(s) \rightarrow Ni^{2+} + 2e^- \tag{3.1}$$

$$Ni^{2+} + 2e^- \rightarrow Ni(s). \tag{3.2}$$

If the efficiency on the electrodes is 100 %, every two electrons transferred between the anode and cathode results in one Ni atom being deposited on the sample. The thickness of the electroplated layer can, therefore, be controlled by the total amount of charge running through the electrical circuit. The electroplated nickel will conform to structure on the surface where it is deposited, resulting in the inverse surface structures on the nickel part, see figure 3.6 b).

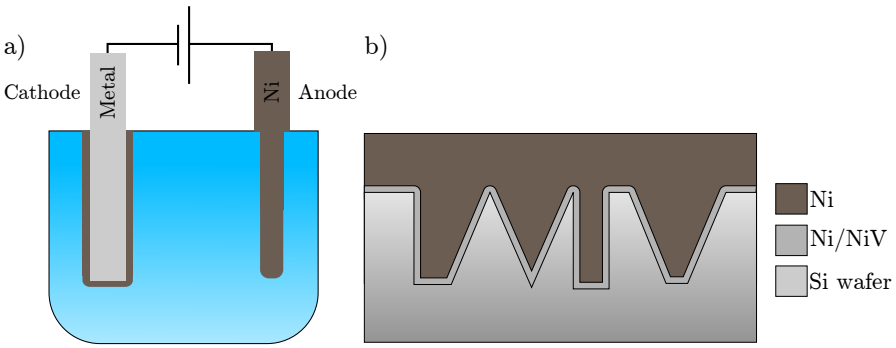

Figure 3.6: a) Schematic drawing of the electroplating process as galvanic cell running in reverse. b) Illustration of electroplated nickel on a structured surface creating the inverse surface structures.

Content in this box is modified from[55]

Before electroplating the sample needs to have a conducting surface, this is achieved by depositing a thin film of metal, typically gold or nickel vanadium. The choice of metal does not affect the electroplating process but should be taken according to the further processing of the shim. Gold does not adhere directly to silicon so before depositing gold an adhesion layer is deposited, typically titanium or chromium. When the silicon is etched away in KOH, the thin film, referred to as a seed layer, will be exposed to KOH. NiV is slowly attacked by KOH, and the etching process should be timed carefully, so the shim can be removed as soon as the last silicon is removed. Gold is not attacked by the KOH, and can thus be used in situations where there is a long time between first exposure of the seed layer and the end of the etching process, e.g. for tall microstructures. The reason for not always using gold is that the adhesion layer will be etched by KOH, this reduces the fidelity by the thickness of the adhesion layer, typically 10 nm. This loss of resolution is only problematic for the replication of nanostructures, not microstructures. Usually, the mold insert is coated with a low surface

energy coating to reduce adhesion between the molded polymer sample and shim. At DTU we use molecular vapor deposition of FDTS

I have used NiV for all shims produced in this project since I have had the best.

Due to the maturity of the technology, there have been no need to develop electroplating processes during this project. For a single design, the electroplated shim failed due to geometric constraints that were not considered. Due to the well-known increase in electric field strength around sharp corners, there will be an increased deposit of nickel at the edges. The same effect leads to dendrite formation in rechargeable batteries. In figure 3.7 a there is a SEM micrograph showing the failed electroplating of deep trenches. In figure 3.7 b I have illustrated a cross section of the trench during electroplating. The sketch shows how the increased deposition at the top corner of the trench closes the access to the bottom of the trench.

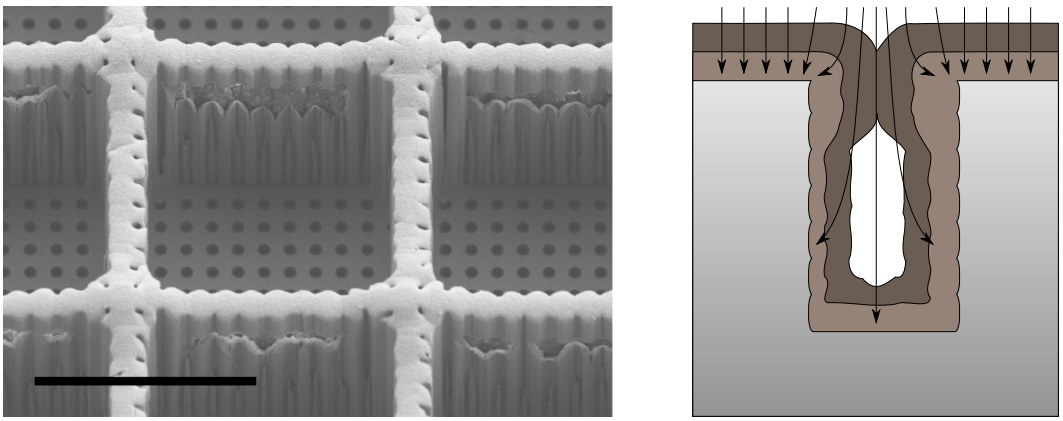

a) b)

Figure 3.7: a) SEM micrograph of holes in walls on nickel shim. Scale bar is 10 μm b) Schematic drawing of the tip effect leading to poor electroplating.

To solve the problem one could either avoid such deep trenches or use a different seed layer deposition. Sputtering of NiV has been used for seed layers in this project. The sputtering process gives excellent step coverage, ensuring that the electroplating starts at all surfaces at the same time. This is an advantage for most structures since it provides high-quality nickel on all surfaces. By using a process with inadequate step coverage, e.g. evaporation, the electroplating process could be forced to start only at the bottom of the trench. This would create poorer electroplating around the nanostructures visible at the bottom of the hole in figure 3.7 a, potentially ruining the primary purpose of the design. I chose therefore not to spend time solving this issue. Instead, I just discarded the two out 16 patches in my design where this effect gave a problem.

3.3 Injection molding

Box 3.1: Injection molding

Injection molding is an industrial process with a heated polymer injected into a closed mold where it solidifies as the temperature is decreased. After the cooling process, the mold opens and the polymer is released. The essential parts of an injection molding machine are shown in Figure 3.8. In the hopper, 1, the polymer granulate is ventilated with hot dry air. This is done to release any water possibly absorbed by the granulate during storage, as any uncontrolled water absorption could decrease the reproducibility of the injection molded samples. The barrel, 2, is a tube with a screw conveyor that transports the polymer granulate from a cold zone to a hot zone. When passing the heating zone, the polymer is molten, degassed and prepared for injection. For injection of the polymer, the screw conveyor is plunged forward and used as a hydraulic piston. This forces the polymer into the clamped mold, 3, called an injection molding tool. After injection, the part is cooled, and the clamping unit opens the tool. The tool consists of a sprue, a gate, and a mold cavity. The sprue leads the polymer from the nozzle of the barrel to the gate, connecting the sprue with the mold cavity. The thin gate is easily removed on the finished part to separate the sample from the sprue.

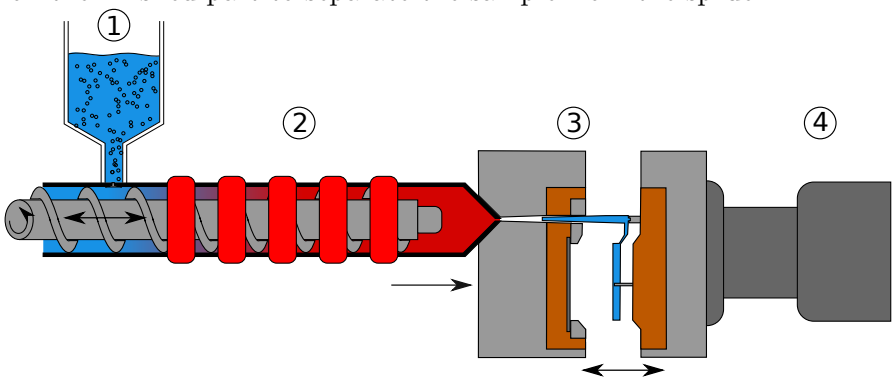

Figure 3.8: Schematic drawing of an injection molding machine. 1) A hopper that feeds the screw with polymer granulate. 2) The injection unit, it heats the polymer granulate and injects it into the mold cavity. 3) The molten polymer conforms to the geometry of the mold, solidifying into the final part. 4) Clamping system able to open and close the mold.
Content in this box is modified from[55]

The injection molding machine available at DTU Danchip is an Engel Victory 80/45 Tech, with a clamping force of 45 tons. At DTU Danchip there is three tools available, a disc tool for microfluidics, a flat disc tool, and a microscope slide tool. In each tool, it is possible to mount shims as inserts to structure one side of the polymer part. The microscope slide tool creates a rectangular cuboid part with dimensions H×B×T= 75 × 25 × 1 mm^3, the flat disk creates a 2 mm thick disk with a diameter of 50 mm, the disc for microfluidics is the same geometry as the flat disk but also provides 12 through holes with LUER connections. During my master thesis, it became evident that the microscope slide often bends during demolding, both due to the 1 mm thickness and improper positioning of ejection pins. For all samples used in my Ph.D. work, I, therefore, used the flat disc tool to mold polymer parts. A digital rendering of a piece produced by the flat disk tool is shown in figure 3.9.

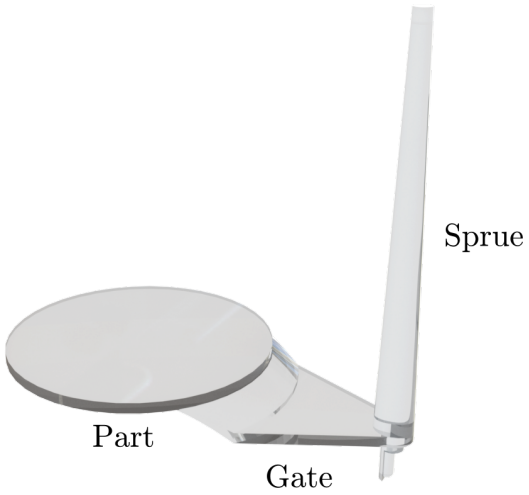

Figure 3.9: Digital rendering of the polymer piece produced by the Flat disk injection molding tool. The piece consists of a sprue, a gate, and the actual disc part.

The injection molding process is a cyclic process where the machine returns to the same state after each cycle, enabling a fully automatic process. Each cycle consists of several smaller steps that each needs to be optimized to get the molded part. For a typical industrial process, these steps are

1 Mold closing
2 Filling phase
3 Packing phase
4 Cooling phase
5 Demolding & mold opening
6 Part removal

Each step taking just a few seconds. At DTU Danchip we have the possibility of running both an isothermal process and a variothermal process. In an isothermal process, the mold is kept at a constant temperature, below the melting point of the polymer. When polymer enters a cold mold, it solidifies rapidly, resulting in very low cycle time. In an isothermal process, the mold is continuously cooled to remove the added heat from the molten polymer. In a variothermal process, the mold is heated above the melting point of the polymer before injection. After injection, the mold is the cooled below the melting point in the packing and cooling phase. Since an injection molding tool is a relatively large piece of steel, $\approx 150\,\mathrm{kg}$ for the flat disk tool, it takes some time (and energy) to heat and cool. Due to this heating and cooling time a variothermal process will have much longer cycle times than isothermal, typically $1 - 3\,\mathrm{min}$ for variothermal and $30\,\mathrm{s}$ for isothermal on the DTU Danchip Machine. For industrial processes, the cycle time is usually $< 10\,\mathrm{s}$. The heating and cooling time in a variothermal process can be reduced by optimizing the positioning of the cooling and heating elements in the mold. If the heating and cooling elements are put very close to the mold surface the amount of material that needs heating drastically reduces. More advanced methods of reducing heating time involve laser or induction heating of the mold surface just before injection.

In the flat disk tool, drawn in figure 3.10, the heating, and cooling are done in the beryllium-copper insert. This ensures reasonably fast heating and cooling. The heating is done by electrical heating and the cooling by water. This means that the heating and

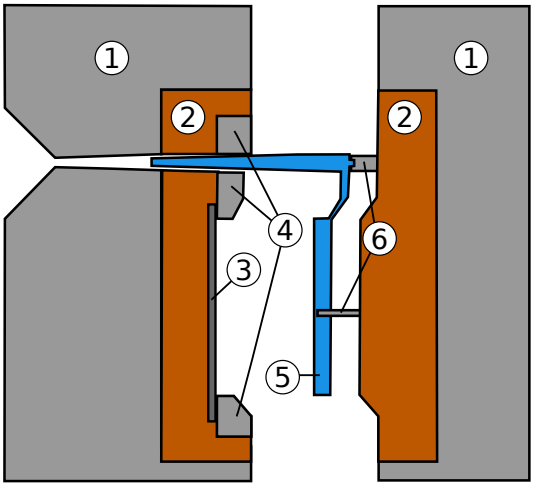

Figure 3.10: Zoom in on the injection molding tool(3) in figure 3.8. 1) Tool casing in hardened steel. 2) Berylium-Copper insert. 3) Nickel Shim. 4) Steel holding/clamping plate. 5) Finished polymer part. 6) Ejector pins

cooling comes from different places, creating an uneven temperature profile. In more advanced tooling the heating and cooling are done by (pressurized) water flowing trough the same channel, ensuring better temperature distribution. By having the heating and cooling through the same channel, it is possible to get optimum placement for both heating and cooling, something that cannot be achieved with two devices competing for space.

3.3.1 Filling phase

In the filling phase, molten polymer is injected into the cavity. The filling phase is mainly controlled by the injection volume, injection speed, and the switchover condition. The injection volume is set in the previous cycle where the polymer is loaded into the barrel. The part size, holding pressure, and polymer type are the main factors determining the amount of polymer needed. In addition to the polymer injected into the cavity, there should also be allocated some polymer as a cushion in the barrel to exert the holding pressure. There can be significant differences in the amount of polymer needed for each shot when using different types of polymer. The shot volume should, therefore, be adjusted for each type of polymer, even for the same mold.

During the filling phase, the polymer will flow into the cavity along the path of lowest resistance. The hydraulic resistance governs the resistance to flow and scales with the dimension to the fourth power. This means that the micro- and nanostructures in the mold surface does not fill before the rest of the cavity is filled. During filling of the mold, a skin layer will be formed along at the polymer-mold interface, see figure 1.5. To have a good filling of the micro- and nanostructures it is, therefore, beneficial to fill the cavity quickly so the polymer can be forced into the surface structures before solidifying. High injection speeds do, however, give rise to both burn mark formation and jetting. Burn marks arise due to gas igniting in the cavity due to very rapid compression with no time for the gas to escape. Proper venting channels in the mold can reduce this issue. Jetting happens when the polymer is forced rapidly through the gate and instead of filling the mold from on side to the other, it creates a jet. This jet produces visible defects on the part, uneven filling and can potentially damage the mold. To get the best possible filling on I follow the guideline depicted in figure 3.11.

This kind of profile has proven to give the best results, ensuring low time spent in the sprue, no jetting in the gate, and a homogeneous filling of the part. The shape of the filling curve for the filling of the part is designed to flow front with constant speed, with a circular disk as mold the parabolic shape is a good approximation. The schematic drawing is a guideline and not in exact numbers since these would vary according to the rest of the injection molding process. To find the switch between the three filling regimes, I would advise to inject at a constant speed and read the measured injection pressure. The resistance to flow will vary according to the filling, resulting in different injection pressures for different regions of the mold.

The filling phase ends when the switchover condition is met, after this point the machine follows a prescribed holding pressure curve instead of filling rate curve. Injection molding machines usually have different options, e.g. time limit, pressure limit or volume limit. Most injection molders choose either volume limit or pressure limit since these are the best indications of when a mold is filled. I would advise using the pressure dependent switch over since the pressure in the cavity is the most important state parameter. When using a pressure dependent switch over it is also easy to adjust the holding pressure to start at the same value. This ensures that the machine follows a pressure curve without discontinuities, increasing reproducibility and machine lifetime. For some machines, however, the pressure dependent switch over is very inaccurate and to get the best possible reproducibility the volume dependent switch over is adjusted to give the desired pressure.

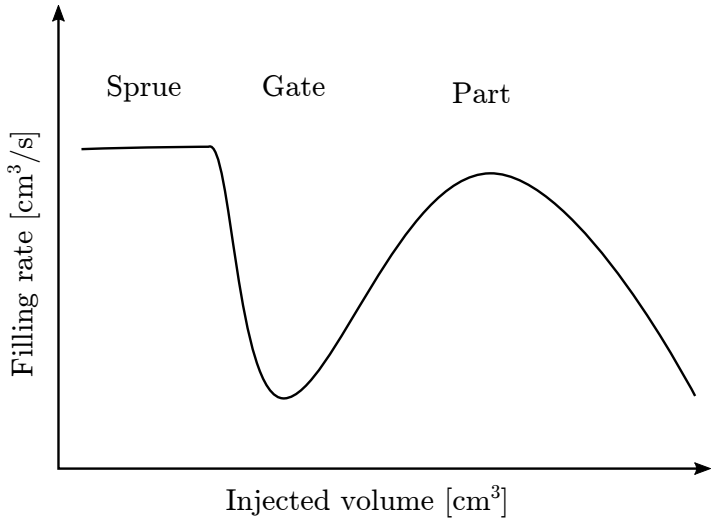

Figure 3.11: Schematic drawing of the injection profile developed for the flat disk tool. The sprue is filled at high velocity, the gate is filled very slowly, and the part is filled with parabolic profile to get a constant speed of the flow front.

3.3.2 Packing phase

The packing phase is defined by the time where the barrel exerts a holding pressure. The purpose of the holding pressure is to pack the polymer so that the finished part comes out with the right dimensions. The density of molten polymer is typically 80 % of the density of solid polymer for semi-crystalline polymers and 90 % for amorphous polymers.[91] This means that the mold needs to be filled with compressed molten polymer for the part to come out in the right size. Furthermore, the polymer should be evenly compressed to reduce internal

stresses. Stress in the solid polymer from the molding process can be very visible, resulting in warped or brittle parts. It is very difficult to obtain polymer parts with the exact shape of the mold, usually there is a shrinkage of $\leq 3\,\%$ for semi-crystalline polymers and $\leq 0.5\,\%$ for amorphous polymers. In general, it is also not possible to get an even compression of the polymer since the packing pressure is applied through the gate. This is problematic since there is a significant pressure drop over the part due to the high viscosity of the polymer.

The holding pressure can change the pressure in the part as long as there is molten polymer connecting the part and the barrel. Depending on whether the process is isothermal or variothermal this can vary from less than one second to maybe one minute. Since the gate is extremely thin it will freeze shortly after polymer stops flowing, if the temperature of the mold is lower than the melting point of the polymer, this takes 0.3 s according to Thomas Christiansen.[92] After the gate has frozen the holding pressure should be reduced, or stopped, after this point, the holding pressure will only overpack the sprue. An overpacked sprue can be very difficult to demold, resulting in the part getting stuck.

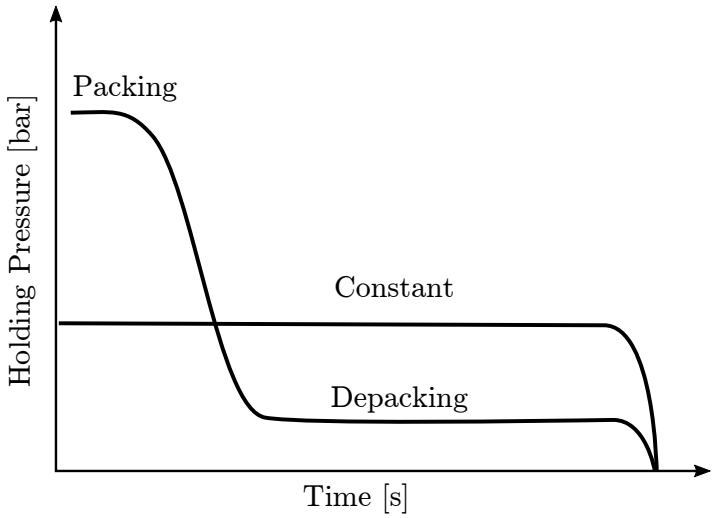

Figure 3.12: Schematic drawing of holding pressure profiles. One is constant, where it is easy to sweep over different values. The other is varying, defined by a packing pressure a transition region and a depacking pressure.

The packing profile used in this project is usually one of the two, drawn in figure 3.12. One is a simple, constant, holding pressure profile where it is manageable to sweep over a range of pressures to optimize the process. The other is more complex, with a packing phase, a transition region, and a depacking phase. For the complex holding pressure profile, the parameter space a lot bigger, optimization is therefore often done iteratively instead of by sweeping. In the iterative approach, each sample is evaluated after a change in parameters, and it is then decided whether the change was for the better or worse. The packing-depacking profile was introduced in a variothermal process by Emil Søgaard, to produce the sample in[2]. In a variothermal process, there is much more time for the polymer to flow, settle, and equilibrate. The very high packing pressure is needed to force the polymer into the microcavities but would also overpack the mold. The pressure is therefore lowered to the depacking pressure so the polymer can decompress to the desired density. Proper packing is essential both on the macro and micro scale to avoid defects, an example of bad packing on the microscopic level is shown in figure 3.13. In the figure, there is shown both a proper replicated hierarchical structure and on with defects. If it were not for the stripes on the side of the pillar and the nanostructures on top, it would look like improper filling. The

nanostructures do however reveal that the microstructure was filled but packed improperly, resulting in a massive shrinkage.

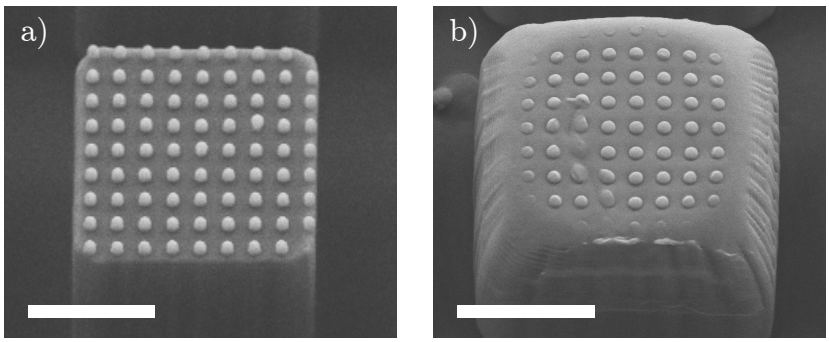

Figure 3.13: Example of injection molded hierarchical structures. a) Proper filling and packing produces perfect replication of both micro- and nanostructure. b) It is visible from the nanostructures that the microstructure was completely filled, after cooling the micro structure shrunk into the wrong shape due to improper packing. Sample a is molded in linear low-density polyethylene (LLDPE) and b in polyamide (PA), scale bar is 5 μm.

3.3.3 Cooling

The cooling phase starts when the sprue or gate have frozen. After this point the holding pressure will have no effect and the parts will only cool. For an industrial process, the guideline is to cool until the part can keep its shape, normally just below the heat deflection temperature. The heat deflection temperature is a measure of at which temperature an object deflects by a certain amount when a particular force is applied. At the heat deflection temperature the part is still reasonably hot, but now able to cool outside the mold since it will keep its shape. Removing the part as soon as it can keep its shape reduces the cycle time of the molding process, increasing production of the injection molding machine. For the borealis HD120MO PP used most frequently in this project, the heat deflection temperature is 88°C.

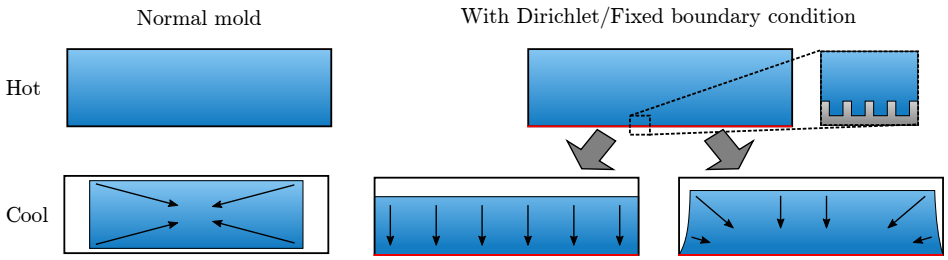

Figure 3.14: Example of part shrinkage for a normal mold, where the polymer can detach from the surface, and a microstructured mold, where it is fixed. For the fixed boundary it is not clear whether all shrinkage is in the free direction or it deforms by shrinking in multiple directions.

When injection molding micro- and nanostructures on an academic level, not caring about cycle time, the cooling time is still important. This is due to the shrinking of the polymer while cooling. For optimal molding, the part needs to be de-molded at the temperature where the shrinkage of the part is minimal. If not there will be forces acting on the microstructures

that can end up scratching the structure. It is not entirely understood how shrinkage in microstructured mold works since the microstructures fixes the polymer. I have sketched different cases of shrinking polymer parts in figure 3.14. For a regular mold, the part is ideally shrinking uniformly, keeping its shape but with reduced dimension. In the case of a microstructured boundary, the polymer will often be stuck in the microstructured surface, inducing a fixed boundary condition for the shrinkage. It is easy to imagine that the lack of horizontal shrinkage near the surface will build up stresses in the polymer. These stresses will pull the microstructures during the release from the mold. If the forces are large enough compared to the mechanical properties of the microstructures, the structure will get scratched.

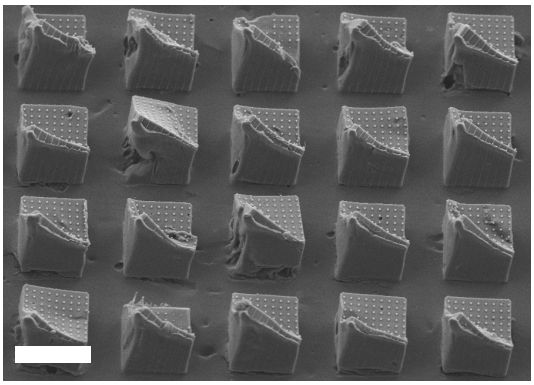

Figure 3.15: SEM micrograph of severely scratched structures. The scratch marks diminish the effect of nanostructures on top of microstructures. Sample is in PP and scale bar is 20 μm

Scratching of microstructures during demolding have been a huge challenge in this project. An example of severely scratched surface structures is shown in figure 3.15. The scratching is always, locally, in the same direction, as shown in the image. This direction changes throughout the sample, which, in turn, depends on the macroscopic shrinkage and stresses. Scratching is extremely difficult to avoid, and will in many cases, like in figure 3.15, ruin the functionality of the structure. This is due to the scratch marks altering the top of the microstructure, which is the part of the structure interacting with the liquid. It has previously been shown that the exact shape of the structure interacting with the liquid changes the wetting behaviour.[93] For injection molding of functional surfaces, scratching is a much bigger issue when creating superhydrophobic surfaces compared to e.g. an anti-reflective surface. Light interact with a nanotextured surface through an effective medium theory,[94] where liquids are much more affected by single defects.[43]

In theory, it is possible to remove the part at zero percent shrinkage, with no scratching, since the part is overpacked when molded and ends up a few percent below mold dimensions. In reality, it is not so simple because the mold is always unevenly packed with the inlet being at one side of the cavity. Emil Søgaard invented a scheme able to do this by removing the clamping force on the mold at a given moment. When removing the clamping force, the steel mold will expand by a few microns. This expansion can be used to demold microstructures smaller than this movement. The demolding by removing the clamping force was necessary since the optimal demolding time was a point where the macroscopic part was not cooled enough to keep its shape outside the mold. I have been unable to use this technique in during my Ph.D. project due to the height of microstructures being larger than the shift generated by removing the clamping force. Instead, I have found the problem to be reduced when molding in Flexirene MT 40 A. This polymer is a LLDPE which requires a high strain before plastic deformation. This enables the polymer to deform during demolding due to scratching

and then reshape into the molded shape after demolding. Using a solution that depends on the mechanical properties of the polymer is obviously only an academic fix since LLDPE is not suitable for many applications. LLDPE is currently used mainly for soft polymer bags, made by blow film extrusion.

The dynamics of cooling, shrinking, and scratching was subject for much discussion during my external stay at FHNW and the PSI. It would be possible to get a better understanding of the shrinking process by combining simulations with accurate measurements of the position and shape of microstructures on a macroscopic scale. Such an experiment have not yet been carried out. It will require strong skills within injection molding simulations and metrology, more suited for a mechanical department than a nanotechnology department.

3.3.4 Opening, Ejecting, Part Removal, and restarting

When the cooling phase ends the mold opens, when the mold is opened the ejector pins releases the sample from the mold. In the machine at DTU Danchip the ejection works by pulling the sample out, rather than pushing. This is done by having ejector pins in a slightly conical shape molten into the sample. When the mold opens, they pull out the sample from the structured cavity side, see figure 3.10. For a microstructured shim, the adhesion between shim and polymer can be very high, due to the huge interface. In such a case ejection by pulling will easily fail, leaving the sample in the mold to be removed by hand. I have found that opening the mold with extremely slow speeds ($\approx 1\,\mathrm{cm/s}$) reduces the amount of samples getting stuck. Again, this fix only works when cycle time is not important. To avoid this problem the mold should be designed with the ejector pins in a push configuration.

After ejection, the part is picked up by a robotic arm that places the sample on a conveyor belt, and the injection molding cycle can restart.

3.3.5 Injection molding at FHNW

In the paper included in Appendix E there is presented some results on injection molded samples molded at FHNW. The machine at FHNW differs slightly from the machine at DTU Danchip; having cooling and heating by water, ejector pins in a push configuration, more sensors to monitor the molding process, and ability to use compression molding. As already described, the heating and cooling by water makes the temperature distribution more even and enables optimum placement in the tooling. The ejector pins are situated around the shim insert and push from the shim side, enabling the machine to eject the samples with much higher adhesion to the shim. The extra sensors in the tool facilitate measurements of polymer pressures and temperatures several places in the cavity, this can, in turn, be used to calculate shear rates, etc. Compression molding requires a tool with a movable cavity wall. By compressing with one side of the cavity instead of using a holding pressure, it is possible to achieve a much better packing of the part. This is due to the holding pressure being applied through a tiny gate, where the compression from the cavity wall works on the whole sample.

3.4 Multi-height structures in injection molded polymer

The paper included at the end of this chapter concerns the fabrication of multi-height structures in injection molded polymer. It is included here since it is closely related to the fabrication techniques in this chapter. The design of multi-height structures was intended to give structures similar to that of the TransForm structures. The difficulty in imitating the TransForm structures by clean room fabrication is the organic shapes of the transform structures. They are rounded, of different sizes, semi-randomly distributed, and have different heights. These are all characteristics that are somewhat difficult to achieve by the planar processes available in the cleanroom. My idea to get most of these features was the fabrication scheme proposed in the paper,

- Using a mask with dots placed in random places.
- Exposing, and etching, several times to get overlapping structures.
- Smoothen the structures by growing a thermal oxide.
- Followed by polarity reversal to get pillar-like protrusions.

4

Measuring Contact angles

To quantify surfaces wetting behavior, it is of key importance to measure the contact angle of the liquid of interest, on the respective surface. This is often done in an experimental setup called a contact angle goniometer or optical tensiometer. The word goniometer comes from Greek, gōnia meaning angle and metron meaning measure. It is referred to as an optical tensiometer since it uses optical readout (images) of a drop on a surface to determine the shape of the drop that in turn can be used to derive contact angles and surface tension. Contact angles and surface tension can also be measured indirectly by force balance tensiometry where one measures the force required for pulling/pushing an object out of/into a liquid.

4.1 Force Balance Tensiometry

The setup for using force balance tensiometer consists of a mounted sample, a liquid bath, and a force meter. During the experiment, the sample is brought into contact with the liquid while measuring the force with very high precision. The force tensiometers produced by Biolin Scientific the force is measured with an accuracy down to 50nN.[95] The high sensitivity is achieved by having the sample attached to a stationary force balance and the liquid bath placed on a motorized stage. A schematic drawing of a force balance tensiometer is shown in figure 4.1a. Force balance tensiometry can be used to measure a variety of different properties ranging from

- Surface tension of liquid
- Density of liquid or solid
- Rate of liquid intrusion into porous media
- Dynamic contact angles
- Sedimentation behavior

Measuring the surface tension of a liquid, γ_{lg}, is done using a completely wetting platinum ring and can by the principle sketched in figure 4.1b be measured without knowing the density of the liquid by dividing the force measured F by wetted length $2\pi R$, $\gamma = F/2\pi R$. This particular use of a force tensiometer is known as the Du Noüy ring method. Densities of liquids and solids can be measured by submerging an unknown solid in an know liquid or submerging a known solid into an unknown liquid and in either case, measure the buoyancy force. Knowing the volume of the solid the density calculation is trivial. Dynamic contact angles can be measured by lowering a solid with known density into a liquid with known density and surface tension. The object should have a geometry so that the triple line is moving on vertical surfaces only. When this is the case the force per length on the object is $F = \gamma l \cos(\theta)$ where θ is the contact angle. By determining the wetted length, l, from the geometry of the solid, the contact angle can be calculated. By measuring the force through

a whole cycle of lowering the object (advancing triple line) and raising it out (receding triple line) of the liquid, it is possible to measure both advancing and receding contact angle. Dynamic contact angles measured in this way are an average of the wetting properties along the triple line. The averaging mechanism in the measurement process produces very accurate results for homogeneous samples but is unable to measure local variations in the wetting properties. The drawback of not being able to measure local contact angles is the reason why we have not used a force tensiometer for measurements presented in this thesis.

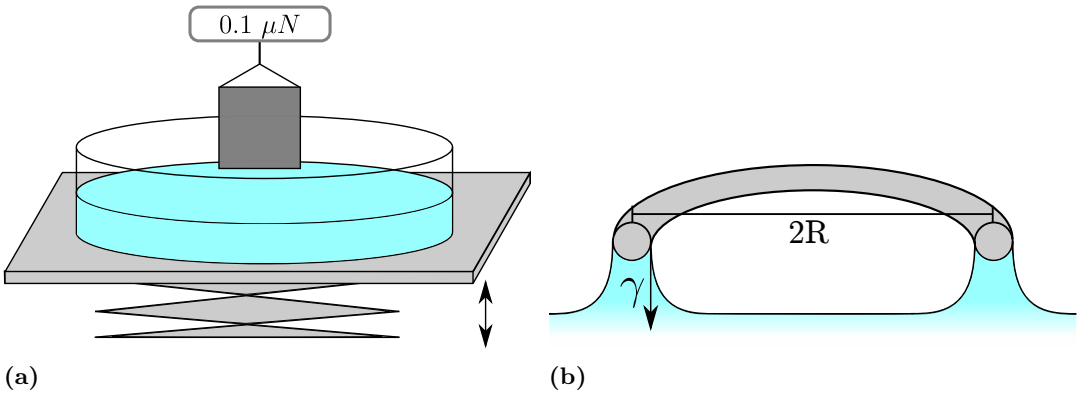

Figure 4.1: (a) Setup of a force tensiometer, it consists of a liquid bath on a moving stage and an probe attached to a force meter. (b) Sketch of the physical principle when using a ring probe, the surface tension pulls at the ring with a force per length. Knowing the total force and geometry of the ring the surface tension can be calculated.

4.2 Optical Tensiometry

The simplest optical tensiometer setup consists of a camera, with an appropriate lens system, a sample stage, and a motor controlled syringe. The principle of optical tensiometry is to bring a drop into the field of view of the camera and measure the desired properties by analyzing the drop shape recorded by the camera. Optical tensiometry cannot measure as many physical properties as force tensiometry, but it is possible to measure a few properties in a variety of situations that cannot be achieved in force tensiometry. This includes

- Surface tension of liquid with known density
- Local static contact angle
- Local dynamic contact angle
- Contact angle distortion from electrowetting phenomena
- Contact angles of a drop impacting the surface
- Contact angles on tilted surface

These different situations require different extra pieces of equipment to the basic optical tensiometer setup. For measuring electrowetting phenomena, the electric potential around drop should be controlled; for measuring drops impacting a surface, the camera should be able to record at high frame rates and for measuring on drops on tilted surface, the sample stage should be able to tilt. The measurement of dynamic contact angles between a liquid and a solid is often done with the purpose of predicting the behavior of solid-liquid interaction in some particular physical situation. For this, the versatility the optical tensiometer offers can

be used to measure the dynamic contact angles in a situation that resembles and thereby giving results that are more accurate. For instance, if one wants to make a superhydrophobic window that repels raindrops it is important to measure on impacting drops. It could be that the Cassie-Baxter state of the surface is very unstable, and the surface only appears superhydrophobic when measured with drops that are very carefully placed, whereas impacting drops pins. For measuring dynamic contact angles of drops on a surface, there are at least two different approaches, the sessile drop method, and the tilting method.

4.2.1 Sessile Drop method

With the sessile drop method, a drop is placed on the surface without removing the needle that dispensed the drop. The drop is then inflated by adding liquid to the drop. Continuous inflation of the drop will force the triple line to advance over the surface, and the advancing contact angle is measured. The liquid is then extracted from the drop to force the triple line to recede, and the receding contact angle is measured. This procedure is sketched in figure 4.2a. Inflation and deflation of the drop should be done at relatively slow speeds so inertial effects can be neglected and the drop is in quasi-equilibrium. It is important to note that the drop exhibits the advancing contact throughout the inflation, whereas the correct receding angle is only seen a single time during deflation. The difference between advancing and receding measurement is that while the triple line advances there is always a dry surface on one side of the triple line and a wetted surface on the other. During receding this is only the case when the triple line starts moving, after that, the surface just outside the drop has very recently been wet. The recently wet surface can be different from a dry surface; either from chemical changes in the solid surface, like molecular reorganization, or liquid molecules adsorbed at or absorbed by the surface. This is clearly seen in figure 4.2b where the water contact angle on microstructured polystyrene is plotted as a function of the base radius of the drop during a dynamic contact angle experiment. In the inflation phase, the contact angle is stable $\approx 112°$ being the advancing contact angle. At the beginning of the deflation phase the contact angle decreases with a pinned triple, at $\approx 78°$ being the receding contact angle the triple line starts moving but the contact angle does not retain a unique contact angle during triple line movement. Since polystyrene does not absorb water, it is unlikely that this is the cause of the contact angle decreasing below the receding contact angle. More likely is the migration of additives, molecular reorientation or molecular adsorption of water on the surface. If the experiment was conducted over a longer timescale the resting time effects shown by Tadmor[62] would change the measured dynamic contact angles due to molecular reorganization at the triple line.

4.2.2 Tilting Method

In the tilting method, a sessile drop is dispensed at the surface; the surface is then tilted until the drop rolls or slide off the surface. The advancing and receding contact angles are then taken as the contact angle on the advancing and receding side of the drop at the point where the drop starts moving down the inclined surface. The angle of inclination required for the drop to start moving is also referred to as the roll-off angle. The roll-off angle should not be considered as a material property as the dynamic contact angles since it depends on the size of the drop used in the experiment. The gravitational force on the drop scales with the volume of the drop whereas the retention force on the drop according to the Furmidge equation[96] scales with the radius of the drop. The comparison of roll-off angles measured with drops

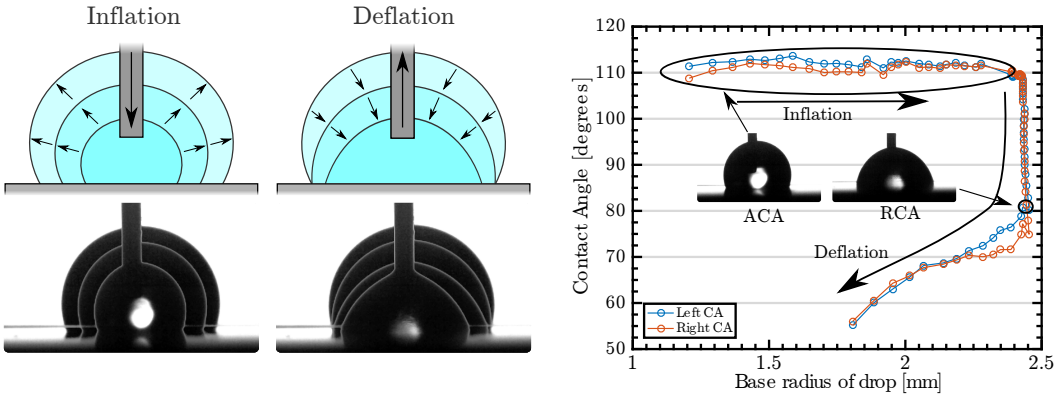

(a) **(b)**

Figure 4.2: (a) Schematic drawing of a dynamic contact angle measurement together with stacked images of an actual recording. (b) Measured water contact angle on micro structured polystyrene as a function of base radius of drop. During inflation the drop have the advancing contact angle at all times but when deflated only exhibits the receding contact angle at one point i time.

of the same size does, however, give key information about the water repellency that can be compared between different surfaces. Due to the difficulties in accurately determining the contact angle for superhydrophobic surfaces it has been proposed to use the water shedding angle to evaluate the performance of superhydrophobic cloth. The water shedding angle is the angle that a sample should be tilted before an impacting drop leaves the surface, it is closely related to the roll-off angle. In most setups, the camera recording the experiment is mounted in a way, so it follows the solid surface during the tilting experiment, in this way it is easy to determine the onset of drop movement.

4.3 Fitting methods

For all optical tensiometry methods, the output is a sequence of images of the drop in profile. To determine the contact angle, the image needs to be processed. The processing of images usually involves

1 Determination of drop boundary.
2 Find baseline of drop by using the reflection.
3 Fit a selection of the boundary to an equation.
4 Evaluate the slope of the equation at the baseline and calculate contact angle.

In each step, there are different choices to be made depending on the experimental setup.

Step 1 There is a range of different edge detectors to choose from; Sobel, Kirsh, Prewitt and Canny being the those implemented in matlab.[97] These edge detectors are all limited to pixel resolution whereas more sophisticated methods detects edges with sub-pixel accuracy.[98,99] Chini and Amirfazli claim that the accuracy on the determined contact angles increases by achieving by sub-pixel resolution.[100]

Step 2 Many algorithms for measuring contact angles rely on the user to determine the baseline[101], whereas some are fully automated. It has been shown that the determination of

the baseline is critical since a placement error of 1 pixel, invisible to the naked eye, can result in several degrees difference in determined contact angle.[102] I therefore strongly recommend that baseline determination should be fully automated to reduce operator induced errors. If it is not possible to automatically determine the contact angle in the software available it is possible to use magnification tools to help triple line placement. In figure 4.3 there a screen capture from the Attension Theta software with baseline placement and inserts of zoom on the left and right triple line. It is evident from the images that manual placement is no straightforward task. The left side looks by far the best for the center image but for the right side, it is not clear if the left or center image is the best. The difference between left and right suggests that the tilting angle of the baseline is not correct, but determining angles with 0.1° accuracy by eye is really difficult. Automated schemes for determining the baseline often involves a rough determination using pixels on the boundary; that is then refined by finding the intersection of linear extrapolations of the drop shape above and below the rough baseline.[100,103] It is relatively simple to automate the determination of baseline for drops with low or high contact angles since the point of reflection is very clear, it is much more difficult for drops with a contact angle close to 90°. A drop with a contact angle on 90° forms a hemisphere that with its reflection looks like a sphere. Such an image could also come from a drop with a contact angle of 180°, the difference being that drop with $\theta = 180°$ would have a reflection whereas the drop of $\theta = 90°$ would end in some shadow. Following this line, all drops with a contact angle above 90° could be mistaken for a drop with 90° with a baseline at the widest part of the drop. An automated baseline algorithm should be able to distinguish between these two cases.

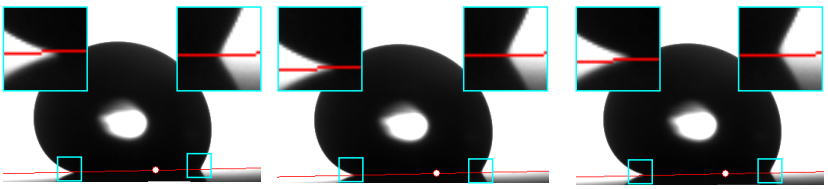

Figure 4.3: Several guesses at manual baseline placement in Attension Theta software. My best guess is in the center with image to the left and right have the baseline shifted 1 pixel up and down, respectively. It is also possible to tilt baseline with 0.1° resolution.

Step 3 Involves two related choices, the selection of drop boundary and an equation to fit it. The equation should be a reasonably good approximation of the drop boundary; this is usually achieved by either using an equation derived from the physical properties or an equation with enough degrees of freedom. The typical equation based on physical properties is a parameterized derivation of the Young-Laplace equation including hydrostatic pressure, where it is assumed that the drop is axisymmetric around a vertical axis.[103,104] This equation is an exact description of the drop shape of a drop on a horizontal surface with the same contact angle at all sides. Fitting to the axisymmetric Young-Laplace equation is often referred to as axisymmetric drop shape analysis (ADSA). Since it is an exact description of the whole drop shape, it is possible to fit all points describing the boundary to the equation. This ensures that whenever applicable ADSA provides the most precise and accurate results possible. In the case that the axisymmetric Young-Laplace equation cannot describe the drop there is a need for a different equation. This need arises when fitting tilted drops, drops in motion or drops influenced by electric fields. In these cases, there is rarely an equation that describes the exact shape of the drop and approximations are used instead. These approximations are generic equations such as polynomial[105] or spline[101] functions. When using an approximation, it is important to determine the length of drop contour that can be

accurately described by the approximation, if not the fitted result will be very inaccurate. This a result of the fitting algorithm that minimizes the error for all data points whereas the slope at a single point determines the contact angle.

Step 4 Once the drop contour is fitted, and the baseline is determined it is straight forward to obtain the contact angle from the slope of the fitting function at the baseline.

There is a few examples where step 2 is omitted by fitting to the greyscale data in the image directly to the function using different approaches.[101,106] This requires more elaborate algorithms but could, in turn, give more accurate results by not throwing away information stored in the greyscale values.

4.4 Development of new fitting method

For this project, all contact angles have been measured on our Attension Theta machine equipped with a tilting stage and a high-speed camera.[107] In the commercial software that comes with the equipment, it is possible to fit contact angles by Young-Laplace, Circle or polynomials. Fitting to the Young-Laplace equation also provides information about contact points, volume and surface tension, while the other methods only provide the contact angle. It is with this extra information from the Young-Laplace method that the plot in figure 4.2b is generated. During a tilting experiment where only the polynomial fitting is available, it is not possible to get the data to plot a relation between contact angle and displacement. Such a plot would make the determining the onset of movement much more accurate, compared to scrolling through frames one by one and deciding when the movement starts. By developing an in-house program, it would be possible to get the extra information needed and avoid the black box that commercial software is. For a time this was not enough reason to embark on such a project.

In the data treatment of the structures presented in chapter5 it was crucial to get better control of the contact angle fitting. The main challenge for the commercial software are the optical distortions often seen close to the receding triple line. An example of a severe distortion is seen in figure 4.4 where the light transmissions through the drop create white areas around the receding triple line. In this case, the polynomial fit does clearly not fit the correct contact angle. To get more accurate results for the contact angle of tilted drops, I developed a new fitting algorithm described in a submitted paper attached at the end of this chapter. This algorithm uses double elliptic fit to use all data points on the drop perimeter instead of the small arc that can be used in polynomial fitting. In this way, it was possible to obtain the correct contact angles and triple line position of a measurement series as plotted in figure 4 page 63.

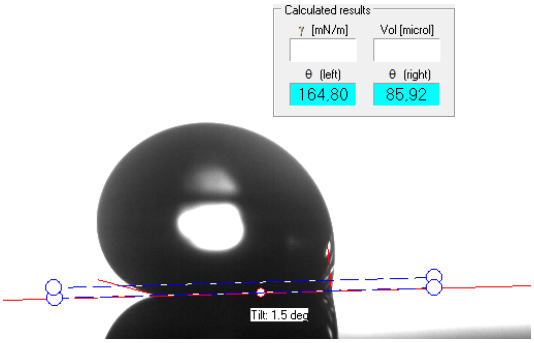
Calculated results
γ [mN/m]
Vol [microl]
θ (left)
θ (right)
164.80
85.92
Tilt: 1.5 deg

Figure 4.4

5

Surface Structures and Contact Angles

The surface structures giving rise to the superhydrophobic Cassie-Baxter state are often referred to as roughness.[75,108,109] This phrase might, however, be misleading since the particular shape of the surface structures is crucial for upholding the Cassie-Baxter state. It therefore not enough to have high roughness factors or low solid-liquid contact area, since these parameters do not describe the specific structure on the surface. The specific conditions at the triple lines have shown crucial to determine the wetting behavior of a given surface structure, both regarding the stability of the Cassie-Baxter state and depinning process allowing a drop to roll off the surface.

A significant part of this project have been concerned with getting an understanding of the governing mechanics resulting in a water repellent surface. This more fundamental research have been necessary to enable the proper design of surface structures that are suited for injection molding and produces a water repellent surface. This need for better design arose from the fact that water repellent structures demonstrated in literature were badly suited for injection molding. During this fundamental research, the focus was centered around uncovering the properties of the TransForm structures, with its superior water repellency and shapes suited for injection molding.

5.1 Irregular structures

During the project, I have gained several insights for the design of water repellent surface structures suited for injection molding. At the beginning of the project Emil Søgaard, a former Ph.D. in the group had worked with producing structures able to support the Cassie-Baxter state when submerged under water. In this work, it was evident that hole like structures was superior due to the enclosed gas volume, separated triple lines, and capable of being injection molded.[2] The hole-like structures are better suited for injection molding compared to pillar-like structures due to the decrease in hydraulic resistance, reducing the pressure needed for filling. Due to these immediate advantages of hole-like structures and inspiration from the irregular TransForm structures, we embarked upon the study of irregular hole-like structures.

The anticipated benefit of using irregular structures was to reduce the maximum number of structures that a drop needs to detach simultaneously, before rolling off the surface. To produce irregular structures I worked for some time designing structures by using Penrose tiles. Penrose tiles are generated by a special kind of tiling system developed by Roger

Penrose. This tiling system can non-periodically tile an infinite plane using two prototiles. There is a range of different tile combinations that can be used to produce a Penrose tile, in this project I worked with the rhombus tiling system. Penrose tiles were an appealing structure type due to

- Being irregular structures created in a deterministic way, with no random numbers needed.
- Having well-defined sizes since the pattern consists of two prototiles.
- Being similar in all directions.

I ended up not using Penrose tiles for structuring surfaces since it was not clear whether this would give any insight into the direct effect of irregularity. Instead, Simon Tylsgaard produced samples with hole-like structures with increasing irregularity. This was done by creating walls connecting dots placed in a square grid. To induce irregularity, the dots was randomly moved away from their position in the square lattice and the irregularity was increased by spreading the probability distribution used to re-position the dots the. The produced structures were not injection molded but instead characterized directly in silicon. This was done to avoid molding defects from influencing the wetting behavior of the surface.

To our initial surprise, the increased irregularity did not decrease resistance to water movement. Instead, it increased. We found that the increased adhesion to the surface originated from the increased contact line density due to the irregular wall being longer, on average. The fact that line density drastically increases adhesion is a major drawback of hole-like structures. Hole-like structures with low surface coverage need to consist of very thin walls which have an enormous line density, compared to pillar-like structures of the same surface coverage. This difference in line density and its impact on wetting performance have convinced me not to use hole-like structures for creating water repellent surfaces. Despite that hole-like structures are easier to realize by injection molding. That the increased line density is the cause of increased adhesion, we explained by constructing a simple model with the drop rigid-body, applying a torque to the triple line when the sample is tilted. This torque must be compensated by the adhesion to the underlying microstructure if the drop is not moving. The result of this work is the paper included at the end of this chapter.

5.2 Hierarchical Transition

After turning the focus to pillar-like structures, I searched in literature for interesting structure types that would be suited for injection molding. As mentioned in the introduction the majority of demonstrated water repellent surfaces uses hierarchical structures to generate the extraordinary wetting properties. Since hierarchical structures are not very suited for injection molding, I found it important to study the underlying reason for the superior performance of these structures.

Hierarchical surfaces are often deemed superior, due to two factors. First, the low surface coverage resulting from the product of the surface coverages of the individual micro and nano levels.[110] Secondly, the nanostructures on the sidewalls of micropillars increase the Laplace pressure needed for collapse of the Cassie-Baxter state by the depinning mechanism.[111] Extremely low surface coverages are also possible to achieve by single level structures. The first argument for the low surface coverage can, therefore, not stand by itself. The immediate explanation is that by creating a single level structure with extremely low surface coverage, the stability of the Casie-Baxter state is drastically reduced. Experimentally this is shown by

Bhushan[111] where increasing the pitch of a given microstructure will for large pitches result drops collapsing from the Cassie-Baxter state to the Wenzel state.

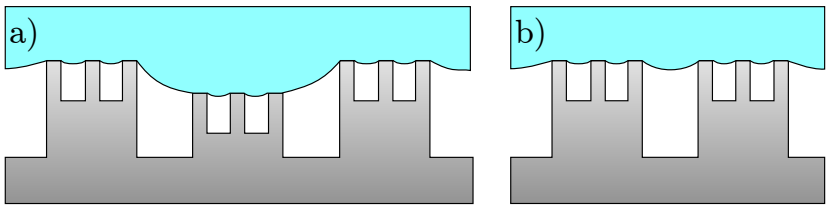

Figure 5.1: Drawing of different geometries for simulation of the menisci. a) Has features at different levels and the 3d capabilities of surface evolver makes it the best suited software for such a simulation. b) All features are at the same level, enabling 2d simulation in COMSOL.

5.2.1 Simulations

The stability of the Cassie-Baxter state can be evaluated using simulations of the shape of the meniscus between pillars. For an arbitrary geometry such a calculation could be carried out in 3D using surface evolver.[112] For a simple geometry where the top of microstructures all are in the same plane, the simulation can be simplified to a 2D model. The difference in structures suited for 3D and 2D are illustrated in figure 5.1. For the simple structure, the bending of the meniscus can be simulated in 2D by rearranging the Young-Laplace equation.[113,114] In its rearranged form the curvature of the meniscus is calculated from a function $f(x, y)$ describing the deflection of the menisci at point (x, y). By using the 2D Young-Laplace equation, I have simulated the bending of the meniscus of a drop resting on top of a hierarchical structure in various configurations. The result of four of these simulations is plotted in figure 5.2.

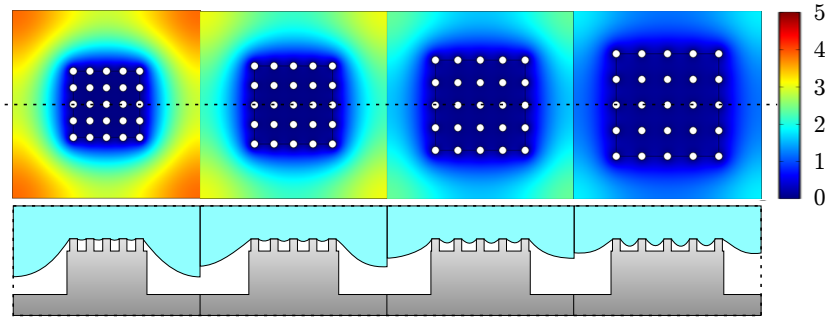

Figure 5.2: Simulation of bending of meniscus for different arrangements of pillars in a grid, the scale is in arbitrary units. Below each simulation is a drawing of the cross-section of the simulated structure. Denser spacing of the top level geometry decreases the deflection between these structures but increases the deflection between the bottom level structure. The drawn deflections in the illustrations are grossly exaggerated to illustrate the point.

The simulations presented in figure 5.2 show that different surface structures with the same solid-liquid interface can have very different wetting situations. At first, it seems like the structure with the widest spacing of top level structures has the lowest probability of collapsing into the Wenzel state by a sagging transition, due to the overall lower bending of the meniscus. The absolute bending presented in the surface plots should, however, be compared with much smaller structure height of the top level structure. Instead of evaluating the absolute deflection, we should instead evaluate the deflection between structures relative to

the height of these structures. If we assume that the structures at both levels can be produced with an aspect ratio of 1, we should divide the deflection between structures with the width of the respective structure. This I have done for a range of simulations similar to those presented in figure 5.2, where the distribution of top-level structures has been parameterized by the spacing parameter α. This is implemented such that α defines the spacing of the upper-level structure, where $\alpha = 0$ corresponds to having a spacing of 0, and $\alpha = 1$ corresponds to having an equal spacing throughout the unit cell. In this way, the α value describes a transition between single level structures and hierarchical structures. $\alpha = 0$ corresponds to being only microstructures, $\alpha = 1$ being only nanostructures, and $0 < \alpha < 1$ being hierarchical structures of different configurations. The structures in figure 5.2 have, from left to right, α values of $\alpha = 0.4$, $\alpha = 0.5$, $\alpha = 0.6$ and $\alpha = 0.7$. The result of simulations with $n^2 = 9 \times 9$ upper-level structures in a square grid on each lower level structure and a solid-liquid area fraction of $f = 2\,\%$ is shown in figure 5.3.

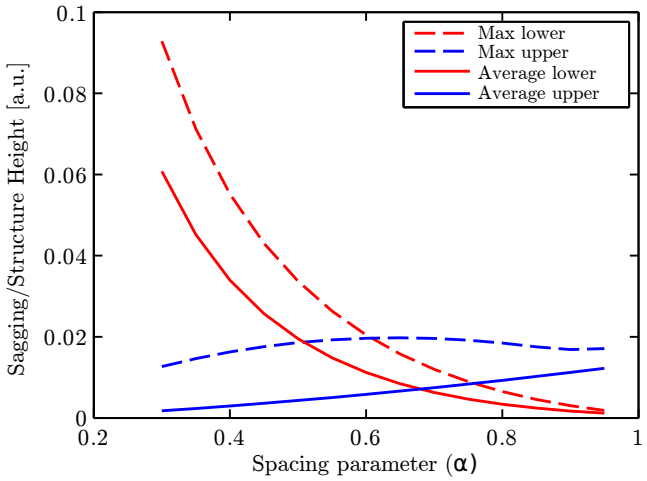

Figure 5.3: The deflection between the upper and lower structure evaluated relative to the respective structure height. The maximum deflection is found as the maximum of $f(x, y)$ between the respective structure, whereas the average deflection is the average of $f(x, y)$ in the same region.

From figure 5.3 it is evident that the relative deflection between the lower level structures is much bigger than the deflection between the upper-level structures. This result is consistent with a calculation of the deflection between two line structures. Between two lines the deflection can be calculated using relations for a circular segment,

$$d = r - \sqrt{r^2 - \frac{c^2}{4}}, \tag{5.1}$$

where d is the deflection, r is the radius of curvature, and c is the distance between structures. The radius of curvature is constant when comparing different structure sizes since it is determined by the macroscopic drop size. When $c << r$, which is the case for a millimeter-sized drop and micro- or nanostructure, the Taylor expansion to first order of equation 5.1 gives

$$d \approx= \frac{1}{8}\frac{c^2}{4r^2}. \tag{5.2}$$

Since the d scales with c^2 and the height of the structure scales linearly with c, the relative deflection scales linearly with c. This scaling relation suggests a general advantage using

nanostructures instead of microstructures for keeping a drop in the Cassie-Baxter state. Using nanostructures generates a much larger resistance to the sagging wetting transition.

5.2.2 Design

The data plotted in figure 5.3 suggests that there is an optimum configuration of the structures where the stability is evenly divided between the upper and lower level structures. For the specific geometry with $f = 2\%$ and $n^2 = 9 \times 9$ the optimum α value is between $\alpha = 0.61$ and $\alpha = 0.68$ depending on whether the maximum or the average deflection is used. The particular α_0 value for the optimum configuration depends on the surface coverage and the amount of upper-level structures on each lower-level structure. An increase in either n or f will increase the value of α_0.

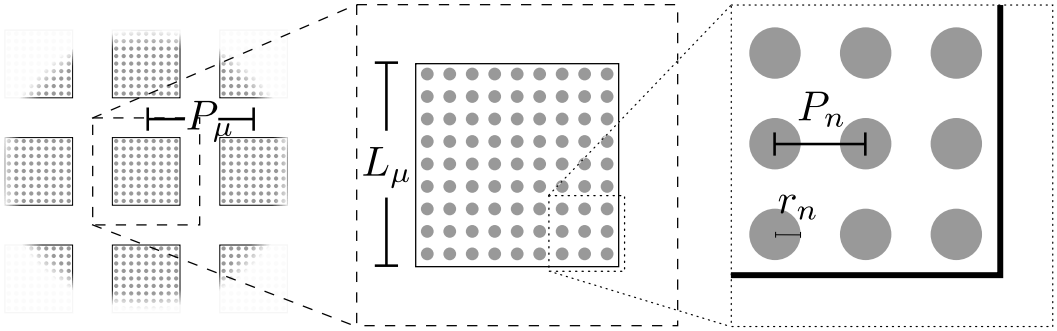

Figure 5.4: Schematic drawing of the geometric paramters describing a hierarchical structure. All geometric paramters can be calculated from the surface coverage f, spacing parameter α, and one on of the 4 parameters in the figure.

To experimentally test this hypothesis of an optimum configuration of a hierarchical structure I designed a set of structures with α values ranging from $\alpha = 0.2$ to $\alpha = 0.7$. All structures have $n^2 = 9 \times 9$ ø300 nm circular nanopillars on top of each square micropillar. I designed 8 spaces with a surface coverage $f = 2\%$ and 8 spaces with $f = 8\%$. Using these design parameters it is possible to calculate the rest of the geometric parameters needed to fully describe the surface by:

$$P_\mu = \sqrt{\frac{n^2 \pi r_n^2}{f}} \quad , \quad P_n = \left(\frac{P_\mu}{n} - 2r_n \right) \alpha + 2r_n \quad , \quad L_\mu = 9P_n, \tag{5.3}$$

where L_μ is the side length of the square microstructures, r_n is the radius of the nanopillar, and P_μ and P_n are the pitches of micro- and nanostructures, respectively. A visual representation of the geometric parameters is shown in figure 5.4. The choice of using $r = 150$ nm to set the length scale of the system was based on the choices in the fabrication process. During the fabrication process, the exposure, and etching of the nanopillars is much more delicate than that of the micropillars. For the optimization of fabrication processes, it is, therefore, beneficial if all nanopillars are of the same dimensions. The calculated geometric parameters for the 16 spaces is tabulated in table 5.1.

In table 5.1 there I have also calculated the surface fraction of the nano, the micro and the combined hierarchical level of structure with subscript n, μ ,and h, respectively. Φ_i in the table is the calculated pinned fractions calculated by to the equations presented by Paxson.[33] The pinned fraction is a measure of the total triple line length at the drop perimeter on a

structured surface relative to that of a flat surface. It can for each level be calculated as

$$\Phi_i = \frac{O_i}{P_i}, \tag{5.4}$$

where P_i is the pitch and O_i is the circumference of the structures at the specific level. The total pinned fraction is found by multiplying the pinned fraction for all structure levels, i.e. $\Phi_h = \Phi_\mu \Phi_n$. According to Paxson the force required to lift a drop from a structured surface, compared with that required on a flat surface, scales with the total pinned fraction Φ_h. The $2x8$ structures are therefore remarkable since they show the same surface coverage and pinned line fraction, despite being very different. This is achieved by using lithographic processes for creating both levels of structures, in contrast to most hierarchical structures. For most hierarchical structures demonstrated in literature the microstructure is designed by lithography or micromachining and the overlaying nanostructures are produced by self-assembly or maskless processes.[14,38,110,115–118]

5.2.3 Fabrication

The process flow for fabricating the designed structures in silicon is

1 Spinning of 100 nm bottom anti reflection coating (BARC) and 360 nm KRF M230Y, a possitive DUV resist.
2 Exposure of nanopillars on DUV stepper.
3 Etching of nanopillars using a continuous etching process (nano 1.42).
4 Spinning of 100 nm BARC and 1000 nm of KRF M35G, a possitive DUV resist.

Space nr.	α	P_μ $[\mu m]$	L_μ $[\mu m]$	P_n $[\mu m]$	f_n %	f_μ %	f_h %	Φ_n	Φ_μ	Φ_h
1	0.2	16.92	5.544	0.616	10.7	18.6	2.0	1.53	1.31	2.01
2	0.3	16.92	6.966	0.774	16.9	11.8	2.0	1.22	1.65	2.01
3	0.4	16.92	8.388	0.932	24.6	8.1	2.0	1.01	1.98	2.01
4	0.45	16.92	9.098	1.010	28.9	6.9	2.0	0.93	2.15	2.01
5	0.5	16.92	9.810	1.090	33.6	5.9	2.0	0.86	2.32	2.01
6	0.55	16.92	10.520	1.168	38.7	5.2	2.0	0.81	2.49	2.01
7	0.6	16.92	11.232	1.248	44.1	4.5	2.0	0.76	2.66	2.01
8	0.7	16.92	12.654	1.406	55.9	3.6	2.0	0.67	2.99	2.01
9	0.2	8.46	3.852	0.428	20.7	38.6	8.0	2.20	1.82	4.01
10	0.3	8.46	4.428	0.492	27.4	29.2	8.0	1.92	2.09	4.01
11	0.4	8.46	5.004	0.556	35.0	22.9	8.0	1.70	2.37	4.01
12	0.45	8.46	5.292	0.588	39.1	20.4	8.0	1.60	2.50	4.01
13	0.5	8.46	5.58	0.62	43.5	18.4	8.0	1.52	2.64	4.01
14	0.55	8.46	5.868	0.652	48.1	16.6	8.0	1.45	2.77	4.01
15	0.6	8.46	6.156	0.684	52.9	15.1	8.0	1.38	2.91	4.01
16	0.7	8.46	6.732	0.748	63.3	12.6	8.0	1.26	3.18	4.01

Table 5.1: Parameters describing the fabricated hierarchical structures. P_μ, L_μ, and P_n are geometrical parameters used to define the mask file, f_i and Φ_i can be calculated from these. The structures are devided into two sets, space 1-8 with a surface coverage of 2% and space 9-16 with a surface coverage of 8%. For all spaces there is a 9×9 grid of ø300 nm pillars on each microstructure.

5 Exposure of micropillars on DUV stepper.
6 Etching of nanopillars using a DRIE process (mboost).
7 Deposition of FDTS monolayer by molecular vapor deposition (MVD).

The process parameters for the individual steps are printed in Appendix C. In the fabrication process, I choose to use DUV lithography for two reasons, its resolution, and accuracy. The resolution of the DUV stepper is required to resolve the ∅300 nm circular pillars in the first print and the alignment accuracy is needed get the nanopillars centered on the micropillar. To get optimal results, I have arranged the structures on the reticle so the most demanding designs are in the center. This was done since the exposure of the center of the reticle have a higher uniformity of light intensity compared to the edge. The most demanding designs are space 9-12 having the lowest pitch of nanopillars, P_n. To get the desired diameter of ø300 nm on all 16 spaces the dose was optimized for each space individually. The dose needed (D) was found to $150\,\mathrm{J/m^2} < D < 170\,\mathrm{J/m^2}$ for all but space 9, requiring a dose of $220\,\mathrm{J/m^2}$.

The different resist thicknesses in step 1 and 4 are chosen to get optimal resolution in step 1 and good coverage of the 300 nm tall nanostructures in step 4. The etching of microstructures using the mboost recipe was originally chosen to create positively sloped sidewalls for optimal injection molding. The positive sidewall slope has a high chance of producing nanostructures in the etched trenches. This phenomenon is universal to all etching processes etching positive sidewalls since particles masking the etching process will create defects that continue to grow. Examples of these nanostructures between microstructures are seen in the SEM micrographs presented in figure 5.5.

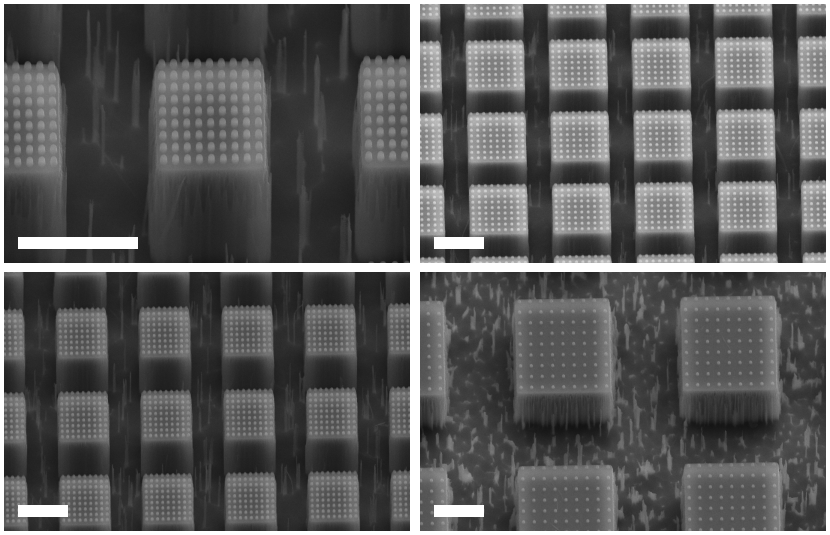

Figure 5.5: SEM images of 4 of the fabricated 16 spaces.

5.2.4 Characterization

The 16 spaces with hierarchical structures have been characterized by contact angle measurements. Initially, the hypothesis to test was that an optimal configuration of micro- and nanopillars in a hierarchical structure would maximize the stability of the Cassie-Baxter state. In literature there have been presented several schemes for testing this stability, by impacting drops[30,119,120], pressed drops[121,122], or pressurized water.[2] I choose to test the stability using impacting drops since many applications for water repellent surfaces focus on repelling

falling water drops. It is thus imperative that the surface can uphold the Cassie-Baxter state during an impact event. A drop impacting on a surface is a much more violent, and uncontrolled, compared to forcing a drop against the surface. I choose the realistic setting over the controlled one since the mechanisms under impact might be crucial for any real applications.

Impact experiments were carried out by dispensing a drop from a needle tip at various height. The drop detaches the needle at a particular volume, given by the circumference of the needle tip (O), surface tension of liquid, and density of the liquid (ρ)

$$V = \frac{O\gamma_{lg}}{\rho g}, \tag{5.5}$$

where g is the gravitational acceleration. The diameter of the standard needle used at the Attension Theta optical tensiometer is 300 μm, resulting in a detached drop volume of $\approx$ 6.5 μL.

For all 16 spaces, an impacting water drop was not able to pin during impact, even at 1.4 $\frac{\text{m}}{\text{s}}$, corresponding to $\approx$ 20 % of terminal velocity for a 6.5 μL drop.[123]

All surface spaces have also been characterized by measurement of dynamic contact angles using the tilting method. Both using pure water (milli-q) and an 3:1 mixture of milli-q and 96 vol% ethanol. The resulting 24 vol% water-ethanol mixture have approximately half the surface tension compared to water, $\gamma_{lg} \approx 36\,\frac{\text{mN}}{\text{m}}$.[124] By reducing the surface tension, the forces required for rolling a drop off the surface increases, resulting in a larger absolute difference of the roll-off angle. The obtained experimental data are presented in figure 5.6. All contact angles presented in the figure have been fitted using the double elliptic fit described in chapter 4 to get the correct result for the receding angle.

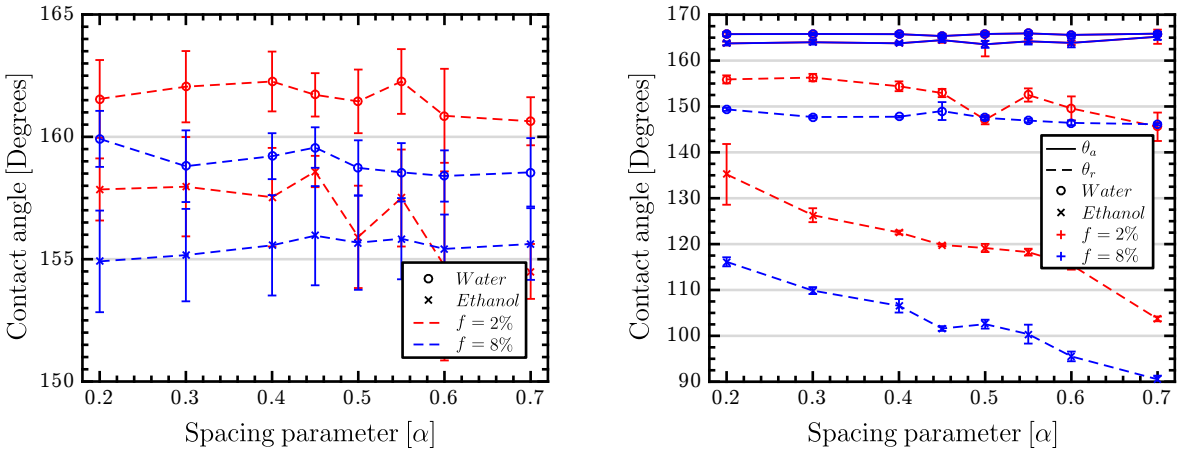

Figure 5.6: Contact angle data for water and 24 vol% ethanol on hierarchical structures. Both the as placed contact angle at zero tilt(left) and dynamic contact angles (right) are shown. Drop size is 10 μL and errorbars are standard deviation from five measurements.

The as placed contact angles plotted in figure 5.6 are very similar in magnitude. As one would expect from the Cassie-Baxter equation the data shows $\theta_{water} > \theta_{ethanol}$ and $\theta_{f=2\%} > \theta_{f=8\%}$. The as placed contact angle does not seem to depend heavily on the spacing parameter α since all data scatter less depending on α than the error bars of the individual data points. The dynamic contact angle does, however, depend heavily on the hierarchical configuration. The contact angle hysteresis monotonically increases for an increase in α.

This cannot be explained by Cassie-Baxter's surface (or line) fraction model or the pinned length model by Paxson, since the surfaces with different α have the same surface fraction and pinned line fractions. From the previous stability analysis, we would expect the opposite result of the measurements since the overall relative deflection is smallest for high values of α according to figure 5.3. I would therefore not expect any wetting transition mechanisms to be the origin of the substantial increase in contact angle hysteresis seen in figure 5.6. That the contact angle hysteresis decreases for a smaller pitch of nanostructures (P_n) is consistent with the performance of most hierarchical structures presented in literature and seen in nature. The nanostructures on these surfaces produced by self-assembly process have tiny structures with close spacing.

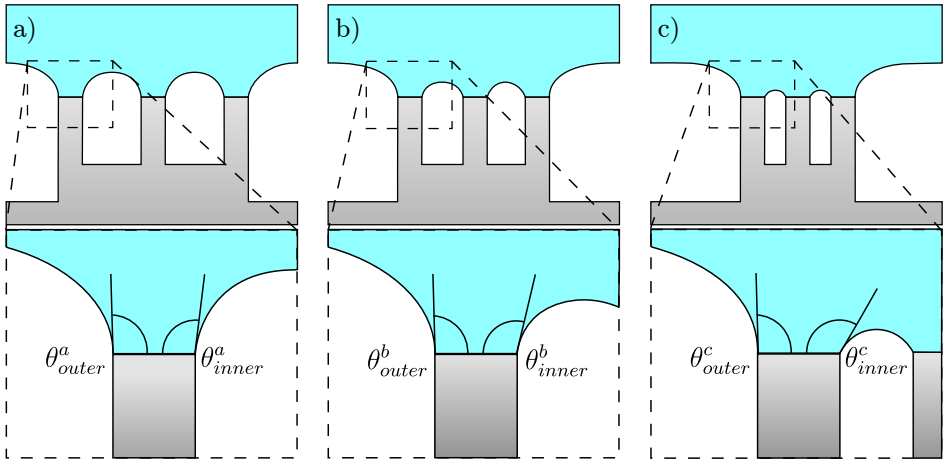

Figure 5.7: Schematic illustration of the interference of distortions. a) Large pitch of nanopillars creates no interference, $\theta^a_{inner} = \theta^a_{outer}$. b) and c) gradually decreasing the pitch will increase interference between menisci, $\theta^c_{inner} > \theta^b_{inner} > \theta^{b,c}_{outer}$

From the experiments it is seen that the contact angle hysteresis is highly dependent on the configuration of the micro- and nanopillars, despite the structures have the same line and surface density that the drop needs to detach to roll off the surface. It is my hypothesis that this effect originates from interference between separate pillars distortion of the meniscus. In many simple models calculating the forces at the triple line, it is assumed that there is no interference between distortions made by different structures.[33,71,125] In the paper by Paxson and Varanasi they do however notice that when the pitch gets sufficiently small, there will be interference between the distortions of the menisci. The concept of interfering distortions is schematically drawn in figure 5.7. The total force needed to de-pin the drop from the microstructure is according to Paxson and Varanasi

$$F_\mu = \oint_O \gamma_{lg} \sin\theta \mathrm{d}s \tag{5.6}$$

where θ is the local contact angle on top of a nanopillar when the drop detaches, and O is the perimeter of all nanopillars on the microstructure. In this equation, the drop is assumed to move vertically off the surface, a good approximation for the high receding angles of the macroscopic drop. In the 2D case sketched in figure 5.7 the force from the inner contact angle will scale directly with the distance between pillars

$$\sin\theta_{inner} = \frac{s}{2R}, \tag{5.7}$$

where s is the spacing between pillars and R is the radius of curvature. Equation 5.6 and 5.7 suggest that there should be a linear relation between the force needed to de-pin a

microstructure and the spacing between the nanostructures on top. Probably with some offset from the contribution from the integral over θ_{outer}. The force required to move a drop across a surface is according to the Furmidge equation given by[96]

$$F_r = \gamma_{lg} d(\cos\theta_r - \cos\theta_a), \tag{5.8}$$

where d is the diameter of the drop. Using the diameter for a 10 μL drop with a contact angle of 160°, and normalizing the force F_r with the total pinned fraction Φ_h i have plotted the data from 5.6 in figure 5.8. The advancing contact angle in the Furmidge equation is set to 180° according to the model described in chapter 2.

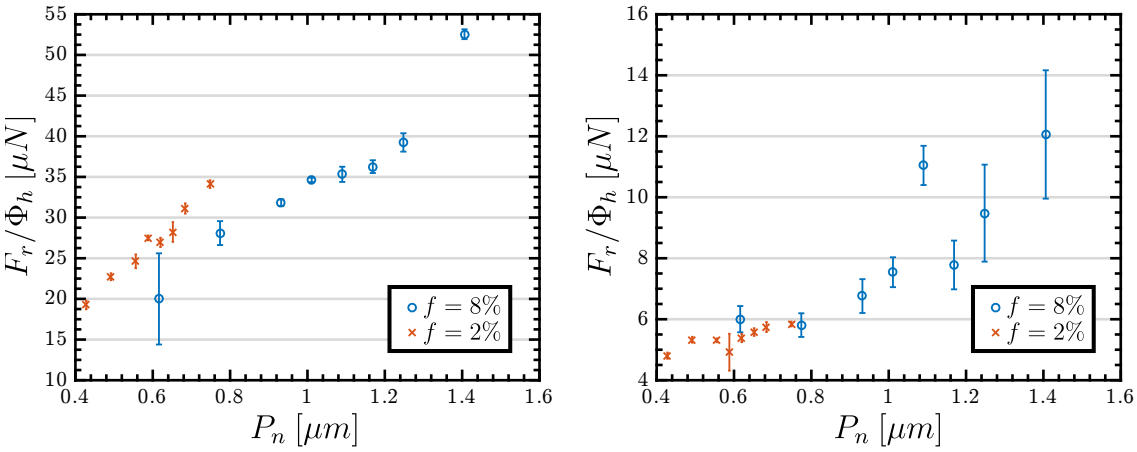

Figure 5.8: Normalized force required to roll a drop off the surface, as a function of nanopillar pitch. Left graph is data for 24 vol% ethanol and right graph is for water.

For each dataset plotted in 5.8 there is a clear linear trend, maybe except the results for water on $f = 8\,\%$ where many of the data points are rather noisy. This linear trend seems to confirm that the hypothesis of interference between pillars can play a major role in the working principle of hierarchical structures. Since the force required is linearly correlated with the spacing between posts it would favor water-repellent structure comprising of tiny top level structures. This result is consistent with many natural water repellent surfaces.[7,111]

The content in this section has not been published but is expected to be so after the hand in of this thesis.

6

TransForm Technologies

In 2013 I was at the European School on Nanosciences and Nanotechnologies (ESONN) in Grenoble as a part of my Ph.d. study. During the summer school, there was a poster session where all attendees presented their field of work. During the poster session, I talked with Carl Esben Poulsen who had, in collaboration with Kasper Kistrup, been trying to create welding seems for ultrasonic welding using laser ablation instead of conventional micro milling. Instead of getting the desired welding seems they had created a peculiar microstructure, looking like micron sized craters, in the mold surface. These craters were not ablated individually but emerged as an effect of the laser-based surface treatment. During this poster session, we realized the similarities between their micro holes and my mold inserts produced in the clean room. After returning from the summer school, we began exploring the possibility of using this laser structuring technique to create molds for molding superhydrophobic polymer parts. This was the start of the TransForm project.

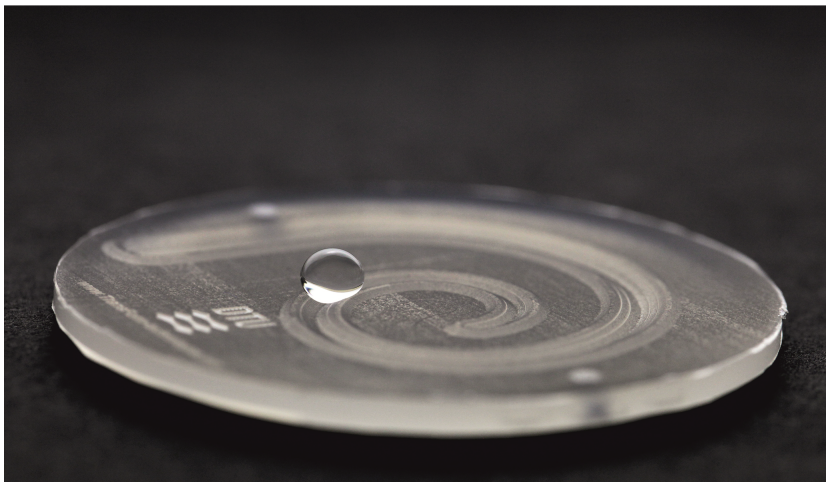

Figure 6.1: Photograph of water drop on polypropylene part structured by TransForm structures. The part features a water repellent grove that guides the droplet, part diameter is 50 mm.

After some investigation of this new structuring technique, it became apparent that this new microstructuring technology was able to produce parts that were very water repellent. In fact, they were much more water repellent than any surface previously made by injection molding at DTU. In addition to the superior performance, we saw several benefits of this technology over competing methods for micro-structuring molds. When comparing to micro milling, clean room fabrication or direct laser writing the TransForm technology have several benefits:

- Laser based, meaning easy transition from planar surfaces to full 3D mold cavities
- Able to micro structuring existing tools in hardened tool steel, no need for nickel, etc.
- Extremely fast, able to microstructure an area of 1 cm^2 in less than 5 min.
- None of the other structuring techniques have been able to create a superhydrophobic surface by isothermal molding.

Due to these significant benefits we filed a patent application for the developed structuring method, enclosed in Appendix F, and the use of the structures to produce a water-repellent surface, attached in Appendix G.

To show geometrical freedom of the laser-based technique, we created a part with a spiral groove with superhydrophobic structures. A drop placed in the grove will thus be able to roll along groove with little resistance. A photograph of a drop placed in the groove is shown in figure 6.1 with a video available online.[126]

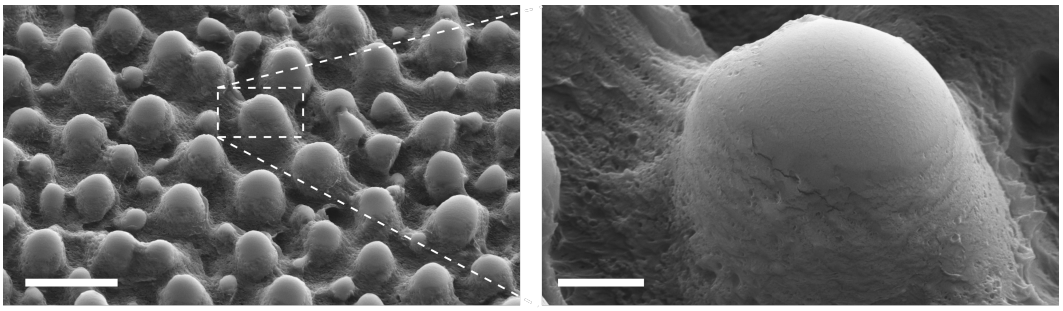

a) b)

Figure 6.2: a) SEM micrograph the TransForm structures replicated in PP scale bar is 20 μm b) Zoom in on a single pillar top, scale bar is 3 μm. The sample is tilted by 30°

The microstructures arise as a result of a surface treatment rather than individual machining of each structure. This gives rise to the random placement of structures seen in figure 6.2 a. By varying the process parameters we can control density and size distribution of structures, but not their individual position. Using the graphs presented in the three patents, we are thereby able to tune the geometry to our need.

All variants of the TransForm structures look very similar to what is shown in figure 6.2. The surface structure in the polymer arises from microscopic craters in the mold surface. During isothermal molding, the holes are partly filled resulting in super smooth top of pillars, seen in figure 6.2. At the side wall of the pillar shown in figure 6.2 b it is clear that the bottom part of the sidewall have a surface roughness from the mold where the top part is very smooth. By changing the molding conditions the intrusion into the crater can be controlled, in turn, affecting the wetting properties of the surface. This is illustrated by the set of SEM micrographs presented in figure 6.3.

The SEM images in figure 6.3 have been taken close to the center of the sample and in the same place of every part. This enables us to direct comparing of the structural changes from the molding process. From the images, it seems that the biggest structural change is from 30°C to 50°C with only minor modifications from 50°C to 80°C. From 30°C to 50°C there is a significant increase in the filling of the structures and a reduction of the scratching of structures during demolding. The increased filling is due to the decreased cooling rate enabling the polymer to flow longer into the cavity before solidifying. The reduced scratching is due to the polymer part being hotter when demolding, minimizing the shrinkage of the

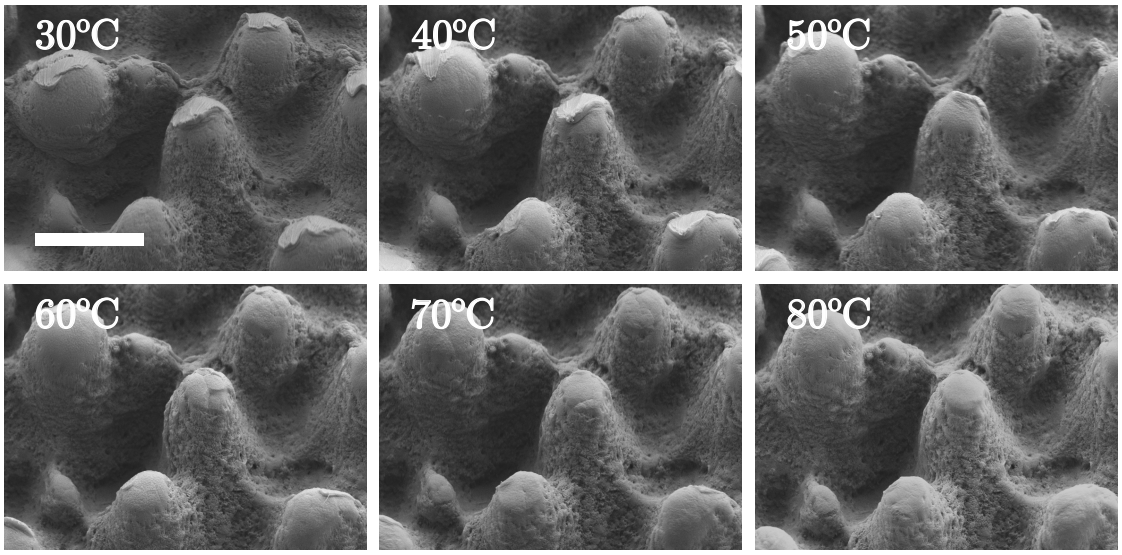

Figure 6.3: SEM micrograph of the same set of micro pillars molded with different mold temperatures. The in Scale bar is 10 μm, sample is tilted by 30°.

Mold temperature	30°C	40°C	50°C	60°C	70°C	80°C
Advancing CA	171 ± 3	169 ± 5	171 ± 3	172 ± 4	172 ± 2	161 ± 5
Receding CA	105 ± 22	99 ± 34	132 ± 8	128 ± 8	137 ± 5	139 ± 9

Table 6.1: Advancing and receding contact angles for samples produced by different mold temperatures. The large uncertainty on 30° and 40° is due to a chance of severe pinning of the drop. Uncertainty is standard deviation of measurements on 6 identical samples.

macroscopic part. By reducing the shrinkage, there will be fewer forces pulling the sideways in the structures during demolding, resulting in less scratching.

When looking closely at the micrographs from 50° to 80°, there is a continued reduction of scratches, on e.g. the bottom right pillar. This decrease of scratches is also seen on the wetting behavior of sample produced by the six molding temperatures. In table 6.1 I have printed the advancing and receding contact angles measured on samples produced by the six different mold temperatures. There is a significant increase in the receding angle between the samples made with mold temperatures of 40°C and 50°C, and a smaller increase between 60°C and 70°C. It is only the samples produced with 70°C and 80°C mold temperatures that I would classify as a truly water repellent surface. For the samples produced with 30°C and 40°C a 10 μL drop on the surface is stuck, for 50°C and 60°C the drop will roll off at angles $\geq 10°$. For the sample produced with 70°C and 80°C mold temperatures a 10 μL drop will roll off at the slightest tilt $\approx 1° - 2°$. The SEM micrographs in figure 6.3 combined with the data in table 6.1 suggests that a successful replication of TransForm structures relies on a combination of aspect ratio and smoothness of pillar tops. This is consistent with theoretical prediction.[31,121]

Box 6.1: Ultrasonic Welding

Ultrasonic welding is a process for joining parts, typically made of polymer, using ultrasonic sound. A schematic drawing of the ultrasonic welding process is presented in figure 6.4. Ultrasonic welding is performed by passing sound waves through two joined objects that are made so they only touch in a small area, figure 6.4 a-b. When the sound propagates through the parts the energy density increases drastically in the small area connecting the parts, figure 6.4 c. The increased energy density locally melts the polymer fusing the two pieces together, figure 6.4 d.

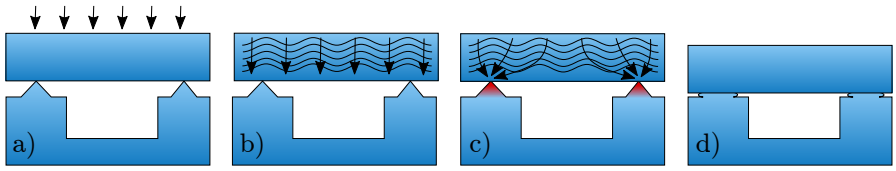

Figure 6.4: a) Two polymer parts are pressed together, only touching in a small cross section. b) Ultrasonic waves are send thorugh the top part. c) The sound waves are focused when passing form the top part to the bottom part. Melting the polymer at the touching points d) The molten polymer fuses the parts together.

Parts used for ultrasonic welding are often produced with a surface structure designed to guide the sound waves. These structures are referred to as energy directors, and they make up the welding seam.

Ultrasonic welding is widely used in industry since it is

- Fast and cheap.
- Easy to automate.
- Not using any chemicals.
- Able to fuse parts made of different material.

At DTU Nanotech there has been some research in using ultrasonic welding for microfluidic devices.[127–129] The four main challenges for this implementation are

1 Small devices requires small energy directors. This requires tiny milling tools operated with high precision.
2 Energy directors are often needed on top of channel walls. The top of the walls are trenches in the tool, that can be difficult to machine.
3 The melted energy director either creates a small gap or flows into the microfluidic channel, distorting the desired geometry.
4 During the welding process there is a lot of vibration that has been known to generate particles.

At some point, we decided to try using the TransForm structures as energy directors for ultrasonic welding. This proved to solve most of the difficulties in using ultrasonic welding for lab-on-a-chip devices. By creating microscopic protrusions on the surface of the part, there is the same increase in energy density as for the conventional energy director. The difference being, that instead of one there would be thousands microscopic energy directors to generate the joint. Microscopic energy directors directly solve point 1-3. First, the laser engraving has very high precision compared to the milling; alignment is within a few microns. Second,

The laser beam has no problems structuring the bottom of the cavity. Third, the height and volume of melted polymer are much smaller for microscopic energy directors compared to conventional ones. We did also show that we got no particle formation during the welding, this was later shown not to be attributed to the microscopic energy directors but rather the clamping technique employed. These points are explained in detail in the paper attached in Appendix D. Due to the clear benefits of using TransForm structures as energy directors in microfluidic devices we filed another patent application, enclosed in Appendix H.

The excellent water repellent performance shown by the TransForm structure was quite surprising considering the general design rules for such a surface. The water repellent TransForm structure has an aspect ratio of approximately one, a much higher surface coverage of microstructures, and no hierarchical structures. Since this discovery was at an early stage of my Ph.D. study, much of the later research was inspired by this curiosity. To determine the driving factor behind the water repellency of the TransForm structure, I have tried to create structures with a rounded top, irregular structures, and structures of different height. In all cases, the performance of the clean room fabricated structure was much lower than that of TransForm structures.

After filing the patent applications, we were able to get external funding for maturing the technology. The funding enabled Kasper Kistrup, Carl Esben Poulsen and me to go on leave for 1.5, 8.5, and 4 months, respectively. During this time we

- Structured commercial injection molding tools.
- Used commercial tools to assess lifetime of microstructures.
- Tested anti-fouling, water repellency, ultrasonic welding, and friction reduction, in an industrial setting.
- Filed the fourth notification of invention, where the TransForm structures are combined with coatings.
- Build a setup for the seamless structuring of a cylindrical mold used in roll-to-roll fabrication.
- Studied bacterial and cellular growth on microstructured samples.

The results of these investigations are not made public due to the different commercial interests.

7

Conclusion and outlook

In recent years there have been many demonstrations of how surface structures can create surfaces with novel functionalities, such as liquid repellent, anti-fogging, or self-cleaning. Compared to the overwhelming interest in this subject in the scientific community there have been few examples of such structures in commercial products. In the POLYMIC group, we believe that this is due to the lack of demonstrations using commercially relevant production platforms.

The aim of this project was to enable the fabrication of surfaces with controlled wetting by injection molding. The initial plan was to gain insights into wetting and de-wetting mechanisms, combined with a thorough understanding of the fabrication process. This combination of knowledge within fundamental theory and limitations in fabrication enables a design for manufacturing approach that is needed to successfully injection mold a water repellent surface.

Early in the project, I was co-inventor of a technology facilitating the production of water repellent surfaces by injection molding. With this, it is possible to produce superhydrophobic parts by directly structuring commercial grade steel molds, and using an isothermal injection molding process. The possibility to structure hardened steel and use fast isothermal molding cycles are crucial to a commercial adaptation of the technology.

The early discovery of this technology reversed the initial plan for the project. We were able to produce water-repellent surfaces on an industrial mass production platform but the underlying mechanics generating the functional surface was not entirely clear. To uncover these mechanics, I have conducted several studies of the wetting behavior on micro- and nanostructured surfaces. The primary focus of these studies were to determine the differences between the regular structures produced by planar processes in the clean room and the biomimetic structures generated by the patented structuring technique.

In the first study I found that irregular hole-like structures increase the adhesion of drops, inhibiting movement. To explain this, we derived a simple model based on the increase line density for increasing irregularity of structures.

In the second study, I developed a clean room based fabrication technique capable of mimicking some of the organic shapes seen on natural water repellent surfaces. The resulting structures had multiple heights, rounded corners, and was randomly distributed on the surface. Contact angle measurements revealed that the random distribution of surface structures produces numerous pinning sites for drops resting on the surface.

For a better theoretical understanding of wetting phenomena, I have made a simulation of underwater wetting transitions. The developed simulation scheme can accurately predict the wetting transition of submerged microcavities wetted by a pressurized water column. The

wetting transition is found to be governed by the diffusion of gas into the water column, the dynamic wetting properties of the surface, and the particular geometry of the microcavity.

Most dynamic contact angles presented in the thesis have been measured by the tilting method. The receding contact angles measured in an tilting experiment are often wrongly fitted due to optical defects on the rear side of the tilted drop. I have developed and implemented a novel fitting method using double sided elliptical fit to overcome this issue. By using double sided elliptical fit, it is proven possible to fit the receding contact angle accurately, even with severe optical defects.

Lastly, I have designed and fabricated a range of hierarchical structures challenging the state of the art wetting theories for such surfaces. By employing a model taking into account the local configuration of nanostructures at the triple line, it is possible to explain the observations.

Through the invention of the TransForm structuring technique, it has been possible to show numerous industrial partners the possibilities of using microstructured molding tools. By proving that it is possible to realize microstructured polymer parts using industrial production methods, we have initiated the commercial adaptation of this technology.

Further work within the field of structural wetting in the POLYMIC group will be focused on producing functional surfaces on polymer foils using roll-to-roll processing. The activities are also moving entirely into the nanoscale, enabling anti-reflective surfaces with particular wetting properties.

Bibliography

[1] Ritika Singh Petersen, Rasoul Mahshid, Nis Korsgaard Andersen, Stephan Sylvest Keller, Hans Nørgaard Hansen, and Anja Boisen. "Hot embossing and mechanical punching of biodegradable microcontainers for oral drug delivery". In: *Microelectronic Engineering* 133 (2015), pp. 104–109. DOI: 10.1016/j.mee.2014.11.009.

[2] Emil Søgaard, Nis K Andersen, Kristian Smistrup, Simon T Larsen, Ling Sun, and Rafael Taboryski. "Study of Transitions between Wetting States on Microcavity Arrays by Optical Transmission Microscopy". In: *Langmuir* 30.43 (2014), pp. 12960–12968. DOI: 10.1021/la502855g.

[3] Christian Rytka, Nadia Opara, Nis Korsgaard Andersen, Per Magnus Kristiansen, and Andreas Neyer. "On The Role of Wetting, Structure Width, and Flow Characteristics in Polymer Replication on Micro- and Nanoscale". In: *Macromolecular Materials and Engineering* 301.5 (2016), pp. 597–609. DOI: 10.1002/mame.201500350.

[4] C E POULSEN, A Wolff, N K ANDERSEN, K KISTRUP, and R Taboryski. *Replication tool and method of providing a replication tool*. 2016. URL: https://www.google.dk/patents/WO2016075276A1?cl=en.

[5] C E POULSEN, A Wolff, N K ANDERSEN, K KISTRUP, and R Taboryski. *Micro-scale energy directors for ultrasonic welding*. 2016. URL: https://www.google.dk/patents/WO2016075272A1?cl=en.

[6] C E POULSEN, A Wolff, N K ANDERSEN, K KISTRUP, and R Taboryski. *Method of producing an item with enhanced wetting properties by fast replication and replication tool used in the method*. 2016. URL: https://www.google.com/patents/WO2016075273A1?cl=en.

[7] W Barthlott, C Neinhuis, Heliconia Verlot, and Colocasia L Schott. "Purity of the sacred lotus , or escape from contamination in biological surfaces". In: (1997), pp. 1–8.

[8] N. J. Shirtcliffe, G. McHale, and M. I. Newton. "Learning from Superhydrophobic Plants: The Use of Hydrophilic Areas on Superhydrophobic Surfaces for Droplet Control Part of the "Langmuir 25th Year: Wetting and superhydrophobicity" special issue." In: *Langmuir* 25.24 (2009), pp. 14121–14128. DOI: 10.1021/la901557d.

[9] Kerstin Koch and Wilhelm Barthlott. "Superhydrophobic and superhydrophilic plant surfaces: an inspiration for biomimetic materials." In: *Philosophical transactions. Series A, Mathematical, physical, and engineering sciences* 367.1893 (2009), pp. 1487–509. DOI: 10.1098/rsta.2009.0022.

[10] A. B. D. Cassie and S. Baxter. "Wettability of porous surfaces". In: *Transactions of the Faraday Society* 40.5 (1944), p. 546. DOI: 10.1039/tf9444000546.

[11] S. Wang and L. Jiang. "Definition of Superhydrophobic States". In: *Advanced Materials* 19.21 (2007), pp. 3423–3424. DOI: 10.1002/adma.200700934.

[12] Wen Li and Alidad Amirfazli. "Superhydrophobic surfaces: Adhesive strongly to water?" In: *Advanced Materials* 19.21 (2007), pp. 3421–3422. DOI: 10.1002/adma.200601764.

[13] Eyal Bittoun and Abraham Marmur. "The role of multiscale roughness in the Lotus effect: is it essential for super-hydrophobicity?" In: *Langmuir : the ACS journal of surfaces and colloids* 28.39 (2012), pp. 13933–42. DOI: 10.1021/la3029512.

[14] Bharat Bhushan, Yong Chae Jung, and Kerstin Koch. "Micro-, nano- and hierarchical structures for superhydrophobicity, self-cleaning and low adhesion". In: *Philosophical Transactions of the Royal Society A: Mathematical, Physical and Engineering Sciences* 367.1894 (2009), pp. 1631–1672. DOI: 10.1098/rsta.2009.0014.

[15] Doo Jin Lee, Hyung Min Kim, Young Seok Song, and Jae Ryoun Youn. "Water droplet bouncing and superhydrophobicity induced by multiscale hierarchical nanostructures." In: *ACS nano* 6.9 (2012), pp. 7656–64. DOI: 10.1021/nn3032547.

[16] Elena Celia, Thierry Darmanin, Elisabeth Taffin de Givenchy, Sonia Amigoni, and Frédéric Guittard. "Recent advances in designing superhydrophobic surfaces." In: *Journal of colloid and interface science* 402 (2013), pp. 1–18. DOI: 10.1016/j.jcis.2013.03.041.

[17] Takashi Nishino, Masashi Meguro, Katsuhiko Nakamae, Motonori Matsushita, and Yasukiyo Ueda. "The Lowest Surface Free Energy Based on -CF 3 Alignment". In: *Langmuir* 15.13 (1999), pp. 4321–4323. DOI: 10.1021/la981727s.

[18] Zhiguang Guo and Weimin Liu. “Biomimic from the superhydrophobic plant leaves in nature: Binary structure and unitary structure”. In: *Plant Science* 172.6 (2007), pp. 1103–1112. DOI: 10.1016/j.plantsci.2007.03.005.

[19] C W Extrand. “Criteria for Ultralyophobic Surfaces”. In: *Langmuir* 20.12 (2004), pp. 5013–5018. DOI: 10.1021/la036481s.

[20] John Oliver. *Bioinspired and Nanoengineered Surfaces: Technologies, Applications and Global Markets*. 2013. ISBN: 1-56965-429-8.

[21] Kyoo-Chul Park, Hyungryul J Choi, Chih-Hao Chang, Robert E Cohen, Gareth H McKinley, and George Barbastathis. “Nanotextured silica surfaces with robust superhydrophobicity and omnidirectional broadband supertransmissivity.” In: *ACS nano* 6.5 (2012), pp. 3789–99. DOI: 10.1021/nn301112t.

[22] Wikipedia. *Waterproof phones*. URL: https://en.wikipedia.org/wiki/IP{_}Code (visited on 08/03/2016).

[23] Teknologisk Institut. *Waterproof hearing aid*. 2013. URL: http://www.teknologisk.dk/ydelser/danmarks-foerste-nano-fabrik-er-klar-til-produktion/33056 (visited on 08/03/2016).

[24] Estc May and Las Vegas. “Understanding Nanocoating Technology”. In: May (2013).

[25] S Dimitrov, V Kamenska, J.D. Walker, W Windle, R Purdy, M Lewis, and O Mekenyan. “Predicting the biodegradation products of perfluorinated chemicals using CATABOL”. In: *SAR and QSAR in Environmental Research* 15.1 (2004), pp. 69–82. DOI: 10.1080/1062936032000169688.

[26] Peter J. Lasier, John W. Washington, Sayed M. Hassan, and Thomas M. Jenkins. “Perfluorinated chemicals in surface waters and sediments from northwest Georgia, USA, and their bioaccumulation in Lumbriculus variegatus”. In: *Environmental Toxicology and Chemistry* 30.10 (2011), pp. 2194–2201. DOI: 10.1002/etc.622.

[27] Liangliang Cao, Andrew K. Jones, Vinod K. Sikka, Jianzhong Wu, and Di Gao. “Anti-Icing Superhydrophobic Coatings”. In: *Langmuir* 25.21 (2009), pp. 12444–12448. DOI: 10.1021/la902882b.

[28] Olivier Parent and Adrian Ilinca. “Anti-icing and de-icing techniques for wind turbines: Critical review”. In: *Cold Regions Science and Technology* 65.1 (2011), pp. 88–96. DOI: 10.1016/j.coldregions.2010.01.005.

[29] Liangliang Cao, Hsin-Hua Hu, and Di Gao. “Design and fabrication of micro-textures for inducing a superhydrophobic behavior on hydrophilic materials.” In: *Langmuir : the ACS journal of surfaces and colloids* 23.8 (2007), pp. 4310–4. DOI: 10.1021/la063572r.

[30] Yong Chae Jung and Bharat Bhushan. “Dynamic effects of bouncing water droplets on superhydrophobic surfaces.” In: *Langmuir : the ACS journal of surfaces and colloids* 24.12 (2008), pp. 6262–6269.

[31] Joseph W Krumpfer, Pei Bian, Peiwen Zheng, Lichao Gao, and Thomas J McCarthy. “Contact angle hysteresis on superhydrophobic surfaces: an ionic liquid probe fluid offers mechanistic insight.” In: *Langmuir : the ACS journal of surfaces and colloids* 27.6 (2011), pp. 2166–9. DOI: 10.1021/la105068c.

[32] Choongyeop Lee and Chang-Jin C J Kim. “Maximizing the giant liquid slip on superhydrophobic microstructures by nanostructuring their sidewalls.” In: *Langmuir : the ACS journal of surfaces and colloids* 25.21 (2009), pp. 12812–8. DOI: 10.1021/la901824d.

[33] Adam T Paxson and Kripa K Varanasi. “Self-similarity of contact line depinning from textured surfaces.” In: *Nature communications* 4 (2013), p. 1492. DOI: 10.1038/ncomms2482.

[34] Hoon Eui Jeong, Moon Kyu Kwak, Chan Ick Park, and Kahp Yang Suh. “Wettability of nanoengineered dual-roughness surfaces fabricated by UV-assisted capillary force lithography.” In: *Journal of colloid and interface science* 339.1 (2009), pp. 202–7. DOI: 10.1016/j.jcis.2009.07.020.

[35] Ramasamy Thangavelu Rajendra Kumar, Klaus Bo Mogensen, and Peter Bøggild. “Simple Approach to Superamphiphobic Overhanging Silicon Nanostructures”. In: *The Journal of Physical Chemistry C* 114.7 (2010), pp. 2936–2940. DOI: 10.1021/jp9066422.

[36] Esa Puukilainen, Tiina Rasilainen, Mika Suvanto, and Tapani a Pakkanen. “Superhydrophobic polyolefin surfaces: controlled micro- and nanostructures.” In: *Langmuir : the ACS journal of surfaces and colloids* 23.13 (2007), pp. 7263–8. DOI: 10.1021/la063588h.

[37] Eero Huovinen, Janne Hirvi, Mika Suvanto, and Tapani a Pakkanen. "Micro-micro hierarchy replacing micro-nano hierarchy: a precisely controlled way to produce wear-resistant superhydrophobic polymer surfaces." In: *Langmuir : the ACS journal of surfaces and colloids* 28.41 (2012), pp. 14747–55. DOI: 10.1021/la303358h.

[38] Tiina Rasilainen, Anna Kirveslahti, Pauliina Nevalainen, Mika Suvanto, and Tapani a. Pakkanen. "Controlling the Movement of Water Droplets With Micro- and Hierarchical Micro/-Nanostructures". In: *Surface Review and Letters* 18.05 (2011), pp. 209–222. DOI: 10.1142/S0218625X11014679.

[39] Inka Saarikoski, Fatima Joki-Korpela, Mika Suvanto, Tuula T. Pakkanen, and Tapani a. Pakkanen. "Superhydrophobic elastomer surfaces with nanostructured micronails". In: *Surface Science* 606.1-2 (2012), pp. 91–98. DOI: 10.1016/j.susc.2011.09.005.

[40] Hanna-Kaisa Koponen, Inka Saarikoski, Tuulia Korhonen, Marjo Pääkkö, Risto Kuisma, Tuula T. Pakkanen, Mika Suvanto, and Tapani a. Pakkanen. "Modification of cycloolefin copolymer and poly(vinyl chloride) surfaces by superimposition of nano- and microstructures". In: *Applied Surface Science* 253.12 (2007), pp. 5208–5213. DOI: 10.1016/j.apsusc.2006.11.039.

[41] Tiina Rasilainen, Anna Kirveslahti, Pauliina Nevalainen, Mika Suvanto, and Tapani a. Pakkanen. "Modification of polypropylene surfaces with micropits and hierarchical micropits/nanodepressions". In: *Surface Science* 604.21-22 (2010), pp. 2036–2042. DOI: 10.1016/j.susc.2010.08.018.

[42] Q F Xu, B Mondal, and a M Lyons. "Fabricating Superhydrophobic Polymer Surfaces with Excellent Abrasion Resistance by a Simple Lamination Templating Method". In: *Acs Applied Materials & Interfaces* 3.9 (2011), pp. 3508–3514.

[43] Edward Bormashenko and Yelena Bormashenko. "Wetting of composite surfaces: When and why is the area far from the triple line important?" In: *Journal of Physical Chemistry C* 117.38 (2013), pp. 19552–19557. DOI: 10.1021/jp407171v.

[44] David R. Tobergte and Shirley Curtis. *Functional Surfaces in Biology*. Vol. 53. 9. Dordrecht: Springer Netherlands, 2009, pp. 1–30. ISBN: 978-1-4020-6696-2. DOI: 10.1007/978-1-4020-6697-9.

[45] Seung-Mo Lee and Tai Hun Kwon. "Mass-producible replication of highly hydrophobic surfaces from plant leaves". In: *Nanotechnology* 17.13 (2006), pp. 3189–3196. DOI: 10.1088/0957-4484/17/13/019.

[46] Jie Feng, Mingda Huang, and Xin Qian. "Fabrication of Polyethylene Superhydrophobic Surfaces by Stretching-Controlled Micromolding". In: *Macromolecular Materials and Engineering* 294.5 (2009), pp. 295–300. DOI: 10.1002/mame.200800331.

[47] Lichao Gao and Thomas J McCarthy. "A perfectly hydrophobic surface (thetaA/thetaR = 180 degrees /180 degrees)." In: *Journal of the American Chemical Society* 128.28 (2006), pp. 9052–3. DOI: 10.1021/ja062943n.

[48] Tak-Sing Wong, Sung Hoon Kang, Sindy K Y Tang, Elizabeth J Smythe, Benjamin D Hatton, Alison Grinthal, and Joanna Aizenberg. "Bioinspired self-repairing slippery surfaces with pressure-stable omniphobicity". In: *Nature* 477.7365 (2011), pp. 443–447. DOI: 10.1038/nature10447.

[49] Holger F Bohn and Walter Federle. "Insect aquaplaning: Nepenthes pitcher plants capture prey with the peristome, a fully wettable water-lubricated anisotropic surface". In: *Proceedings of the National Academy of Sciences* 101.39 (2004), pp. 14138–14143. DOI: 10.1073/pnas.0405885101.

[50] Philseok Kim, Tak-Sing Wong, Jack Alvarenga, Michael J Kreder, Wilmer E. Adorno-Martinez, and Joanna Aizenberg. "Liquid-Infused Nanostructured Surfaces with Extreme Anti-Ice and Anti-Frost Performance". In: *ACS Nano* 6.8 (2012), pp. 6569–6577. DOI: 10.1021/nn302310q.

[51] Alexander K Epstein, Tak-Sing Wong, Rebecca a Belisle, Emily Marie Boggs, and Joanna Aizenberg. "Liquid-infused structured surfaces with exceptional anti-biofouling performance". In: *Proceedings of the National Academy of Sciences of the United States of America* 109.33 (2012), pp. 13182–13187. DOI: 10.1073/pnas.1201973109.

[52] Simone Tanzi, Peter Friis Østergaard, Marco Matteucci, Thomas Lehrmann Christiansen, Jiri Cech, Rodolphe Marie, and Rafael Taboryski. "Fabrication of combined-scale nano- and microfluidic polymer systems using a multilevel dry etching, electroplating and molding pro-

cess". In: *Journal of Micromechanics and Microengineering* 22.11 (2012), p. 115008. DOI: 10.1088/0960-1317/22/11/115008.

[53] Marco Matteucci, Thomas Lehrmann Christiansen, Simone Tanzi, Peter Friis Østergaard, Simon Tylsgaard Larsen, and Rafael Taboryski. "Fabrication and characterization of injection molded multi level nano and microfluidic systems". In: *Microelectronic Engineering* 111 (2013), pp. 294–298. DOI: 10.1016/j.mee.2013.01.060.

[54] Michael J Hey and David W Wood. "Estimation of liquid / vapor interfacial thicknesses from surface energies". In: *Journal of Colloid and Interface Science* 90.1 (1982), pp. 277–279. DOI: 10.1016/0021-9797(82)90419-2.

[55] Nis Korsgaard Andersen. "Injection moulding and characterisation of self-cleaning surfaces". Master. Technical University of Denmark, 2012.

[56] T. Young. "An Essay on the Cohesion of Fluids". In: *Philosophical Transactions of the Royal Society of London* 95.0 (1805), pp. 65–87. DOI: 10.1098/rstl.1805.0005.

[57] Robert N. Wenzel. "RESISTANCE OF SOLID SURFACES TO WETTING BY WATER". In: *Industrial & Engineering Chemistry* 28.8 (1936), pp. 988–994. DOI: 10.1021/ie50320a024.

[58] R. Shuttleworth and G. L. J. Bailey. "The spreading of a liquid over a rough solid". In: *Discussions of the Faraday Society* 3.16 (1948), p. 16. DOI: 10.1039/df9480300016.

[59] H. Y. Erbil. "Determination of the peripheral contact angle of sessile drops on solids from the rate of evaporation". In: *Journal of Adhesion Science and Technology* 13.12 (1999), pp. 1405–1413. DOI: 10.1163/156856199X00550.

[60] Robert J. Good and M. N. Koo. "The effect of drop size on contact angle". In: *Journal of Colloid And Interface Science* 71.2 (1979), pp. 283–292. DOI: 10.1016/0021-9797(79)90239-X.

[61] M. E R Shanahan and A. Carre. "Viscoelastic Dissipation in Wetting and Adhesion Phenomena". In: *Langmuir* 11.4 (1995), pp. 1396–1402. DOI: 10.1021/la00004a055.

[62] Rafael Tadmor, Prashant Bahadur, Aisha Leh, Hartmann E. N'guessan, Rajiv Jaini, and Lan Dang. "Measurement of Lateral Adhesion Forces at the Interface between a Liquid Drop and a Substrate". In: *Physical Review Letters* 103.26 (2009), p. 266101. DOI: 10.1103/PhysRevLett.103.266101.

[63] C.O Timmons and W.a Zisman. "The effect of liquid structure on contact angle hysteresis". In: *Journal of Colloid and Interface Science* 22.2 (1966), pp. 165–171. DOI: 10.1016/0021-9797(66)90080-4.

[64] Lichao Gao and Thomas J McCarthy. "Contact angle hysteresis explained." In: *Langmuir : the ACS journal of surfaces and colloids* 22.14 (2006), pp. 6234–7. DOI: 10.1021/la060254j.

[65] J David Smith, Rajeev Dhiman, Sushant Anand, Ernesto Reza-Garduno, Robert E Cohen, Gareth H McKinley, and Kripa K Varanasi. "Droplet mobility on lubricant-impregnated surfaces". In: *Soft Matter* 9.6 (2013), pp. 1772–1780. DOI: 10.1039/c2sm27032c.

[66] Rafael Tadmor. "Line energy and the relation between advancing, receding, and young contact angles." In: *Langmuir : the ACS journal of surfaces and colloids* 20.18 (2004), pp. 7659–64. DOI: 10.1021/la049410h.

[67] Gene Whyman, Edward Bormashenko, and Tamir Stein. "The rigorous derivation of Young, Cassie-Baxter and Wenzel equations and the analysis of the contact angle hysteresis phenomenon". In: *Chemical Physics Letters* 450.4-6 (2008), pp. 355–359. DOI: 10.1016/j.cplett.2007.11.033.

[68] Periklis Papadopoulos et al. "Wetting on the Microscale: Shape of a Liquid Drop on a Microstructured Surface at Different Length Scales". In: *Langmuir* 28.5 (2012), pp. 8392–8398.

[69] Simon Tylsgaard Larsen and Rafael Taboryski. "A Cassie-like law using triple phase boundary line fractions for faceted droplets on chemically heterogeneous surfaces." In: *Langmuir : the ACS journal of surfaces and colloids* 25.3 (2009), pp. 1282–4. DOI: 10.1021/la8030045.

[70] Ling Schneider, Milan Laustsen, Nikolaj Mandsberg, and Rafael Taboryski. "The Influence of Structure Heights and Opening Angles of Micro- and Nanocones on the Macroscopic Surface Wetting Properties". In: *Scientific Reports* 6.February (2016), p. 21400. DOI: 10.1038/srep21400.

[71] Periklis Papadopoulos, Lena Mammen, Xu Deng, Doris Vollmer, and Hans-jürgen Butt. "How superhydrophobicity breaks down". In: *Proceedings of the National Academy of Sciences* 110.9 (2013), pp. 3254–3258. DOI: 10.1073/pnas.1218673110.

[72] Lin Feng, Yanan Zhang, Jinming Xi, Ying Zhu, Nü Wang, Fan Xia, and Lei Jiang. "Petal Effect: A Superhydrophobic State with High Adhesive Force". In: 18 (2008), pp. 4114–4119.

[73] Chan Ick Park, Hoon Eui Jeong, Sung Hoon Lee, Hye Sung Cho, and Kahp Y Suh. "Wetting transition and optimal design for microstructured surfaces with hydrophobic and hydrophilic materials." In: *Journal of colloid and interface science* 336.1 (2009), pp. 298–303. DOI: 10.1016/j.jcis.2009.04.022.

[74] E Bormashenko, a Musin, G Whyman, and M Zinigrad. "Wetting transitions and depinning of the triple line." In: *Langmuir : the ACS journal of surfaces and colloids* 28.7 (2012), pp. 3460–4. DOI: 10.1021/la204424n.

[75] Edward Bormashenko. "Progress in understanding wetting transitions on rough surfaces." In: *Advances in colloid and interface science* (2014), pp. 1–12. DOI: 10.1016/j.cis.2014.02.009.

[76] Michael Nosonovsky and Bharat Bhushan. "Biomimetic superhydrophobic surfaces: multiscale approach." In: *Nano letters* 7.9 (2007), pp. 2633–7. DOI: 10.1021/nl071023f.

[77] Pierre-Gilles de Gennes, Françoise Brochard-Wyart, and David Quéré. *Capillarity and Wetting Phenomena*. New York, NY: Springer New York, 2004, pp. 15–30. ISBN: 978-1-4419-1833-8. DOI: 10.1007/978-0-387-21656-0.

[78] M. E. R. SHANAHAN and P.-G. DE GENNES. "L'arête produite par un coin liquide près de la ligne triple de contact solide/liquide/fluide". fre. In: *Comptes rendus de l'Académie des sciences. Série 2, Mécanique, Physique, Chimie, Sciences de l'univers, Sciences de la Terre* 302.8 (), pp. 517–521.

[79] Rafael Tadmor, Kumud Chaurasia, Preeti S. Yadav, Aisha Leh, Prashant Bahadur, Lan Dang, and Wesley R. Hoffer. "Drop retention force as a function of resting time". In: *Langmuir* 24.17 (2008), pp. 9370–9374. DOI: 10.1021/la7040696.

[80] Hartmann E. N'guessan, Aisha Leh, Paris Cox, Prashant Bahadur, Rafael Tadmor, Prabir Patra, Robert Vajtai, Pulickel M Ajayan, and Priyanka Wasnik. "Water tribology on graphene". In: *Nature Communications* 3 (2012), p. 1242. DOI: 10.1038/ncomms2247.

[81] William Henry. "Experiments on the Quantity of Gases Absorbed by Water, at Different Temperatures, and under Different Pressures". In: *Philosophical Transactions of the Royal Society of London* 93.1 (1803), pp. 29–274. DOI: 10.1098/rstl.1803.0004.

[82] Mansuripur Masud and Liang Rongguang. *Projection Photolithography*. URL: http://www.mmresearch.com/articles/article4/ (visited on 07/26/2016).

[83] *Danchip website*. URL: http://www.danchip.dtu.dk/english/Process-Technology/Equipment/Nanoscale-Lithography (visited on 07/26/2016).

[84] Swiss Litho. *No Title*. URL: https://www.swisslitho.com/ (visited on 08/11/2016).

[85] E.Mello Ceresa and F. Garbassi. "AES/XPS Thickness measurement of the native oxide on single crystal Si wafers". In: *Materials Chemistry and Physics* 9.4 (1983), pp. 371–385. DOI: 10.1016/0254-0584(83)90013-5.

[86] S. Nguyen. "Reaction Mechanisms of Plasma- and Thermal-Assisted Chemical Vapor Deposition of Tetraethylorthosilicate Oxide Films". In: *Journal of The Electrochemical Society* 137.7 (1990), p. 2209. DOI: 10.1149/1.2086914.

[87] Arne Schleunitz, Vitaliy a Guzenko, Martin Messerschmidt, Hakan Atasoy, Robert Kirchner, and Helmut Schift. "Novel 3D micro- and nanofabrication method using thermally activated selective topography equilibration (TASTE) of polymers". In: *Nano Convergence* 1.1 (2014), p. 7. DOI: 10.1186/s40580-014-0007-5.

[88] Helmut Schift, Christian Spreu, Arne Schleunitz, and JaeJong Lee. "Shape control of polymer reflow structures fabricated by nanoimprint lithography". In: *Microelectronic Engineering* 88.1 (2011), pp. 87–92. DOI: 10.1016/j.mee.2010.08.029.

[89] Arne Schleunitz and Helmut Schift. "Fabrication of 3D nanoimprint stamps with continuous reliefs using dose-modulated electron beam lithography and thermal reflow". In: *Journal of Micromechanics and Microengineering* 20.9 (2010), p. 095002. DOI: 10.1088/0960-1317/20/9/095002.

[90] Alexander B. Christiansen, Jeppe Clausen, N. Asger Mortensen, and Anders Kristensen. "Minimizing scattering from antireflective surfaces replicated from low-aspect-ratio black silicon". In: *Applied Physics Letters* 101.13 (2012), p. 131902. DOI: 10.1063/1.4754691.

[91] Beaumontinc. *Melt Density*. URL: http://www.beaumontinc.com/solid-density-vs-melt-density/ (visited on 08/18/2016).

[92] Thomas Lehrmann Christiansen. "Design and Development of a Microfluidic Chip for Electrical Measurements on Biological Cells". Master Thesis. DTU, 2012.

[93] Didem Öner and Thomas J. McCarthy. "Ultrahydrophobic Surfaces. Effects of Topography Length Scales on Wettability". In: *Langmuir* 16.20 (2000), pp. 7777–7782. DOI: 10.1021/la000598o.

[94] Philippe Lalanne and Dominique Lemercier-Lalanne. "On the effective medium theory of subwavelength periodic structures". In: *Journal of Modern Optics* 43.10 (1996), pp. 2063–2086. DOI: 10.1080/095003496154716.

[95] *BiolinScientific*. URL: http://www.biolinscientific.com/product/sigma-range-technical-specifications/ (visited on 07/11/2016).

[96] C.G.L Furmidge. "Studies at phase interfaces. I. The sliding of liquid drops on solid surfaces and a theory for spray retention". In: *Journal of Colloid Science* 17.4 (1962), pp. 309–324. DOI: 10.1016/0095-8522(62)90011-9.

[97] MathWorks. *Matlab edge detectors*. URL: http://se.mathworks.com/discovery/edge-detection.html (visited on 08/01/2016).

[98] Miroslav Hagara and Peter Kulla. "Edge Detection with sub-pixel accuracy based on approximation of Edge with Erf function". In: *Radioengineering* 20.2 (2011), pp. 516–524.

[99] Agustín Trujillo-Pino, Karl Krissian, Miguel Alemán-Flores, and Daniel Santana-Cedrés. "Accurate subpixel edge location based on partial area effect". In: *Image and Vision Computing* 31.1 (2013), pp. 72–90. DOI: 10.1016/j.imavis.2012.10.005.

[100] S. Farshid Chini and A. Amirfazli. "A method for measuring contact angle of asymmetric and symmetric drops". In: *Colloids and Surfaces A: Physicochemical and Engineering Aspects* 388.1-3 (2011), pp. 29–37. DOI: 10.1016/j.colsurfa.2011.08.001.

[101] a. F. Stalder, G. Kulik, D. Sage, L. Barbieri, and P. Hoffmann. "A snake-based approach to accurate determination of both contact points and contact angles". In: *Colloids and Surfaces A: Physicochemical and Engineering Aspects* 286.1-3 (2006), pp. 92–103. DOI: 10.1016/j.colsurfa.2006.03.008.

[102] J. Zimmermann, Stefan Seeger, and F. A. Reifler. "Water Shedding Angle: A New Technique to Evaluate the Water-Repellent Properties of Superhydrophobic Surfaces". In: *Textile Research Journal* 79.17 (2009), pp. 1565–1570. DOI: 10.1177/0040517509105074.

[103] A. Kalantarian, R. David, and A. W. Neumann. "Methodology for High Accuracy Contact Angle Measurement †". In: *Langmuir* 25.24 (2009), pp. 14146–14154. DOI: 10.1021/la902016j.

[104] Y Rotenberg, L Boruvka, and A.W Neumann. "Determination of surface tension and contact angle from the shapes of axisymmetric fluid interfaces". In: *Journal of Colloid and Interface Science* 93.1 (1983), pp. 169–183. DOI: 10.1016/0021-9797(83)90396-X.

[105] Ehsan Atefi, J. Adin Mann, and Hossein Tavana. "A robust polynomial fitting approach for contact angle measurements". In: *Langmuir* 29.19 (2013), pp. 5677–5688. DOI: 10.1021/la4002972.

[106] M. G. Cabezas, A. Bateni, J. M. Montanero, and A. W. Neumann. "A new drop-shape methodology for surface tension measurement". In: *Applied Surface Science* 238.1-4 SPEC. ISS. (2004), pp. 480–484. DOI: 10.1016/j.apsusc.2004.05.250.

[107] Biolin Scientific. *AttensionTheta*. URL: http://www.biolinscientific.com/product/theta/ (visited on 08/01/2016).

[108] N J Shirtcliffe, G McHale, M I Newton, and C C Perry. "Wetting and wetting transitions on copper-based super-hydrophobic surfaces." In: *Langmuir : the ACS journal of surfaces and colloids* 21.3 (2005), pp. 937–43. DOI: 10.1021/la048630s.

[109] David Quéré. "Rough ideas on wetting". In: *Physica A: Statistical Mechanics and its Applications* 313.1-2 (2002), pp. 32–46. DOI: 10.1016/S0378-4371(02)01033-6.

[110] Yonghao Xiu, Lingbo Zhu, Dennis W Hess, and C P Wong. "Hierarchical silicon etched structures for controlled hydrophobicity/superhydrophobicity." In: *Nano letters* 7.11 (2007), pp. 3388–93. DOI: 10.1021/nl0717457.

[111] Bharat Bhushan and Yong Chae Jung. "Wetting, adhesion and friction of superhydrophobic and hydrophilic leaves and fabricated micro/nanopatterned surfaces". In: *Journal of Physics: Condensed Matter* 20.22 (2008), p. 225010. DOI: 10.1088/0953-8984/20/22/225010.

[112] Kenneth A. Brakke. "The Surface Evolver". In: *Experimental Mathematics* 1.2 (1992), pp. 141–165. DOI: 10.1080/10586458.1992.10504253.

[113] Q-S Zheng, Y Yu, and Z-H Zhao. "Effects of hydraulic pressure on the stability and transition of wetting modes of superhydrophobic surfaces." In: *Langmuir : the ACS journal of surfaces and colloids* 21.26 (2005), pp. 12207–12. DOI: 10.1021/la052054y.

[114] Andrea Cavalli, Peter Bøggild, and Fridolin Okkels. "Topology optimization of robust superhydrophobic surfaces". In: *Soft Matter* 9.7 (2013), p. 2234. DOI: 10.1039/c2sm27214h.

[115] Ming-Hung Chen, Tsung-Hsing Hsu, Yun-Ju Chuang, and Fan-Gang Tseng. "Dual hierarchical biomimic superhydrophobic surface with three energy states". In: *Applied Physics Letters* 95.2 (2009), p. 023702. DOI: 10.1063/1.3180114.

[116] S Dash, N Kumari, and S V Garimella. "Characterization of ultrahydrophobic hierarchical surfaces fabricated using a single-step fabrication methodology". In: *Journal of Micromechanics and Microengineering* 21.10 (2011), p. 105012. DOI: 10.1088/0960-1317/21/10/105012.

[117] Tuukka Verho, Juuso T. Korhonen, Lauri Sainiemi, Ville Jokinen, Chris Bower, Kristian Franze, Sami Franssila, Piers Andrew, Olli Ikkala, and Robin H. A. Ras. "Reversible switching between superhydrophobic states on a hierarchically structured surface". en. In: *Proceedings of the National Academy of Sciences* 109.26 (2012), pp. 10210–10213. DOI: 10.1073/pnas.1204328109.

[118] Bharat Bhushan, Kerstin Koch, and Yong Chae Jung. "Biomimetic hierarchical structure for self-cleaning". In: *Applied Physics Letters* 93.9 (2008), p. 093101. DOI: 10.1063/1.2976635.

[119] Dae Hee Kwon and Sang Joon Lee. "Impact and wetting behaviors of impinging microdroplets on superhydrophobic textured surfaces". In: *Applied Physics Letters* 100.17 (2012), p. 171601. DOI: 10.1063/1.4705296.

[120] Xiying Li, Liqun Mao, and Xuehu Ma. "Dynamic behavior of water droplet impact on microtextured surfaces: the effect of geometrical parameters on anisotropic wetting and the maximum spreading diameter." In: *Langmuir : the ACS journal of surfaces and colloids* 29.4 (2013), pp. 1129–38. DOI: 10.1021/la304567s.

[121] Aurélie Lafuma and David Quéré. "Superhydrophobic states." In: *Nature materials* 2.7 (2003), pp. 457–60. DOI: 10.1038/nmat924.

[122] Mathilde Callies, Yong Chen, Frédéric Marty, Anne Pépin, and David Quéré. "Microfabricated textured surfaces for super-hydrophobicity investigations". In: *Microelectronic Engineering* 78-79.1-4 (2005), pp. 100–105. DOI: 10.1016/j.mee.2004.12.093.

[123] G. B. Foote and P. S. Du Toit. "Terminal Velocity of Raindrops Aloft". In: *Journal of Applied Meteorology* 8.2 (1969), pp. 249–253. DOI: 10.1175/1520-0450(1969)008<0249:TVORA>2.0.CO;2.

[124] Gonzalo Vazquez, Estrella Alvarez, and Jose M Navaza. "Surface Tension of Alcohol Water + Water from 20 to 50 .degree.C". In: *Journal of Chemical & Engineering Data* 40.3 (1995), pp. 611–614. DOI: 10.1021/je00019a016.

[125] Simon Tylsgaard Larsen, Nis Korsgaard Andersen, Emil Søgaard, and Rafael Taboryski. "Structure irregularity impedes drop roll-off at superhydrophobic surfaces." In: *Langmuir : the ACS journal of surfaces and colloids* 30.17 (2014), pp. 5041–5. DOI: 10.1021/la5007633.

[126] TransForm Technologies. *TransForm Website*. URL: http://transform-technologies.dk (visited on 08/14/2016).

[127] Kasper Kistrup, Carl Esben Poulsen, Peter Friis Østergaard, Kenneth Brian Haugshøj, Rafael Taboryski, Anders Wolff, and Mikkel Fougt Hansen. "Fabrication and modelling of injection moulded all-polymer capillary microvalves for passive microfluidic control". In: *Journal of Micromechanics and Microengineering* 24.12 (2014), p. 125007. DOI: 10.1088/0960-1317/24/12/125007.

[128] K. Kistrup, C. E. Poulsen, M. F. Hansen, and A. Wolff. "Ultrasonic welding for fast bonding of self-aligned structures in lab-on-a-chip systems". In: *Lab Chip* 15.9 (2015), pp. 1998–2001. DOI: 10.1039/C5LC00174A.

[129] Kasper Kistrup, Karen Skotte Sørensen, Anders Wolff, and Mikkel Fougt Hansen. "Liquid carry-over in an injection moulded all-polymer chip system for immiscible phase magnetic bead-based solid-phase extraction". In: *Journal of Magnetism and Magnetic Materials* 380 (2015), pp. 191–196. DOI: 10.1016/j.jmmm.2014.10.020.

A

Simulation of filling of holes MATLAB code

The simulation of filling of holes are script wise divided into two parts. First part is a master script that defines all physical variable etc. needed for describing the system. This master script then calls the function diffusionloop in order to calculate the diffusion of gas and moving of triple line. For documentation purposes the scripts are included here.

Master script for time resolved experiment with one specific pressure

```
1
2  clear all
3  pa_vec=[150,225,300,400]*100;
4  bar=1e5;
5  for i=1:4
6
7  elements_in_water=200;              % elements used in the numerical ...
       diffusion problem
8  interface=4;                        % interface used to apply boundary conditions
9  hole_height=3.2e-6;                 % depth of hole
10 water_height=500e-6;                % thickness of water layer above hole
11 R=3.75e-6;                          % Radius of hole
12 aca=102*pi/180;                     % Advancing contact angle of bulk material
13 Kh=6.1e-6;                          % henrys constant for N2 in mol/(m3 Pa);
14 c0=1e5*Kh;                          % initial concentration of N2 in water
15 T=300;                              % temperature during experiment
16
17
18 A_hole=pi*R^2;                      % Cross sectional area of hole
19 A_water=sqrt(3)/2*(2*R+300e-9)^2;   % Cross sectional area of water column
20 V0_hole=A_hole*hole_height;         % Initial volume trapped air hole
21 V0_water=A_water*water_height;      % Initial Volume of water
22
23 % A=pi*R^2;
24 % V0_hole=A*hole_height;
25 % V0_water=A*water_height;
26
27 dt=0.001;                           % time interval used in diffusion simulation
28 c=ones(1,interface*2+elements_in_water)*c0; %concentration profile
29 p_air=bar;                          % Pressure in trapped air
30 iterations=600/dt;                  % number of iterations used in the simulation
31
32 pa=pa_vec(i);                       % Applie pressure
33 constants={R,aca,T,V0_hole,V0_water,pa,water_height}; % constants saved for ...
```

```
    easy forwarding
filling=0;                          % initial filling of hole
[c,filling_vec,p_vec]=diffusionloop_v2(c,iterations,p_air,dt,filling,constants);
output{i,1}=c;                  % saved output for laser use
output{i,2}=filling_vec;
output{i,3}=p_vec;
end



% hold off
% subplot(1,3,1)
% plot(p_vec);
% title('pressure over time')
% subplot(1,3,2)
% plot(filling_vec)
% title('Filling over time')
% subplot(1,3,3)
% plot(c)
% title('concentration as a function of space')


hold on
plot((1:length(filling_vec))*dt/60,filling_vec)
title('Filling over time')
legend(['Pa=',num2str(pa/100),'mbar'])
xlabel('Time [min]','Interpreter','LaTex');
ylabel('Normalized filling of hole','Interpreter','LaTex');
```

And corresponding diffusion loop function

```
function ...
    [c,filling_vec,p_vec]=diffusionloop_v2(c,iterations,p_air,dt,filling,constants)
[R,aca,T,V0_hole,V0_water,pa,water_height]=deal(constants{:});              % ...
    defining constants characteristic of the system
bar = 1e5;                                                                 % ...
    atmospheric pressure
p_water=bar+pa;                                                            % ...
    pressure in water
Kh=6.1e-6;                                                                 % ...
    Henrys konstant for nitrogen
Rg=8.3144621;                                                              % ...
    Gas konstant
filling_vec=zeros(1,iterations);                                           % ...
    defining vector for describing progress of filling
p_vec=zeros(1,iterations);
n0=bar*V0_hole/(Rg*T);
n_hole=n0;
for i=1:iterations
[filling,p_air]=interface_check(filling,p_air,p_water,R,aca,V0_hole);
[c,dc]=diffusion(c,p_air,water_height,dt,Kh);

dn=dc*V0_water;
n1=n_hole;
n2=n_hole-dn;
p_air=n2/n1*p_air;
n_hole=n2;

c_interface=p_air*Kh;
margin=0.001;
```

```
23 if c_interface*(1-margin)<mean(c) && c_interface*(1+margin)>mean(c)
24     display(['System stabilized at ',num2str(filling),'% filling at ...
           time',num2str(i*dt),'s'])
25     filling_vec(i:end)=[];
26     p_vec(i:end)=[];
27     break
28 end
29 if filling>0.99
30     display(['System was completely filled after at',num2str(i*dt),'s'])
31     filling_vec(i:end)=[];
32     p_vec(i:end)=[];
33     break
34 end
35
36 filling_vec(i)=filling;
37 p_vec(i)=p_air;
38 end
39
40
41 if i==iterations
42 display(['Simulation ended after ', num2str(iterations*dt),'s']);
43 end
44
45 function [filling,p_air]=interface_check(filling,p_air,p_water,R,aca,V0_hole)
46 sigma=0.072;
47 dp_surface=-2*sigma*cos(aca)/R;
48 if p_water-p_air>dp_surface;
49     V0=(1-filling)*V0_hole;
50     p0=p_air;
51     p1=p_water-dp_surface;
52     V1=p0*V0/p1;
53
54     filling=(V0_hole-V1)/V0_hole;
55     p_air=p1;
56 end
57
58 function [c,dc]=diffusion(c,p_air,water_height,dt,Kh)
59  %henrys constant for N2 in mol/(m3 Pa);
60 D=1.8e-9;
61 dl=water_height/length(c);
62 boundary=2;
63 c_interface=p_air*Kh;
64 c_new=zeros(1,length(c)+2*boundary);
65 c_new(boundary+1:end-boundary)=c;
66 c_new(1:boundary)=c_interface;
67 c_new(end-boundary+1:end)=c_new(end-boundary);
68 d2c=diff(c_new,2);
69 dct=D*d2c*dt/dl^2;
70 c=c+dct(boundary:end-boundary+1);
71 dc=-dct(1)/length(c);
```

B

Mask Writing Code

I produced a simple matlab script to write the mask file for creating random holes.

```
% Writes a 4x4 grid of 8x8 mm^2 patches with random circles in a cif file
% v3 makes sure all random circles ends up on a specified grid. This is
% done to enshure better compabilty with the laser writing the mask.

%%%%%%%%%%%%%%%%%%%%%%%%%%%%%%%%%%%%%%%%%%%%%%%%%%%%%%%%%%%%%%%%%%%%%%%
%Input parameters

scale=1/2000;               %scale used in cif file [microns]
grid=0.2;                   %grid used for mask writing [um]
Area_sidelength=8000;       %Sidelength of patch [um]
radius_vec=[5,7,9,11]/2;    %Radius of circles [um]
f_vec=[25,30,35,40]/100;    %filling factor
cell_size=9.5*1000;         %Spacing of patches
space_coord=[-1.5,-0.5,0.5,1.5]*cell_size/scale; %position of patches

%%%%%%%%%%%%%%%%%%%%%%%%%%%%%%%%%%%%%%%%%%%%%%%%%%%%%%%%%%%%%%%%%%%%%%%
% Writing file headder

fidin=fopen('M:\Matlab\Random mask\cif_start_v2.txt','r');
fidout=fopen('M:\Matlab\Random mask\test_v3.cif','W');
tline=fgetl(fidin);
while ischar(tline)
   fprintf(fidout,tline);
   fprintf(fidout,'\n');
   tline = fgetl(fidin);
end
fclose(fidin);

%%%%%%%%%%%%%%%%%%%%%%%%%%%%%%%%%%%%%%%%%%%%%%%%%%%%%%%%%%%%%%%%%%%%%%%
% Write cicles

MaxN=round(Area_sidelength^2*max(f_vec)/(pi*min(radius_vec)^2))
Gridcoords=round((rand(2,MaxN)-0.5)*Area_sidelength/grid);
All_coords=round(Gridcoords*grid/scale/2)*2;

for xi=1:4
    for yi=1:4
        % Print header of cell
        fprintf(fidout,'(SCALING: 1 CIF Unit = 1/2000 Microns);\n');
        fprintf(fidout,'DS %d 2 40;\n',xi+4*(yi-1));
        fprintf(fidout,['9 ...
            f',num2str(f_vec(xi)),'-R',num2str(radius_vec(yi)),';\n']);
        fprintf(fidout,'L ACT;\n');

```

```
44          %Calculate coordinates
45          ncircles=round(Area_sidelength^2*f_vec(xi)/(pi*radius_vec(yi)^2))
46          coords=zeros(2,ncircles);
47          coords(1,:)=All_coords(1,1:ncircles)+space_coord(xi);
48          coords(2,:)=All_coords(2,1:ncircles)+space_coord(yi);
49          size(coords);
50          %Print coordinates
51          fprintf(fidout,['R ',num2str(2*round(radius_vec(yi)/scale)) ,' ...
                %d,%d;\n'],coords);
52          fprintf(fidout,'DF;\n');
53      end
54  end
55
56  %end file
57  fprintf(fidout,'E\n');
58  fclose(fidout);
```

In line 19 of the writing script it loads a txt file containing the header for the cif file. This file contains

```
(CIF written by the Tanner Research layout editor, L-Edit);
(Version: 15.22);
(TECHNOLOGY: Generic~0.5~micron~N-Well~Process);
(DATE: 15 Jan 2014);
(FABCELL: Cell0  11 x 11 Microns);
(L-Edit Layer Icon/Outline = CIF Layer CX);
(L-Edit Layer CIF_ACT = CIF Layer ACT);
```

C

Cleanroom Recipes

This Appendix contains an ensable of the processes used in this project. Most values are given as guidelines since each separate process often requires individial optimization that depends on the state of the equipment at the given time.

Step	Temp.	Deposition step						Etch step													
		Time	Pressure	C_4F_8	SF_6	O_2	Coil	Time		Pressure		C_4F_8		SF_6		O_2		Coil		Platen	
								B	M	B	M	B	M	B	M	B	M	B	M	B	M
A	20	**2.8**	5	60	0	0	500	1.5	3.5	30%	5	0	20	100	100	0	0	500	500	50	10

Figure C.1: mboost process parameters. From the Labdaviser webpage.

Recipe	nano1.0	nano1.1	nano1.2	nano1.3	nano1.21	nano1.4	nano1.41	nano1.42	nano1.43
C_4F_8 (sccm)	52	52	52	52	75	75	75	75	75
SF_6 (sccm)	38	38	38	38	38	38	38	38	38
O_2 (sccm)	0	0	0	0	0	0	0	0	0
Coil power (W)	800 (F)	600 (F)	800 (F)	600 (F)	800 (F)	800 (F)	800 (F)	800 (F)	800 (F)
Platen power (W)	50	50	50	40	50	50	75	40	30
Pressure (mtorr)	4	4	4	4	4	4	4	4	4
Temperature (degs C)	10	10	-10	-10	-10	-20	-20	-20	-20
Process time (s)	120	120	120	120	120	120	120	120	120

Figure C.2: Nano etch parameters. From the Labdaviser webpage.

Table C.1: Recipe used for spin coating the wafers. Called 1 μm recipe on the Maximus Spinner.

Step	Time [s]	Accelerations [rpm/s]	maximum speed [rpm]	Temperature [$°C$]
Resist deposition	3	1000	1000	-
Coating	30	1000	4500	-
Spin of	10	1000	1000	-
Baking	60	-	-	90
Cooling	5	-	-	RT

Table C.2: Process parameters for EVG 6″ aligner, for exposing photo resist

Parameter	Value
Mode	Hard Contact
Waiting time before exposure	20 s
Exposure time[a]	2 s

Standard processes

BARC DUV42S-6 coating sequences:

- **(1201) DCH 150mm BARC 65nm** Dispense 3ml@1000rpm; spin-off 30s@4700rpm; softbake 60s@175°C
- **(1202) DCH 100mm BARC 65nm** Dispense 1.6ml@1000rpm; spin-off 30s@3000rpm; softbake 60s@175°C

KRF M230Y coating sequences:

- **(1301) DCH 150mm M230Y 360nm** Dispense 3ml@1000rpm; spin-off 30s@2500rpm; softbake 90s@130°C
- **(1302) DCH 100mm M230Y 360nm** Dispense 1ml@1000rpm; spin-off 30s@2500rpm; softbake 90s@130°C

KRF M35G coating sequences:

- **(1401) DCH 150mm M35G 750nm** Dispense 3ml@1000rpm; spin-off 60s@5000rpm; softbake 90s@130°C
- **(1402) DCH 100mm M35G 750nm** Dispense 1ml@1000rpm; spin-off 60s@5000rpm; softbake 90s@130°C
- **(1403) DCH 150mm M35G 1000nm** Dispense 3ml@1000rpm; spin-off 60s@2630rpm; softbake 90s@130°C
- **(1404) DCH 100mm M35G 1000nm** Dispense 1ml@1000rpm; spin-off 60s@26300rpm; softbake 90s@130°C
- **(1405) DCH 150mm M35G 1400nm** Dispense 3ml@1000rpm; spin-off 60s@1310rpm; softbake 90s@130°C
- **(1406) DCH 100mm M35G 1400nm** Dispense 1ml@1000rpm; spin-off 60s@1310rpm; softbake 90s@130°C

Figure C.3: Spinning recipes for various resist types on the SUSS spinner. From the Labdaviser webpage.

O_2 plasma		**Flow**	200 sccm
		Power	250 Watts
		Time	300 seconds
Repeated 4 times	**Chemical # 1 (vapor order 1)**	**Name**	FDTS2
		Line no.	2
		Cycles	4
		Pressure	0.500 Torr
	Chemical # 2 (vapor order 2)	**Name**	Water
		Line no.	1
		Cycles	1
		Pressure	18 Torr
	Processing	**Time**	900 seconds
	Purge	**Cycles**	5

Figure C.4: Recipe for depositing FDTS by MVD. For Applied Microstructures MVD 100 machine. From the Labdaviser webpage.

Table C.3: Recipe used in this project to produce black silicon structures. The recipe is for the STS D-RIE machine in the DANCHIP cleanroom.

Parameter	Value
SF_6 flow	$70\,\frac{cm^3}{min}$
O_2 flow	$110\,\frac{cm^3}{min}$
RF Coil Power	2700 W
RF Platen Power	30 W
Platen Temperature	$-10\,^\circ$
Process Time	8 min

Table C.4: Parameters used on the plasma asher for removal of resist.

Parameter	Value
O_2 Flow	$400\,\frac{cm^3}{min}$
N_2 Flow	$70\,\frac{cm^3}{min}$
Power	1000 W
Time	15 min -30 min

Table C.5: Showing the ramping of current passed through the sample during nickel deposition. Each step ramps up the current by the displayed amount over the corresponding time and is repeated a number of times. Last step is repeated until the desired total charge has been reached.

Time [s]	Ampere Ramping [A/step]	Repetitions
180	0.1	5
180	0.2	5
3600	0	1
180	1	2
3600	0	x

D

Paper 5

My contribution to this paper is mainly through being a co-inventor of the microstructuring technique used to create the energy director. During the development of this process I characterized the structuring process in collaboration with C. E. Poulsen and K. Kistrup.

E

Paper 6

My contribution to this paper was made during my external stay in Switzerland in the fall 2014. During my stay I participated in the INKA project which is a collaboration between Paul Scherrer Institute (PSI) and Fachhochschule Nordwestschweiz. Since much of the content in this paper is concerned abut injection molding theory, that is somewhat different from the main subject in my thesis, I have chosen to include the paper in the Appendix instead of the main body.

F

Patent 1: Replication Tool and Method of Providing a Replication Tool

G

Patent 2: Micro-scale Energy Director for Ultrasonic Welding

H

Patent 3: Method of Producing an Item with Enhanced Wetting Properties by Fast Replication and Replication Tool Used in the Method

Copyright: Nis Korsgaard Andersen
All rights reserved

Published by:
DTU Nanotech
Department of Micro- and Nanotechnology
Technical University of Denmark
Ørsteds Plads, building 345C
DK-2800 Kgs. Lyngby